



HAL
open science

Simulation of multi-component flows by the lattice Boltzmann method and application to the viscous fingering instability

Lucien Vienne

► **To cite this version:**

Lucien Vienne. Simulation of multi-component flows by the lattice Boltzmann method and application to the viscous fingering instability. Fluid mechanics [physics.class-ph]. Conservatoire national des arts et metiers - CNAM, 2019. English. NNT : 2019CNAM1257 . tel-02447641

HAL Id: tel-02447641

<https://theses.hal.science/tel-02447641v1>

Submitted on 21 Jan 2020

HAL is a multi-disciplinary open access archive for the deposit and dissemination of scientific research documents, whether they are published or not. The documents may come from teaching and research institutions in France or abroad, or from public or private research centers.

L'archive ouverte pluridisciplinaire **HAL**, est destinée au dépôt et à la diffusion de documents scientifiques de niveau recherche, publiés ou non, émanant des établissements d'enseignement et de recherche français ou étrangers, des laboratoires publics ou privés.

École doctorale Sciences des Métiers de l'Ingénieur
Laboratoire de Dynamique des Fluides

THÈSE DE DOCTORAT

présentée par : **Lucien VIENNE**

soutenue le : **03 Décembre 2019**

pour obtenir le grade de : **Docteur du Conservatoire National des Arts et Métiers**

Discipline : Mécanique, génie mécanique, génie civil

Spécialité : Mécanique

Simulation of multi-component flows by the lattice Boltzmann method and application to the viscous fingering instability

THÈSE dirigée par

M. GRASSO Francesco

Professeur, Titulaire de Chaire, CNAM

et co-encadré par

M. MARIÉ Simon

Maître de conférences, CNAM

RAPPORTEURS

M. ASINARI Pietro

Professeur, Politecnico di Torino

Mme PODVIN Bérengère

Chargé de recherche, LIMSI

PRÉSIDENT DU JURY

M. SAGAUT Pierre

Professeur des Universités, Université Aix-Marseille

EXAMINATEURS

M. DUBOIS François

Professeur des Universités, CNAM

Remerciements

Tout d'abord, je souhaite remercier les membres de mon jury qui ont accepté d'évaluer mon travail. En particulier, Bérengère PODVIN et Pietro ASINARI qui ont témoigné de l'intérêt pour mon travail de thèse en acceptant de la rapporter, d'avoir lu attentivement mon manuscrit en proposant des améliorations et en formulant des critiques constructives. Merci à François DUBOIS et Pierre SAGAUT de m'avoir fait l'honneur de participer à mon jury de soutenance.

Bien évidemment, ce travail n'aurait pas pu exister et aboutir sans Francesco GRASSO qui a dirigé cette thèse et Simon MARIÉ qui l'a co-encadrée. Je te suis particulièrement reconnaissant, Simon, pour nos échanges et discussions tout au long de ces trois années de travail durant lesquelles j'ai pris plaisir à travailler avec toi.

Je remercie également l'ensemble des membres du laboratoire DynFluid pour l'ambiance chaleureuse et amicale. Les débats passionnés pendant la pause déjeuner vont me manquer.

Un dernier mot pour remercier mes parents qui m'ont permis d'arriver jusque là et mon frère ainsi que mes amis notamment Clovis, Sandrine et Thaïs.

Abstract

The lattice Boltzmann method (LBM) is a specific discrete formulation of the Boltzmann equation. Since its first premises, thirty years ago, this method has gained some popularity and is now applied to almost all standard problems encountered in fluid mechanics including multi-component flows. In this work, we introduce the inter-molecular friction forces to take into account the interaction between molecules of different kinds resulting primarily in diffusion between components. Viscous dissipation (standard collision) and molecular diffusion (inter-molecular friction forces) phenomena are split, and both can be tuned distinctively. The main advantage of this strategy is optimizations of the collision and advanced collision operators are readily compatible. Adapting an existing code from single component to multiple miscible components is straightforward and required much less effort than the large modifications needed from previously available lattice Boltzmann models. Besides, there is no mixture approximation : each species has its own transport coefficients, which can be calculated from the kinetic theory of gases. In general, diffusion and convection are dealt with two separate mechanisms : one acting respectively on the species mass and the other acting on the mixture momentum. By employing an inter-molecular friction force, the diffusion and convection are coupled through the species momentum. Diffusion and convection mechanisms are closely related in several physical phenomena such as in the viscous fingering instability.

A simulation of the viscous fingering instability is achieved by considering two species in different proportions in a porous medium : a less viscous mixture displacing a more viscous mixture. The core ingredients of the instability are the diffusion and the viscosity contrast between the components. Two strategies are investigated to mimic the effects of the porous medium. The gray lattice Boltzmann and Brinkman force models, although based on fundamentally different approaches, give in our case equivalent results. For early times, comparisons with linear stability analyses agree well with the growth rate calculated from the simulations. For intermediate times, the evolution of the mixing length can be divided into two stages dominated first by diffusion then by convection, as found in the literature. The whole physics of the viscous fingering is thus accurately simulated. Nevertheless, multi-component diffusion effects are usually not taken into account in the case of viscous fingering with three and more species. These effects are non-negligible as we showcase an initial stable configuration that becomes unstable. The reverse diffusion induces fingering whose impact depends on the diffusion between species.

Keywords : lattice Boltzmann method, fluid mechanics, multi-component flows, mixture dynamics, viscous fingering instability

Résumé

La méthode de Boltzmann sur réseau est une formulation discrète particulière de l'équation de Boltzmann. Depuis ses débuts, il y a trente ans, cette méthode a gagné une certaine popularité, et elle est maintenant utilisée dans presque tous les problèmes habituellement rencontrés en mécanique des fluides notamment pour les écoulements multi-espèces. Dans le cadre de ce travail, une force de friction intermoléculaire est introduite pour modéliser les interactions entre les molécules de différent types causant principalement la diffusion entre les espèces. Les phénomènes de dissipation visqueuse (collision usuelle) et de diffusion moléculaire (force de friction intermoléculaire) sont séparés et peuvent être ajustés indépendamment. Le principal avantage de cette stratégie est sa compatibilité avec des optimisations de la collision et les opérateurs de collision avancés. Adapter un code mono-espèce pour aboutir à un code multi-espèces est aisé et demande beaucoup moins d'effort comparé aux précédentes tentatives. De plus, il n'y a pas d'approximation du mélange, chaque espèce a ses propres coefficients de transport pouvant être calculés à l'aide de la théorie cinétique des gaz. En général, la diffusion et la convection sont vus comme deux mécanismes séparés : l'un agissant sur la masse d'une espèce, l'autre sur la quantité de mouvement du mélange. En utilisant une force de friction intermoléculaire, la diffusion et la convection sont couplés par l'intermédiaire la quantité de mouvement de chaque espèce. Les mécanismes de diffusion et de convection sont intimement liés dans de nombreux phénomènes physique tel que la digitation visqueuse.

L'instabilité de digitation visqueuse est simulée en considérant dans un milieu poreux deux espèces dans des proportions différentes soit un mélange moins visqueux déplaçant un mélange plus visqueux. Les principaux moteurs de l'instabilité sont la diffusion et le contraste de viscosité entre les espèces. Deux stratégies sont envisagées pour simuler les effets d'un milieu poreux. Les méthodes de rebond partiel et de force de Brinkman bien que basées sur des approches fondamentalement différentes donnent dans notre cas des résultats identiques. Les taux de croissance de l'instabilité calculés à partir de la simulation coïncident avec ceux obtenus à partir d'analyses de stabilité linéaire. L'évolution de la longueur de mélange peut être divisée en deux étapes dominées d'abord par la diffusion puis par la convection. La physique de la digitation visqueuse est ainsi correctement simulée. Toutefois, les effets de diffusion multi-espèces ne sont généralement pas pris en compte lors de la digitation visqueuse de trois espèces et plus. Ces derniers ne sont pas négligeable puisque nous mettons en avant une configuration initialement stable qui se déstabilise. La diffusion inverse entraîne la digitation dont l'impact dépend de la diffusion entre les espèces.

Un résumé étendu des travaux de la thèse est disponible en annexe F.

Mots clés : méthode de Boltzmann sur réseau, mécanique des fluides, écoulements multi-espèces, dynamique du mélange, instabilité de digitation visqueuse

Contents

Introduction	3
I Background	7
1 Kinetic theory of gases	11
1.1 Distribution function	12
1.2 Boltzmann equation	12
1.3 Collision operator	13
1.4 Macroscopic balance equations	16
2 Lattice Boltzmann method	19
2.1 Non-dimensional formulation	20
2.2 Discretization of the velocity space	21
2.3 Discrete velocity sets	24
2.4 Discretization of physical space and time	26
2.5 Chapman and Enskog expansion procedure	29
2.6 Advanced collision operators	34
2.7 Boundary conditions	39
2.8 Synthesis	43
3 Mixture of gases	45
3.1 Multi-component diffusion theory	45
3.2 Limitations of Fick's law	47
II LBM for miscible gases: a forcing term approach	53
4 Lattice Boltzmann models for mixtures	57
5 A simplified kinetic model for multi-component mixtures	61
5.1 Lattice Boltzmann algorithm	61
5.2 Species with different molecular masses	63

CONTENTS

6	Macroscopic limit	65
6.1	Macroscopic equations	65
6.2	Some variations on the equation formulation	65
6.3	Limit expressions	67
6.4	Transport coefficients	71
7	Numerical simulations	73
7.1	A- Decay of a density wave	73
7.2	B- Equimolar counter-diffusion	76
7.3	C- Loschmidt's tube	77
7.4	D- Opposed jets flow	80
8	Synthesis	83
III	Simulation of the viscous fingering by the LBM	85
9	Viscous fingering instability	89
10	Porous medium in LBM	93
10.1	Gray lattice Boltzmann	93
10.2	Brinkman drag force	94
11	Numerical simulations	95
11.1	Darcy's law	95
11.2	Viscous fingering	95
11.3	Viscous fingering caused by reverse diffusion	106
12	Synthesis	111
	Conclusion	115
	Appendix	119
A	Hermite polynomials and Gauss-Hermite quadrature	121
A.1	Hermite polynomials 1-dimensional space	121
A.2	Hermite polynomials in d-dimensional space	122
A.3	Gauss-Hermite quadrature	123
B	Programming considerations	127
B.1	Code	127
B.2	HPC	128

C Kinetic theory for the calculation of transport coefficients	129
C.1 Omega-integrals	129
C.2 Wilke's law	130
C.3 A more common formulation of the diffusion coefficient	132
D Viscous fingering	135
D.1 Most dangerous and cutoff wave numbers	135
D.2 Color maps of the molar fraction for different Péclet numbers	135
E Parallel activities	137
E.1 Conferences and discussions	137
E.2 Ercoftac Montestigliano spring-school	137
F Résumé étendu des travaux de la thèse en français	143
Bibliography	153

Introduction

Fluid mechanics is a branch of Physics dedicated to the study of gases and liquids flows. Consider the air we breathe, to the human senses, air is continuum and uniform, and we usually describe it by using terms such as density or velocity. However, if we observe air at a sufficient scale ($\approx 10^{-9}\text{m}$), we will see billions of molecules moving around and colliding with each other. Tracking all these movements individually is overwhelming and impractical in reality for a tangible amount of gas. Instead, the evolution of the distribution of gas molecules is a more convenient quantity to follow. This route is called the kinetic theory of gases, and the famous Boltzmann equation governs the distribution of molecules. The collision effects are not trivial and are usually approximated by defining an equilibrium state that the gas tends to reach. The time required for the distribution of molecules to relax toward the equilibrium is mainly due to the viscous dissipation caused by the collision of molecules. If we return to our elemental material, air, we notice that air is predominantly composed of two components: nitrogen (N_2 , $\approx 78\%$) and oxygen (O_2 , $\approx 21\%$). In fact in nature, species commonly mix each other and, generally, pure compounds are a human creation. A natural approach in the case of mixing components is then to consider the evolution of the distribution of each type of molecules. The most complex part remains to appropriately take into account the effect of collisions of different types of molecules.

An analytical solution of fluid flows is unfortunately only known for simple configurations. We will seek for an approximated solution by limiting to only a small amount of all possible molecules directions. In this way, space, time, and molecules velocities are divided into discrete elements representing the continuum reality. This finite representation of the problem can be solved using numerical techniques on computers. The lattice Boltzmann method (LBM) is a specific discrete formulation of the Boltzmann equation. Since its first premises, thirty years ago, this method has gained some popularity and is now applied to almost all standard problems encountered in fluid mechanics such as multi-phase flows, thermal flows, turbulent flows, acoustics, flows in porous media, and multi-component flows, to name a few. Its apparent simplicity and ease of implementation compared to traditional methods to solve fluid flows may explain its increasing use. It should be noted, however, that these two last arguments are only partially true: applying even incredible simple procedures to a complex scenario will result in a complicated end.

As we mentioned before, the way the distribution of molecules change after collisions is critical. In LBM, there is no unique or generally accepted collision operator in the case of mixing components. Different lattice Boltzmann models for miscible species have been proposed depending on the underlying kinetic theory chosen. Some separate the collision between similar and dissimilar molecules, others employ a global equilibrium state. The collision step already crucial is then modified and becomes more complex. In this work, we will circumvent this difficulty by introducing the inter-molecular friction forces to take into account the interaction between molecules of different kinds resulting primarily in diffusion between components. The usual collision namely the relaxation of the distribution toward a species equilibrium state is used. Viscous dissipation (standard collision) and molecular diffusion (inter-molecular friction forces) phenomena are

split, and both can be tuned distinctively. The main advantage of this strategy is that optimizations of the collision and advanced collision operators are readily compatible. Adapting an existing code from single component to multiple miscible components is straightforward and required much less effort than the large modifications needed from previously available lattice Boltzmann models. The collision is the cornerstone of the lattice Boltzmann method, and a revamp of the collision generally results in entirely rewriting the code. Besides, there is no mixture approximation: each species has its own transport coefficients, which can be calculated from the kinetic theory of gases. In general, diffusion and convection are dealt with two separate mechanisms: one acting respectively on the species mass and the other acting on the mixture momentum. By employing an inter-molecular friction force, the diffusion and convection are coupled through the species momentum. Diffusion and convection mechanisms are closely related in several physical phenomena such as in the viscous fingering instability.

Viscous fingering is an ubiquitous instability that occurs when a less viscous fluid displaces a more viscous fluid in a porous medium. The interface between the two fluids starts to deform, and finger-like patterns emerge and grow. This phenomenon can either increase the mixing in porous media, which is incredibly difficult because of the absence of turbulence that can actively stir the flow or be dramatic to some processes. The typical example is secondary oil recovery, for which fingering from the injected aqueous solution pushing the more viscous oil in underground reservoirs of porous rocks reduces the sweep efficiency severely. Similarly, one solution to decrease the carbon dioxide emitted to the atmosphere is to capture it directly from the power plants and gas production sites, and stores in available reservoirs. The interaction between the supercritical CO_2 and the interstitial fluids, usually brine, is of interest. The resulting mixture from the carbon dioxide dissolution could undergo fingering and change radically the distribution of CO_2 in the reservoir. Viscous fingering is also detrimental in the case of chromatography, a technique used to separate and identify chemical compounds in a mixture flowing through a porous medium. The displacing fluid (the eluent) may be less viscous than the sample mixture. The initial planar interface will deform because of fingering, resulting in an inefficient separation. Last, viscous fingering can play a major role in soil contamination by enlarging considerably the polluted area. Hence the study of viscous fingering is essential in numbers of domains.

Thesis structure

The thesis structure is divided into three main parts. Part I contains the necessary background materials to deal with the lattice Boltzmann method and miscible mixtures. The first two chapters detail the basics of the lattice Boltzmann for single (and simple) fluid. The third chapter presents independently the Maxwell-Stefan approach to mass transfer from simple considerations. This is deliberate since a direct derivation from the kinetic theory of gases would be lengthy, complicated, and paraphrases the seminal book molecular theory of gases and liquids by Hirschfelder, Curtiss, and Bird [1]. Part II is the main contribution of the thesis. We combine the approach of the third chapter within the lattice Boltzmann framework. The proposed model is then validated against analytical, experimental, and numerical results. Finally, part III presents an application. The viscous fingering instability is simulated for two and three miscible components.

Part I
Background

1	Kinetic theory of gases	11
1.1	Distribution function	12
1.2	Boltzmann equation	12
1.3	Collision operator	13
1.4	Macroscopic balance equations	16
2	Lattice Boltzmann method	19
2.1	Non-dimensional formulation	20
2.2	Discretization of the velocity space	21
2.3	Discrete velocity sets	24
2.4	Discretization of physical space and time	26
2.5	Chapman and Enskog expansion procedure	29
2.6	Advanced collision operators	34
2.7	Boundary conditions	39
2.8	Synthesis	43
3	Mixture of gases	45
3.1	Multi-component diffusion theory	45
3.2	Limitations of Fick's law	47

Chapter 1

Kinetic theory of gases

A gas at rest is composed of billions of molecules flying around and colliding with each other. Classical and quantum mechanics have been successfully used to describe simple systems with a few degrees of freedom. However, these principles are impractical to examine the behavior of a tangible amount of gas. A single gram of the air we breathe consists of over 10^{22} molecules. Also, the knowledge of the microscopic state is not particularly of interest when studying a gas flow.

Instead of tracking the motions of individual molecules at the microscopic scale, a statistical description of the gas is more appropriate. The gas is then described according to the density of molecules. This corresponds to the mesoscopic scale. The non-equilibrium behavior of dilute gases was investigated about two centuries ago by Maxwell, Boltzmann, and others. This specific branch of statistical mechanics is called the kinetic theory of gas.

A few assumptions have to be made concerning the gas. All of the molecules of the gas are spherical, non-polar and identical. They spend a very little of their time colliding meaning that the fraction of collisions involving more than two molecules is negligible. This excludes dense gases and liquids although some developments exist [1]. Furthermore, we restrict the discussion to the kinetic theory of monatomic dilute gases. Single atoms collide elastically and the translational energy is conserved during a collision. For polyatomic gases, two internal degrees of freedom also exist: the molecules can rotate and vibrate, and these phenomena should be treated with quantum mechanics. Nonetheless, diffusion coefficient and shear viscosity are not very much affected by the internal degrees of freedom. Therefore, the results are in practice more generally applicable than these assumptions assert. It should be noted that the volume viscosity and the coefficient of thermal conductivity are quite dependent on the internal degrees of freedom but the influences of these transport coefficients are irrelevant for the isothermal and low Mach number flows investigated in this thesis.

In the following sections, we provide an introduction to kinetic theory, which is the cornerstone of the lattice Boltzmann method.

1.1 Distribution function

The fundamental quantity in kinetic theory is the distribution function $f(\mathbf{x}, \mathbf{c}, t)$. The variable f describes the probability to find a particle (molecule) with velocity \mathbf{c} at position \mathbf{x} and time t . The macroscopic quantities such as fluid density, fluid velocity, and fluid internal energy can be found by means of the moments of the distribution function. These moments link the mesoscopic and macroscopic scales. This excludes the case of rarefied gases where the gas does not longer behave as a continuum, hence macroscopic quantities are inadequate.

If we integrate over the entire (microscopic) velocity space, we obtain the fluid density at a particular point and time,

$$\rho(\mathbf{x}, t) = \int f(\mathbf{x}, \mathbf{c}, t) d\mathbf{c}. \quad (1.1)$$

The second moment corresponds to the integration weighted with \mathbf{c} over the entire velocity space and gives the fluid momentum density,

$$\rho(\mathbf{x}, t) \mathbf{u}(\mathbf{x}, t) = \int \mathbf{c} f(\mathbf{x}, \mathbf{c}, t) d\mathbf{c}. \quad (1.2)$$

Similarly, the fluid energy density is related to the third moment,

$$\rho(\mathbf{x}, t) E(\mathbf{x}, t) = \int \frac{1}{2} \mathbf{c}^2 f(\mathbf{x}, \mathbf{c}, t) d\mathbf{c}. \quad (1.3)$$

The fluid energy density can be split into two parts: the kinetic energy density due to the fluid motion and the internal energy density, $\rho E = \rho e + \rho \frac{1}{2} \mathbf{u}^2$ or we can write $\rho(\mathbf{x}, t) e(\mathbf{x}, t) = \int 1/2 (\mathbf{c} - \mathbf{u})^2 f(\mathbf{x}, \mathbf{c}, t) d\mathbf{c}$. Here, only the translational energy is considered.

1.2 Boltzmann equation

The distribution function depends on \mathbf{x} , \mathbf{c} , and t . The evolution of the distribution function according to the time is given by the total derivative,

$$\frac{df}{dt} = \left(\frac{\partial f}{\partial x_i} \right) \frac{dx_i}{dt} + \left(\frac{\partial f}{\partial c_i} \right) \frac{dc_i}{dt} + \left(\frac{\partial f}{\partial t} \right) \frac{dt}{dt}, \quad (1.4)$$

where dx_i/dt is equivalent to the particle velocity c_i , dc_i/dt is the particle's acceleration, which according to the Newton's second law is equal to the body force acting on the particles $dc_i/dt = F_{Bi}/\rho$. The previous equation can be rewritten as

$$\frac{\partial f}{\partial t} + c_i \left(\frac{\partial f}{\partial x_i} \right) + \frac{F_{Bi}}{\rho} \left(\frac{\partial f}{\partial c_i} \right) = \frac{df}{dt}. \quad (1.5)$$

This equation is very similar to an advection equation where the distribution function is advected with a velocity of c_i . The third term represents the influence of the body force.

The right-hand side is similar to a source term and depicts the rate of change of the distribution function df/dt due to collisions. The resulting equation is the Boltzmann equation and the right-hand side is called the collision operator. Using vector formulation yields to

$$\frac{\partial f}{\partial t} + \mathbf{c} \cdot \nabla f + \frac{\mathbf{F}_B}{\rho} \cdot \nabla_{\mathbf{c}} f = \left(\frac{df}{dt} \right)_{coll}, \quad (1.6)$$

where ∇ is the gradient in the physical space and $\nabla_{\mathbf{c}}$ is the gradient in the velocity space.

1.3 Collision operator

The collision conserves the mass, the momentum, and the energy of particles, which is equivalent to

$$\int \left(\frac{df}{dt} \right)_{coll} d\mathbf{c} = 0, \quad (1.7)$$

$$\int \mathbf{c} \left(\frac{df}{dt} \right)_{coll} d\mathbf{c} = \mathbf{0}, \quad (1.8)$$

$$\int \frac{1}{2} \mathbf{c}^2 \left(\frac{df}{dt} \right)_{coll} d\mathbf{c} = 0; \quad (1.9)$$

1, \mathbf{c} , $\frac{1}{2} \mathbf{c}^2$ are the collision invariants and results from the conservation laws of the system.

Using geometric considerations and assuming no correlations between particles prior to the collision (also known as molecular chaos approximation), the rate of change due to the binary collision of particles takes the following form

$$\left(\frac{df}{dt} \right)_{coll} = \int (f_{1'} f_{2'} - f_1 f_2) \mathbf{g} b db d\epsilon d\mathbf{c}_2, \quad (1.10)$$

where f_1 and $f_{1'}$ refer to the distribution function of the first particle before and after the collision. \mathbf{g} is the initial relative speed of the two particles, b and ϵ are some geometrical quantities. More detailed explanations can be found in Ref. [1, 2] but for the sake of simplicity are not given here and are not necessary for the next developments.

1.3.1 Equilibrium

Let us consider the case of uniform conditions and absence of external forces, Eq. (1.6) becomes

$$\frac{\partial f}{\partial t} = \int (f_{1'} f_{2'} - f_1 f_2) \mathbf{g} b db d\epsilon d\mathbf{c}_2 \quad (1.11)$$

A gas is at a local equilibrium state when the distribution function does not vary in time. This does not mean that particles sit idle and no collision occur but rather that the collisions do not change the distribution of gas particles. This leads to

$$f_{1'}^{eq} f_{2'}^{eq} = f_1^{eq} f_2^{eq}. \quad (1.12)$$

Taking the logarithm yields

$$\ln(f_{1'}^{eq}) + \ln(f_{2'}^{eq}) = \ln(f_1^{eq}) + \ln(f_2^{eq}). \quad (1.13)$$

The logarithm of the distribution functions is a summational invariant of the collision. Thus it can be shown that the summational invariant must be a linear combination of the three collision invariants, so that

$$\ln(f^{eq}) = A + \mathbf{B} \cdot \mathbf{c} - C \frac{1}{2} \mathbf{c}^2, \quad (1.14)$$

where A , C are scalars, and \mathbf{B} is a vector. They are independent of \mathbf{x} , t since the state of the gas is steady and uniform. This can be rewritten as

$$\ln(f^{eq}) = \ln D + \frac{1}{2} C (\mathbf{c} - \frac{1}{C} \mathbf{B})^2 \quad (1.15)$$

$$f^{eq} = D e^{\frac{1}{2} C (\mathbf{c} - \frac{1}{C} \mathbf{B})^2} \quad (1.16)$$

$$f^{eq} = D e^{-\frac{1}{2} C \mathbf{c}'^2} \quad (1.17)$$

where D is a new constant and $\mathbf{c}' = \mathbf{c} - \frac{1}{C} \mathbf{B}$. The unknown constant can be computed by using the moments of the equilibrium distribution function. For the first moment, we have

$$\rho = \int f^{eq} d\mathbf{c} = D \int e^{-\frac{1}{2} C \mathbf{c}'^2} d\mathbf{c}'. \quad (1.18)$$

With the help of Gaussian integrals ($\int_{-\infty}^{\infty} e^{-a(x+b)^2} dx = \sqrt{\pi/a}$), we obtain

$$\rho = D \int_{-\infty}^{\infty} e^{-\frac{1}{2} C \mathbf{c}'^2} d\mathbf{c}' = D \int_{-\infty}^{\infty} \int_{-\infty}^{\infty} \int_{-\infty}^{\infty} e^{-\frac{1}{2} C (c_x'^2 + c_y'^2 + c_z'^2)} dc_x' dc_y' dc_z' \quad (1.19)$$

$$\rho = D \left(\frac{2\pi}{C} \right)^{3/2} \quad (1.20)$$

The second equilibrium moment is equivalent to

$$\rho \mathbf{u} = \int \mathbf{c} f^{eq} d\mathbf{c} \quad (1.21)$$

$$\rho \mathbf{u} = \int_{-\infty}^{\infty} (\mathbf{B}/C + \mathbf{c}') f^{eq} d\mathbf{c}' \quad (1.22)$$

$$\rho \mathbf{u} = \rho \mathbf{B}/C + D \int_{-\infty}^{\infty} \mathbf{c}' e^{-\frac{1}{2} C \mathbf{c}'^2} d\mathbf{c}' \quad (1.23)$$

$$\mathbf{u} = \mathbf{B}/C. \quad (1.24)$$

The second integral term vanishes because the integrand is an odd function. This results to $\mathbf{c}' = \mathbf{c} - \mathbf{u}$. Using the definition of the internal energy of a monatomic gas at steady

state gives,

$$\rho e = \frac{3}{2} \frac{k_B T}{m} = \int \frac{1}{2} (\mathbf{c} - \mathbf{u})^2 f^{eq} d\mathbf{c} \quad (1.25)$$

$$\frac{3}{2} \frac{k_B T}{m} = \frac{1}{2} D \int_{-\infty}^{\infty} \mathbf{c}'^2 e^{-\frac{1}{2} C \mathbf{c}'^2} d\mathbf{c}' \quad (1.26)$$

$$\frac{3}{2} \frac{k_B T}{m} = \frac{1}{2} D \int_{-\infty}^{\infty} \int_{-\infty}^{\infty} \int_{-\infty}^{\infty} (c_x'^2 + c_y'^2 + c_z'^2) e^{-\frac{1}{2} C (c_x'^2 + c_y'^2 + c_z'^2)} d c_x' d c_y' d c_z' \quad (1.27)$$

$$\frac{3}{2} \frac{k_B T}{m} = \frac{1}{2} D \frac{3}{C} \left(\frac{2\pi}{C} \right)^{3/2} \quad (1.28)$$

$$\frac{k_B T}{m} = \frac{1}{C} \quad (1.29)$$

with k_B the Boltzmann constant, T the temperature, and m the mass of one particle of gas. The following Gaussian integral $\int_{-\infty}^{\infty} x^2 e^{-ax^2} dx = \sqrt{\pi/a}/(2a)$ has been used to compute the integral. Finally, we recover the famous Maxwell-Boltzmann equilibrium distribution for a d ($d = 3$ in the previous derivation) dimensional space:

$$f^{eq} = \rho \left(\frac{m}{2\pi k_B T} \right)^{d/2} e^{-\frac{m}{2k_B T} (\mathbf{c} - \mathbf{u})^2} \quad (1.30)$$

$$= \frac{\rho}{(2\pi R_s T)^{d/2}} e^{-(\mathbf{c} - \mathbf{u})^2 / (2R_s T)} \quad (1.31)$$

where $R_s = k_B/m$ is the specific gas constant.

1.3.2 BGK collision operator

The complicated nonlinear integral collision operator Eq. (1.10) is often replaced by a simpler expression avoiding the inherent mathematical difficulties but resulting in correct macroscopic behavior. Bhatnagar, Gross, and Krook propose the so-called BGK collision operator [3],

$$\left(\frac{df}{dt} \right)_{coll} = -\frac{1}{\tau} (f - f^{eq}) \quad (1.32)$$

where they introduced the relaxation time τ . This operator obeys to Eqs. (1.7),(1.8), (1.9) assuring the conservation of the mass, momentum and energy during the collision. One drastic simplification associated is the use of a relaxation time independent of the distribution function f .

As an example, if we consider a gas whose distribution function is uniform in space $f(\mathbf{x}, \mathbf{c}, t) = f(\mathbf{c}, t)$ but the gas is not at the equilibrium state at $t = 0$,

$$\frac{\partial f(\mathbf{c}, t)}{\partial t} = -\frac{1}{\tau} [f(\mathbf{c}, t) - f^{eq}(\mathbf{c})] \quad (1.33)$$

$$f(\mathbf{c}, t) = f^{eq}(\mathbf{c}) + (f(\mathbf{c}, 0) - f^{eq}(\mathbf{c})) e^{-t/\tau} \quad (1.34)$$

The distribution function relaxes exponentially to the equilibrium according to the typical time-scale parameter τ .

1.4 Macroscopic balance equations

The macroscopic conservation equations for the three invariants (mass, momentum, and energy) can be derived from the Boltzmann equation Eq. (1.6).

First, we introduce the following notation for the moments of f :

$$\begin{aligned}\Pi_0 &= \int f d\mathbf{c} = \rho, & \Pi_i &= \int c_i f d\mathbf{c} = \rho u_i, \\ \Pi_{ij} &= \int c_i c_j f d\mathbf{c}, & \Pi_{ijk} &= \int c_i c_j c_k f d\mathbf{c},\end{aligned}\tag{1.35}$$

and so forth. These moments are unchanged if their indices are reordered, e.g, $\Pi_{xyz} = \Pi_{yxz}$. Concerning the force term, this next expression will be useful,

$$\int \psi \frac{\partial f}{\partial c_i} d\mathbf{c} = \int \int \psi f dc_j dc_k - \int f \frac{\partial \psi}{\partial c_i} d\mathbf{c}.\tag{1.36}$$

The first term of this integration by parts, i.e., the surface integral, vanishes because the product ψf is assumed to diminish rapidly for large \mathbf{c} [1, 4]. Integrating Eq. (1.6) multiplied by an arbitrary quantity ψ over \mathbf{c} results in the Enskog's general equation of change. In particular, the fundamental hydrodynamic equations of mass, motion, and energy balance are recovered for $\psi = 1, c_i, c_i c_i$.

Before the following preliminary result will be needed: equation (1.36) yields

$$\int \frac{\partial f}{\partial c_i} d\mathbf{c} = 0,\tag{1.37}$$

$$\int c_i \frac{\partial f}{\partial c_j} d\mathbf{c} = - \int \frac{\partial c_i}{\partial c_j} f d\mathbf{c} = -\rho \delta_{ij},\tag{1.38}$$

$$\int c_i c_i \frac{\partial f}{\partial c_j} f d\mathbf{c} = - \int \frac{\partial(c_i c_i)}{\partial c_j} d\mathbf{c} = -2\rho u_j.\tag{1.39}$$

Now, we now apply the moment "operator", i.e., $\int \bullet d\mathbf{c}$, $\int c_i \bullet d\mathbf{c}$, and $1/2 \int c_i c_i \bullet d\mathbf{c}$ (equivalent to $\psi = 1, c_i, 1/2 c_i c_i$) to the Boltzmann equation Eq. (1.6). If we integrate the Boltzmann equation over the velocity space, we get,

$$\frac{\partial}{\partial t} \int f d\mathbf{c} + \frac{\partial}{\partial x_i} \int c_i f d\mathbf{c} + \frac{F_{Bi}}{\rho} \int \frac{\partial f}{\partial c_i} d\mathbf{c} = \int \left(\frac{df}{dt} \right)_{coll} d\mathbf{c}.\tag{1.40}$$

Note that the space and time derivatives have been moved out the integrals since t and \mathbf{x} are not function of \mathbf{c} . In addition, since velocity and space coordinates are independent variables, $c_i \partial f / \partial x_i = \partial(c_i f) / \partial x_i$. Using Eqs. (1.1), (1.2), (1.7), and (1.37) gives the continuity equation,

$$\frac{\partial \rho}{\partial t} + \frac{\partial(\rho u_i)}{\partial x_i} = 0.\tag{1.41}$$

If we multiply the Boltzmann equation Eq. (1.6) by c_i and integrate over the velocity space, we find,

$$\frac{\partial}{\partial t} \int c_i f d\mathbf{c} + \frac{\partial}{\partial x_j} \int c_i c_j f d\mathbf{c} + \frac{F_{Bj}}{\rho} \int c_i \frac{\partial f}{\partial c_j} d\mathbf{c} = \int c_i \left(\frac{df}{dt} \right)_{coll} d\mathbf{c}.\tag{1.42}$$

Using Eqs (1.2), (1.8), (1.35), and (1.38) results in

$$\frac{\partial \rho u_i}{\partial t} + \frac{\partial \Pi_{ij}}{\partial x_j} = F_{\mathcal{B}i} \quad (1.43)$$

The second moment Π_{ij} can be rewritten as

$$\Pi_{ij} = \int (c_i - u_i)(c_j - u_j) f d\mathbf{c} + \rho u_i u_j \quad (1.44)$$

Hence, the momentum equation in a conservation form is obtained,

$$\frac{\partial(\rho u_i)}{\partial t} + \frac{\partial(\rho u_i u_j)}{\partial x_j} = \frac{\partial \sigma_{ij}}{\partial x_j} + F_{\mathcal{B}i}, \quad (1.45)$$

where $\sigma_{ij} = -\int (c_i - u_i)(c_j - u_j) f d\mathbf{c}$ is the Cauchy stress tensor, which is naturally symmetric by definition.

Finally, if we multiply the Boltzmann equation by $1/2 c_j c_j$ and integrate over the velocity space, Eq. (1.6) becomes,

$$\frac{1}{2} \frac{\partial}{\partial t} \int c_j c_j f d\mathbf{c} + \frac{1}{2} \frac{\partial}{\partial x_i} \int c_i c_j c_j f d\mathbf{c} + \frac{1}{2} \frac{F_{\mathcal{B}i}}{\rho} \int c_j c_j \frac{\partial f}{\partial c_i} d\mathbf{c} = \frac{1}{2} \int c_j c_j \left(\frac{df}{dt} \right)_{coll} d\mathbf{c}. \quad (1.46)$$

Using Eqs. (1.3, (1.9), (1.35), and (1.39), this reduces to

$$\frac{\partial(\rho E)}{\partial t} + \frac{1}{2} \frac{\partial \Pi_{ijj}}{\partial x_i} = u_i F_{\mathcal{B}i}, \quad (1.47)$$

The third moment Π_{ijj} can be written in an equivalent form using

$$q_i = \frac{1}{2} \int (c_i - u_i)(c_j - u_j)^2 f d\mathbf{c} \quad (1.48)$$

$$= \frac{1}{2} \left[\Pi_{ijj} - 2u_j \Pi_{ij} - u_i \rho E + 2\rho u_i u_j^2 \right] \quad (1.49)$$

$$= \frac{1}{2} \Pi_{ijj} + u_j \sigma_{ij} - u_i \rho E, \quad (1.50)$$

where we introduced the heat flux \mathbf{q} and the equation of energy balance becomes

$$\frac{\partial(\rho E)}{\partial t} + \frac{\partial(\rho u_i E)}{\partial x_i} = \frac{\partial(u_j \sigma_{ij})}{\partial x_i} + u_i F_{\mathcal{B}i} - \frac{\partial q_i}{\partial x_i}, \quad (1.51)$$

By multiplying 1.45 by $1/2 u_i$ and subtracting from the previous equation results in the equation of internal energy balance,

$$\frac{\partial(\rho e)}{\partial t} + \frac{\partial(\rho u_i e)}{\partial x_i} = \sigma_{ij} \frac{\partial u_j}{\partial x_i} - \frac{\partial q_i}{\partial x_i}, \quad (1.52)$$

We emphasize that in order to obtain the balance equations Eqs. (1.41), (1.45), and (1.52), no other assumptions than the conservation of mass, momentum and energy during the collision are made. Neither an explicit collision operator nor the form of the distribution functions are required to derive these macroscopic conservation equations. Nonetheless, the stress tensor σ_{ij} and the heat flux q_i depend on the distribution function. Contrary to the continuity equation, the momentum and energy balance will be fully determined when the expression of f is given.

Chapter 2

Lattice Boltzmann method

Before presenting the lattice Boltzmann method (LBM), we recall that the classical kinetic theory of gases is based on different assumptions, which can, to some extent, limit its applicability. First, we consider only binary collisions, thus this theory is not appropriate for dense gases and liquids where three-body collisions are significant. Nevertheless, Enskog and Eyring approximate theories have been proposed to deal with respectively dense gases and liquids [1]. Second, the use of classical mechanics excludes low-temperature phenomena where quantum effects are no longer negligible. Third, we impose that the mean free path, i.e., the average distance traversed by a particle between collisions, is short compared to all macroscopic dimensions. Otherwise, the gas behaves as a discontinuous medium and the concept of local density, velocity, and energy loses meaning. Fourth, monatomic spherical molecules are considered. In practice, the results can be also applied to polyatomic gases provided that a correction is added to take into account the internal degrees of freedom and molecules are not too non-spherical.

What is the lattice Boltzmann method? The lattice Boltzmann method is a particular discretization of the Boltzmann equation with a BGK, or an equivalent, collision operator. The lattice Boltzmann method can be derived in different ways. The first route is based on the kinetic theory of dilute gases and the discretization of the Boltzmann equation (also called bottom-up or *a posteriori* approach). In the second route the lattice Boltzmann method is constructed from a top-down or *a priori* strategy in such a way that the Navier-Stokes equations are recovered using minimal mesoscopic requirements. Both approaches are not equivalent but rather complementary. The first way has a rigorous historical foundation from statistical mechanics. Due to its kinetic representation, mesoscopic effects can be directly modeled and hydrodynamics beyond the Navier-Stokes equations can also be obtained [5]. However, this involves the aforementioned limitations, which seems to greatly restrict its applicability on hydrodynamic flows. On the contrary, the second way requires less unnecessary assumptions considering a fluid parcel instead of a molecule of gas. The reader may have already noticed, we follow the first route because of its fascinating physical insight and most importantly it provides some expressions for the transport coefficients of gaseous mixtures as we will show later. For the sake of brevity, we do not discuss the ancestor of the lattice Boltz-

mann method: the lattice gas cellular automata. A concise presentation can be found in Ref. [6]. Finally, a third noteworthy route begins directly from the discrete lattice Boltzmann equation, which is solely seen as a mesoscopic scheme for any distribution function with no relation with the Boltzmann equation. The number of discrete kinetic velocities and the equilibrium state are tailored to solve a particular partial differential equation. This expands out the lattice Boltzmann method into a numerical solver. Hence, the lattice Boltzmann method has been employed to solve, to name a few, the linear convection-diffusion equation [7] and nonlinear equations such as Ginzburg-Landau, Burgers-Fisher, nonlinear heat conduction, and sine-Gordon equations [8], or Burgers, Korteweg-de Vries, and Kuramoto-Sivashinsky equations [9], the wave equation [10], the shallow water equations [11].

In the following sections, the lattice Boltzmann method is derived from the Boltzmann equation. The reader may ask why using the lattice Boltzmann method for solving fluid flows instead of Navier-Stokes equations. Indeed for fluid dynamics, hydrodynamic quantities depend on the physical space \mathbf{x} and the time t , and the microscopic velocities do not appear in the fluids equations. The kinetic representation seems unnecessary involving the time, the velocity space, and the physical space; yet in addition to its appealing mesoscopic view of the flow, the lattice Boltzmann method has two other main advantages compared to the traditional way of solving Navier-Stokes equations. First, the advection in the Boltzmann equation, $\mathbf{c} \cdot \nabla f$, is linear whereas the inertial term in the Navier-Stokes equation is $\mathbf{u} \cdot \nabla \mathbf{u}$ where \mathbf{u} may be a complicated function of space and time. Secondly, the momentum diffusion in the lattice Boltzmann method is materialized by the relaxation process of the BGK collision operator, which is non-linear but local. Because of these two advantages, as we will see, the resulting discrete equation is conceptually simple, efficient, and can easily be implemented on parallel architectures, while still being rigorously based on the kinetic theory of gases. These reasons may explain the rapid and growing interest in the lattice Boltzmann method for solving fluid flows.

2.1 Non-dimensional formulation

It is often convenient to use non-dimensional quantities and equations during mathematical manipulations. Let define a characteristic length l_0 , velocity v_0 , and density ρ_0 . The characteristic time scale is given by $t_0 = l_0/v_0$. We introduce the non-dimensional derivatives

$$\frac{\partial}{\partial t^*} = \frac{l_0}{v_0} \frac{\partial}{\partial t}, \quad \frac{\partial}{\partial x_i^*} = l_0 \frac{\partial}{\partial x_i}, \quad \frac{\partial}{\partial c_i^*} = v_0 \frac{\partial}{\partial c_i}, \quad (2.1)$$

where the stars denote non-dimensional quantities. The Boltzmann equation Eq. (1.6) is written in a non-dimensional form

$$\frac{\partial f^*}{\partial t^*} + c_i^* \left(\frac{\partial f^*}{\partial x_i^*} \right) + \frac{F_{Bi}^*}{\rho^*} \left(\frac{\partial f^*}{\partial c_i^*} \right) = \left(\frac{df}{dt} \right)_{coll}^*, \quad (2.2)$$

with $f^* = v_0^d/\rho_0 f$, $\rho^* = \rho/\rho_0$, $c_i^* = c_i/v_0$, $F_{\mathcal{B}i}^* = l_0/v_0^2/\rho_0 F_{\mathcal{B}i}$, and $(df/dt)_{coll}^* = v_0^d/\rho_0 l_0/v_0 (df/dt)_{coll}$, and d is the number of spatial dimensions. Moreover, the equilibrium distribution function has the following non-dimensional form

$$f^{eq*} = \frac{\rho^*}{(2\pi\theta^*)^{d/2}} e^{-(\mathbf{c}^* - \mathbf{u}^*)^2/(2\theta^*)}, \quad (2.3)$$

and $\theta^* = R_s T/v_0^2$ is the non-dimensional temperature. Henceforth, the star notation will be omitted and all quantities will be non-dimensional unless otherwise stated.

2.2 Discretization of the velocity space

Usually, there is no analytical solution of the continuum Boltzmann equation instead the equation will be solved numerically. The distribution function spans over a seven-dimensional space: $t, \mathbf{x}, \mathbf{c}$, which has to be discretized. We first address the velocity space discretization. We point out that we are not interesting in the microscopic level of detail but a correct macroscopic behavior of the flow. As we already saw, only the moments of the distribution function appear in the macroscopic equations. As a result, we are only looking for a discrete distribution function whose moments, weighted integrals, are equivalent to the moments of the continuous distribution function.

2.2.1 Hermite series

The distribution function can be expanded as a series of Hermite polynomials in velocity space \mathbf{c} (see Appendix A and references [4, 5, 12] for more details)

$$f(\mathbf{x}, \mathbf{c}, t) = \omega(\mathbf{c}) \sum_{n=0}^{\infty} \frac{1}{n!} \mathbf{a}_i^{(n)}(\mathbf{x}, t) \mathbf{H}_i^{(n)}(\mathbf{c}), \quad (2.4)$$

with the following expansion coefficients and weight function

$$\mathbf{a}_i^{(n)}(\mathbf{x}, t) = \int f(\mathbf{x}, \mathbf{c}, t) \mathbf{H}_i^{(n)}(\mathbf{c}) d\mathbf{c}, \quad \omega(\mathbf{c}) = \frac{1}{(2\pi)^{d/2}} e^{-\mathbf{c}^2/2}. \quad (2.5)$$

One of the nice features of this formulation is that all the expansion coefficients are linear combinations of the moments of f . Substituting the Hermite polynomials by their expression Eqs. (A.16-A.19), we can identify the first few expansion coefficients with the hydrodynamic quantities

$$a^{(0)} = \int f d\mathbf{c} = \rho, \quad (2.6)$$

$$a_i^{(1)} = \int c_i f d\mathbf{c} = \rho u_i, \quad (2.7)$$

$$a_{ij}^{(2)} = \int (c_i c_j - \delta_{ij}) f d\mathbf{c} = \Pi_{ij} - \delta_{ij} \rho = -\sigma_{ij} + \rho(u_i u_j - \delta_{ij}), \quad (2.8)$$

$$a_{ijk}^{(3)} = \int (c_i c_j c_k - c_i \delta_{jk} - c_j \delta_{ki} - c_k \delta_{ij}) f d\mathbf{c} = \Pi_{ijk} - \rho(u_i \delta_{jk} + u_j \delta_{ki} + u_k \delta_{ij}). \quad (2.9)$$

We can limit the series Eq. (2.4) up to a certain order N . Also, the N -th expansion coefficients are still valid by truncation of higher-order terms. Therefore, we consider only the first N Hermite polynomials

$$f^N(\mathbf{x}, \mathbf{c}, t) \approx \omega(\mathbf{c}) \sum_{n=0}^N \frac{1}{n!} \mathbf{a}_i^{(n)}(\mathbf{x}, t) \mathbf{H}_i^{(n)}(\mathbf{c}). \quad (2.10)$$

This is one of the reasons why the Hermite expansion is ingenious to describe the distribution function in the Boltzmann equation. Since the coefficients of the expansion are related to or coincide with the moments of f , i.e., the hydrodynamic quantities; only a few truncated Hermite polynomials are needed to recover the relevant macroscopic physics. This is the key idea of the Grad 13th-moments equations.

As previously, the equilibrium distribution function is also expanded. Noticing that Eq. (2.3) can be written in the following form

$$f^{eq}(\mathbf{x}, \mathbf{c}, t) = \frac{\rho}{(\sqrt{\theta})^d} \omega\left(\frac{\mathbf{c} - \mathbf{u}}{\sqrt{\theta}}\right), \quad (2.11)$$

and using the change of variable $\boldsymbol{\zeta} = (\mathbf{c} - \mathbf{u})/\sqrt{\theta}$ yield

$$\mathbf{a}_i^{(n)eq}(\mathbf{x}, t) = \rho \int \omega(\boldsymbol{\zeta}) \mathbf{H}_i^{(n)}(\sqrt{\theta}\boldsymbol{\zeta} + \mathbf{u}) d\boldsymbol{\zeta}. \quad (2.12)$$

The expression of the equilibrium expansion coefficients are known exactly and the first few equilibrium expansion coefficients read

$$a^{(0)eq} = \rho \int \omega(\boldsymbol{\zeta}) d\boldsymbol{\zeta} = \rho. \quad (2.13)$$

Successive expressions are easily calculated using the orthogonality property of the Hermite polynomials (see Eq. (A.20)). For instance,

$$a_i^{(1)eq} = \rho \int \omega(\boldsymbol{\zeta}) H_i^{(1)}(\sqrt{\theta}\boldsymbol{\zeta} + \mathbf{u}) d\boldsymbol{\zeta} \quad (2.14)$$

$$= \rho \left[\sqrt{\theta} \int \omega(\boldsymbol{\zeta}) \zeta_i d\boldsymbol{\zeta} + u_i \int \omega(\boldsymbol{\zeta}) d\boldsymbol{\zeta} \right] \quad (2.15)$$

$$= \rho \left[\sqrt{\theta} \int \omega(\boldsymbol{\zeta}) H_i^{(1)}(\boldsymbol{\zeta}) d\boldsymbol{\zeta} + u_i \right] \quad (2.16)$$

$$= \rho \left[\sqrt{\theta} \int \omega(\boldsymbol{\zeta}) H^{(0)}(\boldsymbol{\zeta}) H_i^{(1)}(\boldsymbol{\zeta}) d\boldsymbol{\zeta} + u_i \right] \quad (2.17)$$

$$= \rho u_i, \quad (2.18)$$

Similarly,

$$a_{ij}^{(2)eq} = \rho u_i u_j + \rho(\theta - 1) \delta_{ij}, \quad (2.19)$$

$$a_{ijk}^{(3)eq} = \rho u_i u_j u_k + \rho(\theta - 1)(u_i \delta_{jk} + u_j \delta_{ki} + u_k \delta_{ij}). \quad (2.20)$$

The last term to expand (up to the N -th order) is related to the body forces. If we take the derivative related to the velocity of Eq. (2.4) and use Eq. (A.14) successively, we have

$$\nabla_{\mathbf{c}} f(\mathbf{x}, \mathbf{c}, t) = \sum_{n=0}^N \frac{1}{n!} \mathbf{a}_i^{(n)}(\mathbf{x}, t) \nabla_{\mathbf{c}} \left(\omega(\mathbf{c}) \mathbf{H}_i^{(n)}(\mathbf{c}) \right) \quad (2.21)$$

$$= \sum_{n=0}^N \frac{(-1)^n}{n!} \mathbf{a}_i^{(n)}(\mathbf{x}, t) \nabla_{\mathbf{c}}^{n+1} \left(\omega(\mathbf{c}) \right) \quad (2.22)$$

$$= -\omega(\mathbf{c}) \sum_{n=0}^N \frac{1}{n!} \mathbf{a}_i^{(n)}(\mathbf{x}, t) \mathbf{H}_i^{(n+1)}(\mathbf{c}) \quad (2.23)$$

$$= -\omega(\mathbf{c}) \sum_{n=1}^N \frac{1}{(n-1)!} \mathbf{a}_i^{(n-1)}(\mathbf{x}, t) \mathbf{H}_i^{(n)}(\mathbf{c}). \quad (2.24)$$

2.2.2 Gauss-Hermite quadrature

The last step is to evaluate the integrals in the expansion coefficients. If we truncate the expansion of the distribution function as in Eq. (2.10), the integrand of Eq. (2.5) has the following form

$$f^N(\mathbf{x}, \mathbf{c}, t) \mathbf{H}_i^{(n)}(\mathbf{c}) = \omega(\mathbf{c}) P(\mathbf{x}, \mathbf{c}, t), \quad (2.25)$$

where P is a multi-dimensional polynomial in \mathbf{c} of a degree not greater than $2N$. A Gauss-Hermite quadrature (see Appendix A) is of course employed to compute the expansion coefficient

$$\mathbf{a}_i^{(n)}(\mathbf{x}, t) = \int \omega(\mathbf{c}) P(\mathbf{x}, \mathbf{c}, t) d\mathbf{c} = \sum_{\alpha=0}^{q^d} \omega_{\alpha} P(\mathbf{x}, \mathbf{c}_{\alpha}, t) = \sum_{\alpha=0}^{q^d} \frac{\omega_{\alpha}}{\omega(\mathbf{c}_{\alpha})} f^N(\mathbf{x}, \mathbf{c}_{\alpha}, t) \mathbf{H}_i^{(n)}(\mathbf{c}_{\alpha}) \quad (2.26)$$

with $2q - 1 \geq 2N$. Finally we define

$$f_{\alpha}(\mathbf{x}, t) = \frac{\omega_{\alpha}}{\omega(\mathbf{c}_{\alpha})} f^N(\mathbf{x}, \mathbf{c}_{\alpha}, t), \quad (2.27)$$

and the moment of the distribution function are now

$$\rho = \sum_{\alpha=1}^{q^d} f_{\alpha}, \quad (2.28)$$

$$\rho u_i = \sum_{\alpha=1}^{q^d} c_{\alpha i} f_{\alpha}, \quad (2.29)$$

$$\Pi_{ij} = \sum_{\alpha=1}^{q^d} c_{\alpha i} c_{\alpha j} f_{\alpha}, \quad (2.30)$$

$$\Pi_{ijk} = \sum_{\alpha=1}^{q^d} c_{\alpha i} c_{\alpha j} c_{\alpha k} f_{\alpha}. \quad (2.31)$$

The corresponding equation for f_α is obtained by evaluating at \mathbf{c}_α the Boltzmann equation, Eq. (1.6) and multiplying by $\omega_\alpha/\omega(\mathbf{c})$,

$$\frac{\partial f_\alpha}{\partial t} + \mathbf{c}_\alpha \cdot \nabla f = -\frac{1}{\tau} (f_\alpha - f_\alpha^{eq}) + S_\alpha, \quad (2.32)$$

where the BGK collision operator is employed to model collisions. The discrete equilibrium f_α^{eq} is given by

$$f_\alpha^{eq}(\mathbf{x}, t) = \omega_\alpha \sum_{n=0}^N \frac{1}{n!} \mathbf{a}_i^{(n)eq}(\mathbf{x}, t) \mathbf{H}_i^{(n)}(\mathbf{c}_\alpha), \quad (2.33)$$

and the effect of the body force is absorbed into the source term discrete S_α ,

$$S_\alpha(\mathbf{x}, t) = \frac{\mathbf{F}_B}{\rho} \cdot \omega_\alpha \sum_{n=1}^N \frac{1}{(n-1)!} \mathbf{a}_i^{(n-1)}(\mathbf{x}, t) \mathbf{H}_i^{(n)}(\mathbf{c}_\alpha). \quad (2.34)$$

2.3 Discrete velocity sets

In practice, most lattice Boltzmann implementations employ a Gauss-Hermite quadrature whose abscissas coincide with Cartesian coordinates. This corresponds to the velocity sets called $D1Q3$, $D2Q9$, $D3Q15$, $D3Q19$, and $D3Q27$; following the standard $DdQq$ where d is the spatial dimension and q the number of velocities, i.e., abscissas.

All the previous quadratures are exact for a (multi-dimensional) polynomial of a fifth-degree or less. That is why only the second-order Hermite terms have to be retained ($5 \geq 2N \implies N = 2$). The third-order expansion coefficient $\mathbf{a}_i^{(3)}$ is not conserved by the truncation and the energy balance is no longer respected. Consequently, exclusively isothermal flows will be considered. Higher-order Gauss-Hermite quadratures are possible but they are out of the scope of this thesis ($D2Q17$ and $D3Q39$ for a Cartesian uniform grid are exact quadratures for polynomials of a seventh-degree or less [5]).

If we set the non-dimensional temperature to $\theta = 1$ and go back to the non-dimensional formulation Eq. 2.2, the characteristic velocity is $v_0 = \sqrt{R_s T}$, which corresponds to the speed of sound and the characteristic length is the distance traveled by a sound wave in a unit of time. However, the abscissas in Appendix A contain a cumbersome $\sqrt{3}$ factor so instead the characteristic length is scaled so as the lattice spacing is equal to one. That is why a scaled abscissa \mathbf{e}_α is used in place of,

$$\mathbf{e}_\alpha = \mathbf{c}_\alpha c_s, \quad (2.35)$$

where the scaled factor is set to $c_s = c/\sqrt{3}$ with usually $c = 1$ and, as we will show, is related to the reference speed of sound. The resulting velocity sets are summarized in Table 2.1 and are drawn in Fig. 2.1.

Therefore, the non-dimensional quantities \mathbf{u} , \mathbf{F}_B , and ∇ have also to be appropriately scaled by the factor c_s and the resulting equations are

$$\frac{\partial f_\alpha}{\partial t} + \mathbf{e}_\alpha \cdot \nabla f_\alpha = -\frac{1}{\tau} (f_\alpha - f_\alpha^{eq}) + S_\alpha, \quad (2.36)$$

$DdQq$	Velocities	Weights
$D1Q3$	(0)	2/3
	(± 1)	1/6
$D2Q9$	(0, 0)	4/9
	($\pm 1, 0$), (0, ± 1)	1/9
	($\pm 1, \pm 1$)	1/36
$D3Q15$	(0, 0, 0)	2/9
	($\pm 1, 0, 0$), (0, $\pm 1, 0$), (0, 0, ± 1)	1/9
	($\pm 1, \pm 1, \pm 1$)	1/72
$D3Q19$	(0, 0, 0)	1/3
	($\pm 1, 0, 0$), (0, $\pm 1, 0$), (0, 0, ± 1)	1/18
	($\pm 1, \pm 1, 0$), ($\pm 1, 0, \pm 1$), (0, $\pm 1, \pm 1$)	1/36
$D3Q27$	(0, 0, 0)	8/27
	($\pm 1, 0, 0$), (0, $\pm 1, 0$), (0, 0, ± 1)	2/27
	($\pm 1, \pm 1, 0$), ($\pm 1, 0, \pm 1$), (0, $\pm 1, \pm 1$)	1/54
	($\pm 1, \pm 1, \pm 1$)	1/216

Table 2.1 – Common velocity sets used in the lattice Boltzmann method for $c_s = 1/\sqrt{3}$. If $c \neq 1$, velocities have to be multiplied by c .

where the equilibrium and the source terms are expanded up to the second-order

$$f_\alpha^{eq} = \rho \omega_\alpha \left[1 + \frac{\mathbf{u} \cdot \mathbf{e}_\alpha}{c_s^2} + \frac{(\mathbf{u} \cdot \mathbf{e}_\alpha)^2}{2c_s^4} - \frac{\mathbf{u} \cdot \mathbf{u}}{2c_s^2} \right], \quad (2.37)$$

$$S_\alpha = \omega_\alpha \left[\frac{\mathbf{e}_\alpha - \mathbf{u}}{c_s^2} + \frac{(\mathbf{e}_\alpha \cdot \mathbf{u})\mathbf{e}_\alpha}{c_s^4} \right] \cdot \mathbf{F}_B. \quad (2.38)$$

One can show that the moment of the equilibrium and the source term are given by

$$\Pi_0^{eq} = \sum_\alpha f_\alpha^{eq} = \rho, \quad \sum_\alpha S_\alpha = 0, \quad (2.39)$$

$$\Pi_i^{eq} = \sum_\alpha e_{\alpha i} f_\alpha^{eq} = \rho u_i, \quad \sum_\alpha e_{\alpha i} S_\alpha = F_{Bi}, \quad (2.40)$$

and,

$$\Pi_{ij}^{eq} = \sum_\alpha e_{\alpha i} e_{\alpha j} f_\alpha^{eq} = \rho c_s^2 \delta_{ij} + \rho u_i u_j, \quad (2.41)$$

$$\sum_\alpha e_{\alpha i} e_{\alpha j} S_\alpha = u_i F_{Bj} + u_j F_{Bi}, \quad (2.42)$$

$$\Pi_{ijk}^{eq} = \sum_\alpha e_{\alpha i} e_{\alpha j} e_{\alpha k} f_\alpha^{eq} = \rho c_s^2 (u_i \delta_{jk} + u_j \delta_{ki} + u_k \delta_{ij}), \quad (2.43)$$

$$\sum_\alpha e_{\alpha i} e_{\alpha j} e_{\alpha k} S_\alpha = c_s^2 (F_i \delta_{jk} + F_j \delta_{ki} + F_k \delta_{ij}), \quad (2.44)$$

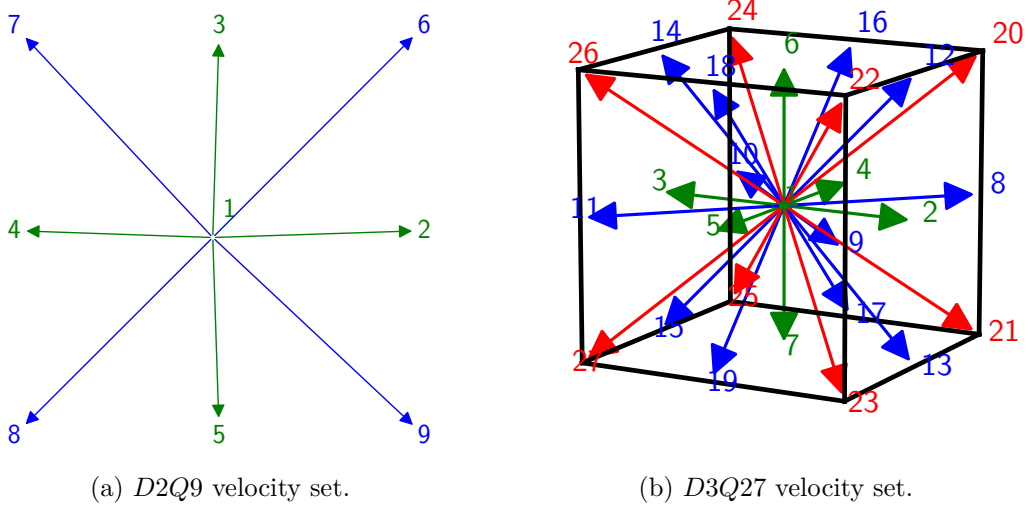


Figure 2.1 – Common velocity sets in the lattice Boltzmann method. $D1Q3$ is equivalent to 1, 2, 4 velocities of $D2Q9$. Degenerate velocity sets can be obtained from $D3Q27$: $D3Q15$ by considering the velocities 1–7 (green) and 20–27 (red), $D3Q19$ by considering the velocities 1 – 7 (green) and 8 – 19 (blue).

where the following relations have been used

$$\sum_{\alpha} \omega_{\alpha} = 1, \quad (2.45)$$

$$\sum_{\alpha} \omega_{\alpha} e_{\alpha i} = 0, \quad (2.46)$$

$$\sum_{\alpha} \omega_{\alpha} e_{\alpha i} e_{\alpha j} = c_s^2 \delta_{ij}, \quad (2.47)$$

$$\sum_{\alpha} \omega_{\alpha} e_{\alpha i} e_{\alpha j} e_{\alpha k} = 0, \quad (2.48)$$

$$\sum_{\alpha} \omega_{\alpha} e_{\alpha i} e_{\alpha j} e_{\alpha k} e_{\alpha l} = c_s^4 (\delta_{ij} \delta_{kl} + \delta_{ik} \delta_{jl} + \delta_{il} \delta_{jk}), \quad (2.49)$$

$$\sum_{\alpha} \omega_{\alpha} e_{\alpha i} e_{\alpha j} e_{\alpha k} e_{\alpha l} e_{\alpha m} = 0. \quad (2.50)$$

2.4 Discretization of physical space and time

The Boltzmann equation has been discretized in the velocity space however, we still need to discretize the time and physical space in order to solve it numerically. One can use any numerical schemes such as finite differences, finite volumes, or finite elements but Eq. (2.36) is a hyperbolic partial differential equation. An efficient way to solve this kind of partial differential equations is the method of characteristics. The distribution function is rewritten as $f_{\alpha} = f_{\alpha}(\mathbf{x}(s), t(s))$ where s is the position along

the characteristic line $(\mathbf{x}(s), t(s))$. Along these characteristics, the partial differential equation reduces to an ordinary differential equation,

$$\frac{df_\alpha}{ds} = \frac{\partial f_\alpha}{\partial t} \frac{dt}{ds} + \frac{\partial f_\alpha}{\partial x_i} \frac{dx_i}{ds} = -\frac{1}{\tau} (f_\alpha - f_\alpha^{eq}) + S_\alpha. \quad (2.51)$$

This previous equation is equivalent to the discrete velocity Boltzmann equation Eq. (2.36) if

$$\frac{dt}{ds} = 1, \quad \frac{dx_i}{ds} = e_{\alpha i}. \quad (2.52)$$

Letting $t(0) = t$ and $x_i(0) = x_i$, we find $t(s) = t + s$ and $x_i(s) = x + e_{\alpha i} s$. We integrate Eq. (2.51) over a time step, from $s = 0$ to $s = \delta_t$,

$$\begin{aligned} f_\alpha(\mathbf{x} + \mathbf{e}_\alpha \delta_t, t + \delta_t) - f_\alpha(\mathbf{x}, t) = \\ \int_0^{\delta_t} \left\{ -\frac{1}{\tau} [f_\alpha(\mathbf{x} + \mathbf{e}_\alpha s, t + s) - f_\alpha^{eq}(\mathbf{x} + \mathbf{e}_\alpha s, t + s)] + S_\alpha(\mathbf{x} + \mathbf{e}_\alpha s, t + s) \right\} ds \end{aligned} \quad (2.53)$$

The integral is evaluated using the trapezoidal rule.

$$\begin{aligned} f_\alpha(\mathbf{x} + \mathbf{e}_\alpha \delta_t, t + \delta_t) - f_\alpha(\mathbf{x}, t) = \\ -\frac{\delta_t}{2\tau} [f_\alpha(\mathbf{x} + \mathbf{e}_\alpha \delta_t, t + \delta_t) - f_\alpha^{eq}(\mathbf{x} + \mathbf{e}_\alpha \delta_t, t + \delta_t) + f_\alpha(\mathbf{x}, t) - f_\alpha^{eq}(\mathbf{x}, t)] \\ + \frac{\delta_t}{2} [S_\alpha(\mathbf{x} + \mathbf{e}_\alpha \delta_t, t + \delta_t) + S_\alpha(\mathbf{x}, t)] \quad (+O(\delta_t^3)) \end{aligned} \quad (2.54)$$

This is a second-order accurate discretization but the resulting equation is implicit. If we introduce the change of variable

$$\hat{f}_\alpha = \left(1 + \frac{\delta_t}{2\tau}\right) f_\alpha - \frac{\delta_t}{2\tau} f_\alpha^{eq} - \frac{\delta_t}{2} S_\alpha, \quad (2.55)$$

the previous equation gives

$$\hat{f}_\alpha(\mathbf{x} + \mathbf{e}_\alpha \delta_t, t + \delta_t) = \hat{f}_\alpha(\mathbf{x}, t) - \frac{\delta_t}{\hat{\tau}} [\hat{f}_\alpha(\mathbf{x}, t) - \hat{f}_\alpha^{eq}(\mathbf{x}, t)] + \delta_t \left(1 - \frac{\delta_t}{2\hat{\tau}}\right) S_\alpha, \quad (2.56)$$

with $\hat{f}_\alpha^{eq} = f_\alpha^{eq}$ and $\hat{\tau} = \tau + \delta_t/2$. Surprisingly, with this change of variable, the equation becomes explicit and is second-order accurate despite having a similar form as a first-order discretization. This is another interesting property of the lattice Boltzmann method. The macroscopic quantities are obtained by computing the moment of \hat{f}_α :

$$\sum_\alpha \hat{f}_\alpha = \rho, \quad (2.57)$$

$$\sum_\alpha \mathbf{e}_\alpha \hat{f}_\alpha = \rho \mathbf{u} - \frac{\delta_t}{2} \mathbf{F}_B, \quad (2.58)$$

and similarly, other quantities can be directly calculated from \hat{f}_α . Hence and from now, the $\hat{\cdot}$ notation will be omitted, and f_α and τ will refer to the transformed variables.

In the lattice Boltzmann method, a convenient system of units called lattice units (lu) is commonly employed. In this system, the time and space steps are set equal to one. Conversion factors and non-dimensional numbers are then used to compare the simulation with experimental or numerical results. For instance, in lattice units we usually set $\delta x_{LBM} = 1$, $\delta t_{LBM} = 1$, and $\rho_{LBM} = 1$ whereas in physical system we have δx_{phy} , δt_{phy} , and ρ_{phy} . The conversion factors from the lattice units to the physical system are simply for the length $C_l = \delta x_{phy}$, the time $C_t = \delta t_{phy}$ and density $C_\rho = \rho_{phy}$. We emphasize that whatever the system of units is considered all the dimensionless numbers are equal. Let consider for example the Mach number

$$\text{Ma} = \frac{U_{phy}}{c_{phy}} = \frac{U_{LBM}}{c_s}, \quad (2.59)$$

$$= \frac{U_{phy}}{U_{LBM}} = \frac{C_l}{C_t} = \frac{\delta x_{phy}}{\delta t_{phy}} = \frac{c_{phy}}{c_s} = \sqrt{3} \times c_{phy}. \quad (2.60)$$

In consequence, setting the Mach number gives a relationship between the physical space and time steps of the simulation $\text{Ma} = \delta x_{phy}/\delta t_{phy} = c_{phy}\sqrt{3}$.

Finally, the lattice Boltzmann method can be split into two main steps and is summarized below:

$$f_\alpha^*(\mathbf{x}, t) = f_\alpha(\mathbf{x}, t) - \frac{1}{\tau} [f_\alpha(\mathbf{x}, t) - f_\alpha^{eq}(\mathbf{x}, t)] + (1 - \frac{1}{2\tau}) S_\alpha \quad \text{Collision,} \quad (2.61)$$

$$f_\alpha(\mathbf{x} + \mathbf{e}_\alpha, t + 1) = f_\alpha^*(\mathbf{x}, t) \quad \text{Streaming,} \quad (2.62)$$

with

$$\rho = \sum_\alpha f_\alpha, \quad f_\alpha^{eq} = \rho \omega_\alpha \left[1 + \frac{\mathbf{u} \cdot \mathbf{e}_\alpha}{c_s^2} + \frac{(\mathbf{u} \cdot \mathbf{e}_\alpha)^2}{2c_s^4} - \frac{\mathbf{u} \cdot \mathbf{u}}{2c_s^2} \right], \quad (2.63)$$

$$\rho \mathbf{u} = \sum_\alpha \mathbf{e}_\alpha f_\alpha + \frac{1}{2} \mathbf{F}_B, \quad S_\alpha = \omega_\alpha \left[\frac{\mathbf{e}_\alpha - \mathbf{u}}{c_s^2} + \frac{(\mathbf{e}_\alpha \cdot \mathbf{u}) \mathbf{e}_\alpha}{c_s^4} \right] \cdot \mathbf{F}_B. \quad (2.64)$$

The first step is called collision and is purely local. The formulation of the source term expressed up to the second-order is the same as Guo's forcing scheme [13] obtained *a priori* so as to derive the correct Force expression in the Navier-Stokes equations. The second step is the streaming, which propagates the distribution functions to the neighboring lattice points. The advantage of a quadrature whose abscissas coincide with the Cartesian coordinates is evident. If \mathbf{x} belongs to a lattice node, then $\mathbf{x} + \mathbf{e}_\alpha$ is also a lattice point. The streaming step is just a shift of the post-collision distribution functions to the next lattice nodes. The advection is exact, there is no diffusion added by the use of an interpolation scheme for instance. The implementation of the algorithm is straightforward (see Algo. 1 and Fig. 2.2).

The final result is conceptually simple yet physically based on the kinetic theory of gases. The algorithm is very efficient as all steps but the streaming are local and the non-locality (propagation) is just a shift in the memory involving the next neighbored lattice nodes. Moreover, the code can easily be parallelized and achieves high performance on multi-core computers. For instance, using the Message-Passing Interface

```

while  $t \leq t_{max}$  do
  collide;
  do MPI communications;
  stream;
  apply boundary conditions;
  compute moments and force,  $\rho$ ,  $\rho\mathbf{u}$ ,  $\mathbf{F}_B$ ;
   $t = t + \delta_t$ ;
end

```

Algorithm 1: Lattice Boltzmann algorithm

(MPI) paradigm, the computational domain is expanded with a layer of ghost nodes. These ghost nodes store a copy of the neighboring node from the adjacent MPI process and are updated just before the streaming step as shown in Algo. 1 since other steps are local. More details concerning programming considerations can be found in Appendix B.

2.5 Chapman and Enskog expansion procedure

As we know, the order of expansion of the Hermite series predicts which moments we can exactly recover from the truncation of higher orders. However, the macroscopic equations are not completely closed and the expression of Π_{ij} , for instance, in terms of hydrodynamic quantities is still required. We need a way to assess the level of accuracy over the different scales of the physics. The Chapman and Enskog expansion estimates, from the deviation of the equilibrium, the relevant physical scales that are solved. The distribution functions are expanded in terms of powers of the Knudsen number [2]:

$$f_\alpha = f_\alpha^{(0)} + \mathcal{K}f_\alpha^{(1)} + \mathcal{K}^2f_\alpha^{(2)} + \dots, \quad (2.65)$$

where \mathcal{K} is the Knudsen number, i.e., the mean free path divided by the characteristic length of the flow. The source term is often expanded as $S_\alpha = \mathcal{K}S_\alpha^{(1)}$, where higher-order terms are not generally required to obtain the correct macroscopic equations. For usual fluid flows with slow time and large spatial scales variations, the Knudsen number is small. The fluid behaves like a continuum and the Navier-Stokes description is valid. In other cases, such as in microfluidics, or rarefied gases, the Knudsen number is large ($\mathcal{K} \geq 0.1$) and higher orders are required in the expansion of Eq. (2.65) to describe phenomena beyond the Navier-Stokes level. Time and spatial variations are also expanded in terms of powers of \mathcal{K} [2] as follow:

$$\frac{\partial}{\partial t} = \partial_t = \mathcal{K}\partial_t^{(1)} + \mathcal{K}^2\partial_t^{(2)} + \dots, \text{ and } \frac{\partial}{\partial x_i} = \partial_i = \mathcal{K}\partial_i^{(1)} \quad (2.66)$$

Using this appropriate division of the derivatives is necessary because f_α is unknown and so as the momentum flux Π_{ij} . The determination of f_α by successive approximations is difficult because, as we will see, the time derivative of the hydrodynamics variables determines the time derivative of $f_\alpha^{(0)}$, on which the equation from which $f_\alpha^{(1)}$ is inferred

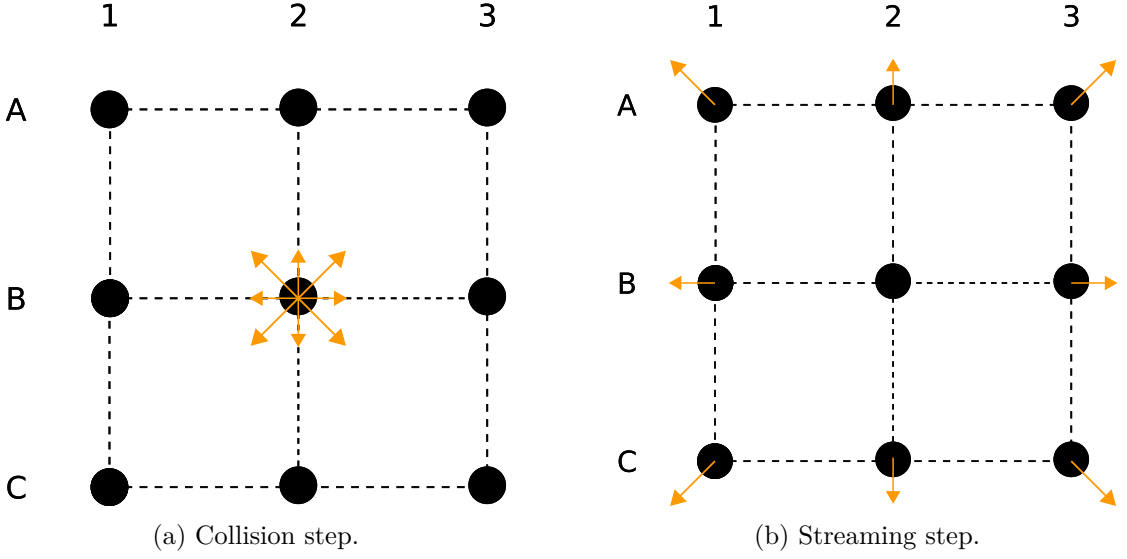


Figure 2.2 – Sketch of the collision and streaming step for the node B2 with the $D2Q9$ velocity set. Notice that f_0 associated with the vector $(0, 0)$ is not represented. The collision involves all the distribution functions from the node, after the streaming step propagates the distribution functions to the neighbor nodes according to the direction \mathbf{e}_α .

depends. The expansion of the time derivative proposed by Enskog allows to circumvent this difficulty [2].

We now apply the Chapman and Enskog expansion to the lattice Boltzmann equation Eqs. (2.61) and (2.62), nevertheless the expansion can also be applied to the Boltzmann equation [Eq. (1.6)] or its counterpart discretized in the velocity space [Eq. (2.36)]. Starting from

$$f_\alpha(\mathbf{x} + \mathbf{e}_\alpha, t + \delta_t) = f_\alpha(\mathbf{x}, t) - \frac{\delta_t}{\tau} [f_\alpha(\mathbf{x}, t) - f_\alpha^{eq}(\mathbf{x}, t)] + \delta_t \left(1 - \frac{\delta_t}{2\tau}\right) S_\alpha \quad (2.67)$$

The Taylor expansion up to the second-order of $f_\alpha(\mathbf{x} + \mathbf{e}_\alpha, t + \delta_t)$ gives

$$f_\alpha(\mathbf{x} + \mathbf{e}_\alpha, t + \delta_t) - f_\alpha(\mathbf{x}, t) = \delta_t (\partial_t + e_{\alpha i} \partial_i) f_\alpha + \frac{\delta_t^2}{2} (\partial_t + e_{\alpha i} \partial_i)^2 f_\alpha + O(\delta_t^3) \quad (2.68)$$

Applying this Taylor expansion to Eq. (2.67) and using the expansions of Eqs. (2.65) and (2.66), the resulting equation can be separated according to the different order of \mathcal{K} :

$O(\mathcal{K}^0)$:

$$f_\alpha^{(0)} = f_\alpha^{eq}, \quad (2.69)$$

$O(\mathcal{K}^1)$:

$$\left(\partial_t^{(1)} + e_{\alpha i} \partial_i^{(1)}\right) f_\alpha^{(0)} = -\frac{1}{\tau} f_\alpha^{(1)} + \left(1 - \frac{\delta_t}{2\tau}\right) S_\alpha^{(1)}, \quad (2.70)$$

$O(\mathcal{K}^2)$:

$$\partial_t^{(2)} f_\alpha^{(0)} + \left(\partial_t^{(1)} + e_{\alpha i} \partial_i^{(1)} \right) f_\alpha^{(1)} + \frac{\delta_t}{2} \left(\partial_t^{(1)} + e_{\alpha i} \partial_i^{(1)} \right)^2 f_\alpha^{(0)} = -\frac{1}{\tau} f_\alpha^{(2)}. \quad (2.71)$$

With the help of Eq. (2.70), the equation for the second-order $O(\mathcal{K}^2)$ is rewritten as

$$\partial_t^{(2)} f_\alpha^{(0)} + \left(\partial_t^{(1)} + e_{\alpha i} \partial_i^{(1)} \right) \left(1 - \frac{\delta_t}{2\tau} \right) \left(f_\alpha^{(1)} + \frac{\delta_t}{2} S_\alpha^{(1)} \right) = -\frac{1}{\tau} f_\alpha^{(2)}. \quad (2.72)$$

A very important remark from the observation of the equations of different orders of \mathcal{K} is the fact that we need the previous order $f_\alpha^{(k)}$ to compute $f_\alpha^{(k+1)}$. If we discard the source term for the sake of simplicity, we can write

$$f_\alpha^{(k+1)} = -\tau \left[\sum_{\beta=0}^k \partial_t^{(k)} f_\alpha^{(\beta)} + b_k \mathbf{e}_\alpha \cdot \nabla f_\alpha^{(k)} \right], \quad (2.73)$$

where b_k is an artefact due to the spatial and temporal discretization, e.g., $b_2 = (1 - \delta_t/2)$. If we recall the Hermite series of f up to order N , the term $e_\alpha \cdot \nabla f$ need an expansion of order $N+1$ in order to be described appropriately (see the recurrence relation Eq. (A.7)). That means if we want to correctly describe a flow at order $O(\mathcal{K}^k)$, the equilibrium and the distribution function have to be expanded up to order $N+k$ in the Hermite series. For the aforementioned quadratures of fifth-degree, $N=2$. Recalling that the Hermite expansion coefficient of order N is a linear combination of the moment of the distribution function up to the order N ; the zeroth, first, and second moments of $f^{(k=0)}$ are accurately depicted and so as the zeroth, first moments of $f^{(k=1)}$. That is why we can expect an error from the second moment of $f^{(k=1)}$ which is related to the pressure tensor in the Navier-Stokes equation as we will show shortly.

As expected, the Chapman and Enskog expansion analyses the asymptotic behavior of the (lattice) Boltzmann equation according to the deviation of the distribution functions from the equilibrium. Since $f_\alpha^{(0)} = f_\alpha^{eq}$, we have

$$\sum_\alpha f_\alpha = \rho = \sum_\alpha f_\alpha^{eq} = \sum_\alpha f_\alpha^{(0)} \implies \sum_\alpha f_\alpha^{(n)} = 0 \quad \forall n \geq 1, \quad (2.74)$$

and

$$\left. \begin{aligned} \sum_\alpha e_{\alpha i} f_\alpha &= \rho u_i - \frac{\delta_t}{2} F_{\mathcal{B}i} \\ \sum_\alpha e_{\alpha i} f_\alpha^{eq} &= \sum_\alpha e_{\alpha i} f_\alpha^{(0)} = \rho u_i \end{aligned} \right\} \implies \left\{ \begin{aligned} \sum_\alpha e_{\alpha i} f_\alpha^{(1)} &= -\frac{\delta_t}{2} F_{\mathcal{B}i} \\ \sum_\alpha e_{\alpha i} f_\alpha^{(n)} &= 0 \quad \forall n \geq 2 \end{aligned} \right. \quad (2.75)$$

where the right-hand side is consequence of the expansion $S_\alpha = \mathcal{K} S_\alpha^{(1)}$.

Let focus now on the order $O(\mathcal{K})$. Taking the zeroth, first, and second moments of Eq. (2.70) yields

$$\partial_t^{(1)} \rho + \partial_i^{(1)} (\rho u_i) = 0, \quad (2.76)$$

$$\partial_t^{(1)} (\rho u_i) + \partial_j^{(1)} \Pi_{ij}^{eq} = F_{\mathcal{B}i}, \quad (2.77)$$

$$\partial_t^{(1)} \Pi_{ij}^{eq} + \partial_k^{(1)} \Pi_{ijk}^{eq} = -\frac{1}{\tau} \Pi_{ij}^{(1)} + \left(1 - \frac{\delta_t}{2\tau} \right) (u_i F_{\mathcal{B}j} + u_j F_{\mathcal{B}i}), \quad (2.78)$$

with $\Pi_{ij}^{eq} = \rho u_i u_j + \rho c_s^2 \delta_{ij}$. The first two equations corresponds to the Euler equations where the pressure is defined as $p = \rho c_s^2$. Similarly, computing the zeroth and first moments of Eq. (2.72) gives

$$\partial_t^{(2)} \rho = 0, \quad (2.79)$$

$$\partial_t^{(2)}(\rho u_i) + \partial_j^{(1)} \left\{ \left(1 - \frac{\delta_t}{2\tau}\right) \left[\Pi_{ij}^{(1)} + \frac{\delta_t}{2} (u_i F_{\mathcal{B}j} + u_j F_{\mathcal{B}i}) \right] \right\} = 0. \quad (2.80)$$

$\Pi_{ij}^{(1)}$ is still unknown but can be expressed using the equations at order $O(\mathcal{K})$:

$$\Pi_{ij}^{(1)} = -\tau \left[\partial_t^{(1)} \Pi_{ij}^{eq} + \partial_k \Pi_{ijk}^{eq} - \left(1 - \frac{\delta_t}{2\tau}\right) (u_i F_{\mathcal{B}j} + u_j F_{\mathcal{B}i}) \right]. \quad (2.81)$$

Recalling that $\partial_i(abc) = a\partial_i(bc) + b\partial_i(ac) - ab\partial_i(c)$, we have

$$\begin{aligned} \partial_t^{(1)} \Pi_{ij}^{eq} &= \partial_t^{(1)} [\rho u_i u_j + \rho c_s^2 \delta_{ij}] \\ &= u_i \partial_t^{(1)}(\rho u_j) + u_j \partial_t^{(1)}(\rho u_i) - u_i u_j \partial_t^{(1)} \rho + c_s^2 \delta_{ij} \partial_t^{(1)} \rho \\ &= -u_i \left[\partial_k^{(1)}(\rho u_j u_k + \rho c_s^2 \delta_{jk}) - F_{\mathcal{B}j} \right] \\ &\quad - u_j \left[\partial_k^{(1)}(\rho u_i u_k + \rho c_s^2 \delta_{ki}) - F_{\mathcal{B}i} \right] \\ &\quad + u_i u_j \partial_k^{(1)}(\rho u_k) - c_s^2 \delta_{ij} \partial_k^{(1)}(\rho u_k) \\ &= - \left[u_i \partial_k^{(1)}(\rho u_j u_k) + u_j \partial_k^{(1)}(\rho u_i u_k) - u_i u_j \partial_k^{(1)}(\rho u_k) \right] \\ &\quad + u_i F_{\mathcal{B}j} + u_j F_{\mathcal{B}i} \\ &\quad - c_s^2 \left(u_i \partial_j^{(1)} \rho + u_j \partial_i^{(1)} \rho \right) - c_s^2 \delta_{ij} \partial_k^{(1)}(\rho u_k) \\ &= -\partial_k^{(1)}(\rho u_i u_j u_k) + u_i F_{\mathcal{B}j} + u_j F_{\mathcal{B}i} \\ &\quad - c_s^2 \left(u_i \partial_j^{(1)} \rho + u_j \partial_i^{(1)} \rho \right) - c_s^2 \delta_{ij} \partial_k^{(1)}(\rho u_k), \end{aligned}$$

and

$$\begin{aligned} \partial_k^{(1)} \Pi_{ijk}^{eq} &= \partial_k \left[\rho c_s^2 (u_i \delta_{jk} + u_j \delta_{ki} + u_k \delta_{ij}) \right] \\ &= c_s^2 \left[\partial_j^{(1)}(\rho u_i) + \partial_i^{(1)}(\rho u_j) \right] + c_s^2 \delta_{ij} \partial_k^{(1)}(\rho u_k). \end{aligned}$$

Finally, we get

$$\Pi_{ij}^{(1)} = -\tau \left[\rho c_s^2 (\partial_j^{(1)} u_i + \partial_i^{(1)} u_j) - \partial_k^{(1)}(\rho u_i u_j u_k) + \frac{\delta_t}{2\tau} (u_i F_{\mathcal{B}j} + u_j F_{\mathcal{B}i}) \right]. \quad (2.82)$$

The equation Eq. (2.80) can now be written explicitly

$$\partial_t^{(2)}(\rho u_i) + \partial_j^{(1)} \left\{ -\tau \left(1 - \frac{\delta_t}{2\tau}\right) \left[\rho c_s^2 (\partial_j^{(1)} u_i + \partial_i^{(1)} u_j) - \partial_k^{(1)}(\rho u_i u_j u_k) \right] \right\} = 0. \quad (2.83)$$

By gathering the equations from the different orders of \mathcal{K} [Eqs. (2.76), (2.77), (2.79), and (2.83)] and using Eq. (2.66), the Navier-Stokes equations are recovered

$$\begin{aligned} \frac{\partial \rho}{\partial t} + \frac{\partial(\rho u_i)}{\partial x_i} &= 0, \\ \frac{\partial(\rho u_i)}{\partial t} + \frac{\partial(\rho u_i u_j)}{\partial x_j} &= -\frac{\partial(\rho c_s^2)}{\partial x_i} + F_{\mathcal{B}i} \\ &+ \partial_j \left[\left(\tau - \frac{\delta_t}{2} \right) \rho c_s^2 \left(\frac{\partial u_i}{\partial x_j} + \frac{\partial u_j}{\partial x_i} \right) - \left(\tau - \frac{\delta_t}{2} \right) \frac{\partial(\rho u_i u_j u_k)}{\partial x_k} \right]. \end{aligned} \quad (2.84)$$

The pressure follows an ideal gas law and we can define

$$p = \rho c_s^2. \quad (2.86)$$

That is the reason why the factor c_s is called pseudo-speed of sound. As expected, the term $\Pi_{ij}^{(1)}$ contains an error, which stems from the viscous stress tensor in the Navier-Stokes equations. The error term $\partial_k(\rho u_i u_j u_k)$ is negligible if $c_s^2 \gg u^2$, which is equivalent to $\text{Ma} \ll 1$ where $\text{Ma} = u/c_s$ is the Mach number. Thus the lattice Boltzmann method is only valid for weakly compressible flows. The dynamic viscosity is related to the relaxation time and is identified as

$$\mu = \left(\tau - \frac{\delta_t}{2} \right) \rho c_s^2 \quad (2.87)$$

Note that the factor $\tau - \delta_t/2$ is an artifact due to the discretization of space and time. Applying the Chapman and Enskog expansion to the continuous equation will result in $\mu = \tau \rho c_s^2$. The volume viscosity seems to not appear in the momentum balance equation because the volume viscosity, also sometimes called bulk viscosity, is equal to $\zeta = 2/3\mu$. This dependence could be removed by using advanced collision operators and allowing different moments to relax to the equilibrium at different rates.

Last, it is possible to obtain explicitly the first order perturbation

$$f_\alpha^{(1)} = -\tau \left(\partial_t^{(1)} + e_{\alpha i} \partial_i^{(1)} \right) f_\alpha^{eq} + \left(\tau - \frac{\delta_t}{2} \right) S_\alpha^{(1)}. \quad (2.88)$$

where we recall the expression of the equilibrium distribution functions

$$f_\alpha^{eq} = \omega_\alpha \rho \left[1 + \frac{e_{\alpha i} u_i}{c_s^2} + \frac{Q_{\alpha ij} u_i u_j}{2c_s^4} \right], \quad (2.89)$$

with the tensor $Q_{\alpha ij} = (e_{\alpha i} e_{\alpha j} - c_s^2 \delta_{ij})$, and the source term can also be rewritten as

$$S_\alpha = \omega_\alpha \left[\frac{e_{\alpha i}}{c_s^2} + \frac{Q_{\alpha ij} u_j}{c_s^4} \right] F_{\mathcal{B}i}. \quad (2.90)$$

After some algebra we have

$$\begin{aligned} \partial_t^{(1)} f_\alpha^{eq} &= -\omega_\alpha \left\{ \partial_i^{(1)}(\rho u_i) + e_{\alpha i} \partial_i^{(1)} \rho + \frac{e_{\alpha i}}{c_s^2} \left[\partial_j^{(1)}(\rho u_i u_j) - F_{\mathcal{B}i} \right] \right. \\ &\quad \left. + \frac{Q_{\alpha ij}}{2c_s^4} \partial_k^{(1)}(\rho u_i u_j u_k) - \frac{Q_{\alpha ij}}{c_s^4} u_i F_{\mathcal{B}j} + \frac{Q_{\alpha ij}}{c_s^2} u_i \partial_j^{(1)} \rho \right\}. \end{aligned}$$

The two last terms have been simplified by using the symmetry property of the tensor, i.e., $Q_{\alpha ij}R_{ij} = Q_{\alpha ji}R_{ji}$ for any tensor R_{ij} . The spatial partial derivative of the equilibrium reads

$$e_{\alpha i}\partial_i^{(1)}f_{\alpha}^{eq} = \omega_{\alpha} \left[e_{\alpha i}\partial_i^{(1)}\rho + \frac{e_{\alpha i}e_{\alpha j}}{c_s^2}\partial_i^{(1)}(\rho u_j) + e_{\alpha i}\frac{Q_{\alpha jk}}{2c_s^4}\partial_i^{(1)}(\rho u_j u_k) \right].$$

And if we combine the two previous equations, Eq. (2.88) becomes

$$\begin{aligned} f_{\alpha}^{(1)} = & -\frac{\tau\omega_{\alpha}}{c_s^2} \left[\rho Q_{\alpha ij}\partial_i^{(1)}u_j - e_{\alpha i}\partial_j^{(1)}(\rho u_i u_j) + \frac{Q_{\alpha ij}}{2c_s^2}e_{\alpha k}\partial_k^{(1)}(\rho u_i u_j) \right. \\ & \left. - \frac{Q_{\alpha ij}}{2c_s^2}\partial_k^{(1)}(\rho u_i u_j u_k) \right] - \frac{\delta_t\omega_{\alpha}}{2c_s^2} \left[e_{\alpha i}F_{\mathcal{B}i} + \frac{Q_{\alpha ij}}{c_s^2}u_j F_{\mathcal{B}i} \right] \end{aligned} \quad (2.91)$$

This is an important result, which highlights the fact that the non-equilibrium part of the distribution function is mainly related to the gradient of \mathbf{u} and \mathbf{u} , $\mathbf{F}_{\mathcal{B}}$ in the case of a flow subject to a body force.

To conclude, the Chapman and Enskog procedure is an asymptotic expansion in terms of powers of the Knudsen number and allows us to identify the macroscopic balance equations involved. Closed to the equilibrium at order $O(\mathcal{K})$, the Euler equations are recovered. At second-order $O(\mathcal{K}^2)$, the Navier-Stokes equations are obtained. Due to an insufficient quadrature, a small error appears in the viscous stress tensor and the lattice Boltzmann method is usually used in the case of weakly (isothermal) compressible flows. Of course, increasing the order of the quadrature is possible in order to solve thermal flows and observe phenomena beyond the Navier-Stokes level (Burnett and super-Burnett equations). The Chapman and Enskog expansion is an important tool to link the mesoscopic and macroscopic scales. In our cases, this provides a relationship between the relaxation time of the distribution function toward the equilibrium and the viscosity. Other alternative multi-scales approaches [14, 15, 16] are also possible and results in similar (compressible or incompressible) Navier-Stokes equations.

2.6 Advanced collision operators

The expression of the viscosity according to the relaxation time gives a necessary condition for the stability of the lattice Boltzmann method: $\tau \geq 1/2$ in order to have a positive viscosity. In fact, the lattice Boltzmann method is prone to numerical instabilities when τ is close to $1/2$. The BGK collision operator and the exact streaming make the LBM very little dissipative [17]. Hence, numerical errors and small pressure waves are not naturally damped causing stability issues, and simulating high Reynolds number flows challenging. Notice that the error term in the stress tensor has a negative effect by decreasing the viscous dissipation. However, this error seems to not be the major cause. In fact, a von Neumann linear analysis suggests that the instability occurs when some modes interact with each other [18]. That is why a higher-order quadrature (D2Q17) is found to be theoretically more unstable even though there is no error in the stress tensor

because the number of modes increases and consequently their possibility of interaction too. Nonetheless, the roots of the instability of the Lattice Boltzmann method are not completely understood and remain, as well as strategies to remedy these stability defects, an active research topic. In the next paragraph, we will briefly present the most common advanced collision operators used to improve the stability of the scheme.

2.6.1 Multiple relaxation time

As we learned from the Chapman and Enskog expansion, the viscous dissipation is related to the relaxation process of the second moment Π_{ij} . In the BGK collision operator, the distribution functions relax toward the equilibrium according to a single relaxation time. A more sophisticated idea is to relax each moment according to a proper relaxation time. This method is called multiple relaxation time (MRT). We introduce the matrix \mathcal{M} , which transforms the distribution functions into moments:

$$m_\alpha = \mathcal{M}f_\alpha. \quad (2.92)$$

\mathcal{M} is a square transformation matrix. If the first line of the matrix is filled only by 1, then the first moment is the density. The invert transformation from the moments to distribution functions is simply $f_\alpha = \mathcal{M}^{-1}m_\alpha$. The main idea is to perform the collision step in the moment space, namely relax each moment with individual relaxation time, transformed back the relaxed moments to the population and stream as usual. Eqs. (2.61) and (2.62) are rewritten as

$$m_\alpha^*(\mathbf{x}, t) = m_\alpha(\mathbf{x}, t) - \mathcal{S}[m_\alpha(\mathbf{x}, t) - m_\alpha^{eq}(\mathbf{x}, t)] + (\mathcal{I} - \frac{1}{2}\mathcal{S})\mathcal{M}S_\alpha \quad (2.93)$$

$$f_\alpha(\mathbf{x} + \mathbf{e}_\alpha, t + 1) = \mathcal{M}^{-1}m_\alpha^*(\mathbf{x}, t), \quad (2.94)$$

where \mathcal{I} is the identity, and \mathcal{S} is the diagonal matrix corresponding to the inverse of the relaxation time associated with each moment. Notice that the equilibrium moments are obtained from $m_\alpha^{eq} = \mathcal{M}f_\alpha^{eq}$ and the source term is also expressed in the moment space. Each line of the matrix \mathcal{M} defines a moment. To construct the transformation matrix, the only condition is the rows of the matrix should be linearly independent (\mathcal{M} has to be an invertible matrix). Hence there is no unique transformation matrix. One can choose to construct the matrix according to the Hermite polynomials however the common approach is based on a Gram-Schmidt procedure of a combination of the velocity vector \mathbf{e}_α . In both cases, the rows of \mathcal{M} are orthogonal with respect to the weight ω_α for the Hermite polynomials and with weight equal to unity for the Gram-Schmidt procedure. In the case the *D2Q9* velocity set, \mathcal{M} is usually obtained from the following nine polynomials

$$1 \quad x \quad y \quad xy \quad x^2 + y^2 \quad x^2 - y^2 \quad x(x^2 + y^2) \quad y(x^2 + y^2) \quad (x^2 + y^2)^2. \quad (2.95)$$

Let \mathcal{M}_{i-} the i -th row of \mathcal{M} and $e_{\alpha x}$, $e_{\alpha y}$ are the component of the velocity vector \mathbf{e}_α . The density, the momentum according to x and y -axes correspond respectively to $\|\mathbf{e}\|^0$

(\mathcal{M}_{1-}) , $e_{\alpha x} (\mathcal{M}_{4-})$, and $e_{\alpha y} (\mathcal{M}_{6-})$. These three vectors constitute the eigenvectors of the MRT collision operator. Then the second line \mathcal{M}_{2-} is obtained by using a Gram-Schmidt procedure on $\|e_{\alpha}\|^2$. In the same way \mathcal{M}_{5-} and \mathcal{M}_{7-} are constructed by the orthogonalization of respectively $e_{\alpha x}\|e_{\alpha}\|^2$ and $e_{\alpha y}\|e_{\alpha}\|^2$, \mathcal{M}_{8-} comes from $e_{\alpha x}^2 - e_{\alpha y}^2$ and \mathcal{M}_{9-} is built from $e_{\alpha x}e_{\alpha y}$. Finally, \mathcal{M}_{3-} is obtained from $\|e_{\alpha}\|^4$. The matrix \mathcal{M} reads [19]

$$\mathcal{M} = \begin{pmatrix} 1 & 1 & 1 & 1 & 1 & 1 & 1 & 1 & 1 \\ -4 & -1 & -1 & -1 & -1 & 2 & 2 & 2 & 2 \\ 4 & 2 & 2 & 2 & 2 & 1 & 1 & 1 & 1 \\ 0 & 1 & 0 & -1 & 0 & 1 & -1 & -1 & 1 \\ 0 & -2 & 0 & 2 & 0 & 1 & -1 & -1 & 1 \\ 0 & 0 & 1 & 0 & -1 & 1 & 1 & -1 & -1 \\ 0 & 0 & -2 & 0 & 2 & 1 & 1 & -1 & -1 \\ 0 & 1 & -1 & 1 & -1 & 0 & 0 & 0 & 0 \\ 0 & 0 & 0 & 0 & 0 & 1 & -1 & 1 & -1 \end{pmatrix}. \quad (2.96)$$

The lines of the matrix are ordered by starting with the three scalars, then the four vectors and finally the two tensors components. The vectors were multiplied by some constants in order to have some handy integer expressions. The moments are related to some macroscopic quantities. m_1 is the fluid density ρ , m_2 and m_3 are proportional to the kinetic energy and the square of the kinetic energy, respectively. m_4 and m_6 are equivalent to ρu_x and ρu_y . m_5 and m_7 are proportional to x and y-components of the heat flux. Finally, m_8 and m_9 are proportional respectively to the diagonal and off-diagonal terms of the viscous stress tensor. The diagonal of \mathcal{S} corresponds to the inverse of the relaxation time, also called relaxation rate, associated with each moment

$$\mathcal{S} = \text{diag}(0, s_E, s_{\zeta}, 0, s_q, 0, s_q, s_{\mu}, s_{\mu}) \quad (2.97)$$

Note that using the polynomials $x^2 + y^2$, $x^2 - y^2$ instead of x^2 , y^2 makes \mathcal{S} to be diagonal if one wants to decouple ζ and μ [20]. If the Chapman-Enskog expansion is applied to the lattice Boltzmann equation with the MRT collision operator, one finds

$$\mu = \left(\frac{1}{s_{\mu}} - \frac{1}{2}\right)\rho c_s^2 \quad (2.98)$$

$$\zeta = \left(\frac{1}{s_{\zeta}} - \frac{1}{2}\right)\rho c_s^2 - \frac{\mu}{3} \quad (2.99)$$

With a relaxation rate associated with each moment (some are equal to enforce isotropy), the volume viscosity can now be independently set. For high Reynolds number flows, the volume viscosity is generally artificially increased, which helps with the dissipation of pressure waves being potential sources of instability. Since the density and momentum are conserved by the collision, the value of their relaxation rate has no influence and is set to zero. s_{μ} is related to the dynamic viscosity. The other relaxation rates, s_E and s_q for $D2Q9$, do not appear in the macroscopic equations. These two free parameters can be tuned to improve the accuracy and the stability of the scheme. The BGK operator is recovered if all the relaxation rates are the same.

There is no systematic procedure to choose the relaxation rates that do not appear in the macroscopic equations. It is often a compromise between accuracy and stability. Notice that the application of the MRT collision operator for three-dimensional flows ($D3Q15$, $D3Q19$, and $D3Q27$) is straightforward [21] and there are more free parameters, relaxation rates, to adjust. We will now discuss on reduced MRT model with only two relaxation time (TRT), one related to the dynamics viscosity corresponding to the moments constructed with the even-order velocity polynomials ($s_E = s_\zeta = s_\mu = s_+$) and the other one is a free parameter corresponding to the moments constructed with the odd-order velocity polynomials ($s_q = s_-$). In addition to providing a simple and a fast way to choose the relaxations rates, the accuracy error becomes independent of the viscosity if the so-called magic number Λ remains constant [22]

$$\Lambda_{+-} = \left(\frac{1}{s_+} - \frac{1}{2} \right) \left(\frac{1}{s_-} - \frac{1}{2} \right). \quad (2.100)$$

The specific choice of $\Lambda = 3/16$ corresponds to $s_q = 8 \frac{2-s_+}{8-s_+}$. In the case of a Poiseuille flow in a straight channel, the boundary implemented with the bounce-back condition (explanations are given later at section 2.7.3) is located exactly in the middle between a fluid node and a solid (wall) node. As a general rule, $\Lambda \in [1/8, 3/8]$ allows reasonably accurate results for flows in porous media [23, 24].

2.6.2 Central moments

The central moment method is an extension of the MRT collision model. As we previously mentioned, in MRT the transformation matrix is not unique. In the central moment collision operator, \mathcal{M} is constructed using polynomials in $(\mathbf{e}_\alpha - \mathbf{u})$ instead of \mathbf{e}_α . This enhances the Galilean invariance and stability. However the matrix \mathcal{M} has to be inverted at each time step, in each grid point since the matrix is no longer constant and depends on the velocity of the fluid. This greatly increases the computational cost of the algorithm. Two different algorithms can be found in the literature. The cascaded operator refers to the use of an orthogonal basis for the construction of the transformation matrix, and the moments relax to the continuous Maxwellian equilibrium. Otherwise, central moments are generally based on a non-orthogonal basis and relax to the standard discrete equilibrium. Since the choice of the polynomials sometimes differ and result in different transformation matrices, the comparison between models is complicated. Extensive details are available in Ref. [25] and recent advances in Ref. [26].

2.6.3 Cumulant

The cumulant collision operator follows the same main principle of relaxing some quantities, cumulants instead of moments of the distribution functions. The cumulants can be computed from a non-linear combination of central moments. This results in a better Galilean invariance and more stable results [27] but the scheme becomes complicated and especially more computationally intensive than the central moments collision operator.

2.6.4 Regularized

The regularized collision operator is based on a simple idea that the instabilities stem from the high order terms in the Chapman-Enskog expansion. At each iteration, before collision, the distribution function is regularized as follow [28]

$$f_\alpha^{reg} = f_\alpha^{eq} + f_\alpha^{(1)} \quad (2.101)$$

Thus the distribution function does not contain any unnecessary high order terms at the Navier-Stokes level which may worsen the stability of the scheme. From the Chapman and Enskog expansion Eq. (2.91), one finds

$$f_\alpha^{(1)} \approx -\frac{\omega_\alpha}{2c_s^2} \left[\tau \rho Q_{\alpha ij} \left(\frac{\partial u_i}{\partial x_j} + \frac{\partial u_j}{\partial x_i} \right) - \tau \frac{Q_{\alpha ij}}{c_s^2} \frac{\partial}{\partial x_k} (\rho u_i u_j u_k) \right] - \frac{\delta_t}{2} S_\alpha. \quad (2.102)$$

Notice that we could use directly Eq. (2.91) and evaluate the derivatives by finite difference however the regularized collision operator would not be local anymore and thus becomes computationally very expensive. We recall Eq. (2.82)

$$\Pi_{ij}^{neq} \approx \Pi_{ij}^{(1)} = -\tau \left[\rho c_s^2 (\partial_j^{(1)} u_i + \partial_i^{(1)} u_j) - \partial_k^{(1)} (\rho u_i u_j u_k) \right] - \frac{\delta_t}{2} (u_i F_{Bj} + u_j F_{Bi}) \quad (2.103)$$

with $\Pi_{ij}^{neq} = \sum_\alpha e_{\alpha i} e_{\alpha j} (f_\alpha - f_\alpha^{eq})$. Using the two previous equations and Eq. (2.90) gives

$$f_\alpha^{(1)} \approx \frac{\omega_\alpha}{2c_s^4} Q_{\alpha ij} \Pi_{ij}^{neq} - \frac{\delta_t \omega_\alpha}{2c_s^2} e_{\alpha i} F_{Bi} \quad (2.104)$$

Therefore, $f_\alpha^{(1)}$ can be approximated locally, and the collision step is performed with the regularized distribution functions, then the post-collision distribution functions are propagated and so forth. The method is later improved in Ref. [29] where an exact Hermite polynomials formulation of the previous equation is found up to any arbitrary order. Further details on the effect of the regularized operator based on linear stability analysis can be found in Ref. [30].

2.6.5 Entropic

The entropic collision operator is based on the \mathcal{H} -theorem. Boltzmann introduced the quantity

$$\mathcal{H} = \int f \ln(f) d\mathbf{c}, \quad (2.105)$$

and showed that \mathcal{H} can only decrease (similar to the second law of thermodynamic where entropy can only increase in time) and reaches a minimum when the gas is in equilibrium state. The discrete \mathcal{H} -function has the following formulation:

$$\mathcal{H} = \sum_\alpha f_\alpha \ln \left(\frac{f_\alpha}{\omega_\alpha} \right). \quad (2.106)$$

The lattice Boltzmann equation without forces in entropic models is given by [31]

$$f_\alpha(\mathbf{x} + \mathbf{e}_\alpha, t + 1) = f_\alpha(\mathbf{x}, t) + \iota\xi [f_\alpha^{eq}(\mathbf{x}, t) - f_\alpha(\mathbf{x}, t)], \quad (2.107)$$

where $\xi \in [0, 1]$ is related to the viscosity and ι is the positive root of

$$\mathcal{H}(f_\alpha + \iota(f_\alpha^{eq} - f_\alpha)) = \mathcal{H}(f_\alpha). \quad (2.108)$$

The entropy of the post-collision state $f_\alpha + \iota(f_\alpha^{eq} - f_\alpha)$ should be equal to the pre-collision state f_α whereas the appropriate dissipation is due to the viscosity ($\xi \leq 1$). Notice that if $\iota = 2$ the standard BGK collision operator is recovered. The instability of the scheme could be explain by the non-respect of the \mathcal{H} -theorem. Thus ι is obtained by solving the previous equation with a Newton-Raphson algorithm or approximating with an analytical asymptotic expression. Several formulations of equilibrium can be found in the literature. The standard polynomial is sometimes employed. In others articles the equilibrium is the solution of the minimization problem Eq. (2.106) under the constraints $\rho = \sum_\alpha f_\alpha^{eq}$ and $\rho\mathbf{u} = \sum_\alpha \mathbf{e}_\alpha f_\alpha^{eq}$.

We highlight that the entropic model is very different from the other mentioned collision operators. Indeed in the entropic collision operator, the effective viscosity is dynamically adjusted in order to enhance the stability. This is somewhat equivalent to the use of a sub-grid scale model.

So, different possibilities exist so as to enhance the stability of the lattice Boltzmann scheme. A comprehensive theoretical comparison is available in Ref. [20]. We will use the MRT collision operator because the computational cost is less than the central moment, cumulant, and entropic. The application of the MRT is straightforward for any discrete and non-standard formulation of the collision through the direct multiplication of the transformation matrix. In addition, the error becomes viscosity independent if equivalent rules as in the TRT are used. Although the regularized collision operator has the lowest computational cost, the two last properties are tricky. In addition, the MRT collision operator can also be extended to central moment with minimal modifications in case of strong instability issues.

2.7 Boundary conditions

In order to simulate a physical system and solve partial differential equations, one needs to provide appropriate initial and boundary conditions. This topic should not be overlooked since an error in the boundary condition will degrade the solution everywhere. The main difficulty concerning the boundary conditions in the lattice Boltzmann method is that we need to prescribe the boundary conditions at the mesoscopic level, whereas the boundary condition are generally formulated according to macroscopic quantities. In addition, if computing the moment from the distribution functions is simple, the inverse is not unique because there are usually more distribution functions than moments to be prescribed. From author's experience, the treatment of the boundary conditions is one of the main sources of instability. Various formulations of the boundary conditions

exist in the lattice Boltzmann method. We will present simple boundary conditions that have been used. We distinguish two types of nodes, the fluid nodes where normal LBM algorithm applies and boundary nodes where some distribution functions are unknown after the streaming step and have to be defined.

2.7.1 Periodic

Periodic boundary conditions are the most simple and mimic a bigger periodic domain by duplicating in the relevant direction the current domain. The incoming distribution functions from the boundary nodes are replaced by the outgoing distribution functions from the opposite boundary nodes as shown by the sketch in Fig. 2.3 .

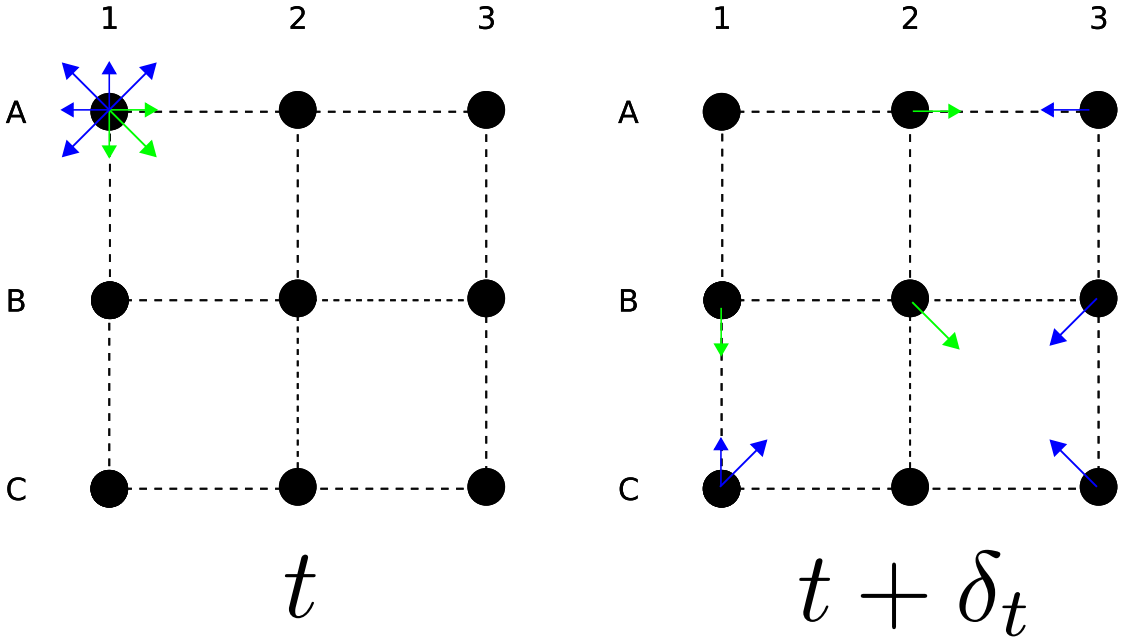


Figure 2.3 – Fully periodic two-dimensional domain. Only the distribution functions from the node A1 are drawn. Green distribution functions stream as usual. Periodic boundary condition implies to the blue distribution functions.

2.7.2 Equilibrium

In the equilibrium boundary condition, all the post-streaming distribution function of a boundary node are set be equal to the equilibrium according to the prescribed density and momentum:

$$f_{\alpha}(\mathbf{x}_b, t) = f_{\alpha}^{eq}(\rho_w, \mathbf{u}_w). \quad (2.109)$$

where \mathbf{x}_b is the location of the boundary node where ρ_w and \mathbf{u}_w are enforced. In spite of being simple, this boundary condition is only exact when the relaxation time is equal to one or when the non-equilibrium part of the distribution functions is null. The latter

case has no practical interest since it corresponds to a spatially uniform solution. The previous condition can be improved by using the first order perturbation

$$f_\alpha(\mathbf{x}_b, t) = f_\alpha^{eq}(\rho_w, \mathbf{u}_w) + f_\alpha^{(1)}, \quad (2.110)$$

and $f_\alpha^{(1)}$ is given by Eq. (2.91). The boundary solution has been enriched with velocity gradients, which are generally calculated from finite differences. Notice that this condition is unable to reproduce an exact parabolic solution but only solutions with a constant velocity gradient can be obtained.

The initialization of the simulation follows the same strategy. The distribution functions are set to equilibrium and higher orders if needed according to the initial hydrodynamic quantities. In general, we are looking for the long time behavior of the flow. In this case, an exact initialization of the flow is not mandatory. First a transient nonphysical regime will decay and after some time, the system will progress to the appropriate physical state.

2.7.3 Bounce-back

The bounce-back is the most widely used boundary condition for simulating a non-slip velocity boundary. Its astonishing simplicity explains its popularity. For a resting wall, the distribution function that hits the wall (during the streaming step) is reflected back in the opposite direction as depicted in Fig. 2.4. The missing distribution functions are obtained from

$$f_{\bar{\alpha}}(\mathbf{x}_b, t) = f_\alpha(\mathbf{x}_b, t) \quad \text{with} \quad \mathbf{e}_{\bar{\alpha}} = -\mathbf{e}_\alpha. \quad (2.111)$$

Note that if the distribution functions are specularly reflected then the free-slip boundary is obtained.

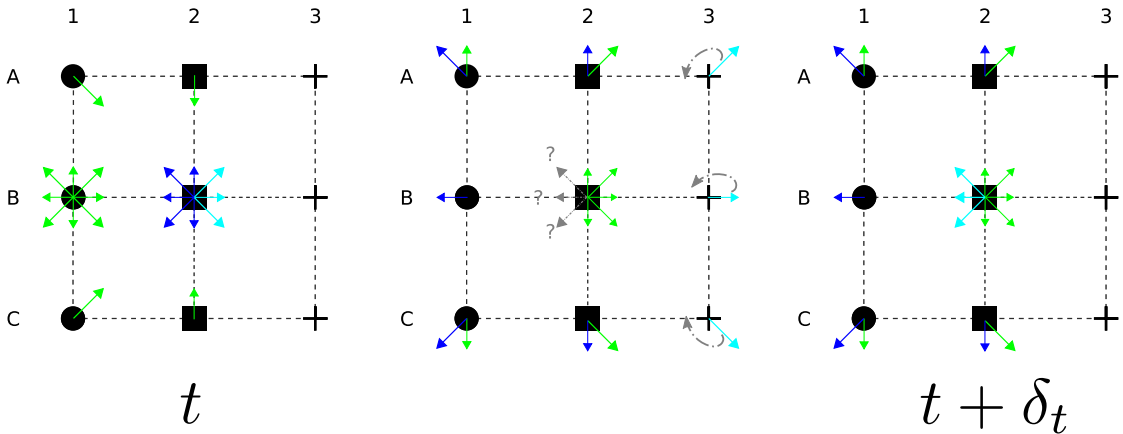


Figure 2.4 – Streaming and bounce-back condition. The nodes are divided into three types: ● fluid nodes, ■ boundary nodes, + solid nodes. Focusing on node B2, some distribution functions (in grey) are unknown after the standard streaming step. They are given by the distribution functions which are reflected back from the solid nodes.

The physical position of the interface between solid and fluid nodes is halfway between the boundary and solid nodes. In addition the bounce-back conserves the mass exactly and is straightforward to apply in three dimensions for any velocity sets. There are two main drawbacks. The boundary is approximated via a stair-case description. The exact location of the boundary depends on the viscosity. This non-physical behavior can be cured using the MRT or TRT collision operators which have more degrees of freedom, i.e., relaxation rates.

2.7.4 Non-equilibrium bounce-back

As its name suggested, the bounce-back condition is applied on the non-equilibrium part of the missing distribution functions. This boundary condition is also called Zou and He from its authors' name [32]. For instance, if we consider the left side of a two-dimensional domain. f_2 , f_6 , and f_9 are missing. This yields

$$\left. \begin{aligned} f_2^{neq} &= f_4^{neq} + N_x \\ f_6^{neq} &= f_8^{neq} + N_x + N_y \\ f_9^{neq} &= f_7^{neq} + N_x - N_y \end{aligned} \right\} \implies \begin{aligned} f_2 &= f_4 + 2\rho_w u_{wx}/3 + N_x \\ f_6 &= f_8 + \rho(u_{wx} + u_{wy})/6 + N_x + N_y \\ f_9 &= f_7 + \rho(u_{wx} - u_{wy})/6 + N_x - N_y \end{aligned} \quad (2.112)$$

where N_x , N_y are correction terms. Using the definition of the momentum, the corrections are calculated as

$$\rho u_{wx} = f_2 - f_4 + f_6 - f_8 + f_9 - f_7 + \frac{1}{2}F_{\mathcal{B}x} \implies N_x = -\frac{1}{6}F_{\mathcal{B}x}, \quad (2.113)$$

$$\rho u_{wy} = f_3 - f_5 + f_6 - f_8 + f_7 - f_9 + \frac{1}{2}F_{\mathcal{B}y} \implies N_y = -\frac{1}{2}(f_3 - f_5) + \frac{1}{3}\rho_w u_{wy} - \frac{1}{4}F_{\mathcal{B}y}. \quad (2.114)$$

The final expressions for the missing distribution functions at the left boundary read

$$f_2 = f_4 + \frac{2}{3}\rho_w u_{wx} - \frac{1}{6}F_{\mathcal{B}x}, \quad (2.115)$$

$$f_6 = f_8 - \frac{1}{2}(f_3 - f_5) + \frac{1}{6}\rho_w u_{wx} + \frac{1}{2}\rho_w u_{wy} - \frac{1}{6}F_{\mathcal{B}x} - \frac{1}{4}F_{\mathcal{B}y}, \quad (2.116)$$

$$f_9 = f_7 + \frac{1}{2}(f_3 - f_5) + \frac{1}{6}\rho_w u_{wx} - \frac{1}{2}\rho_w u_{wy} - \frac{1}{6}F_{\mathcal{B}x} + \frac{1}{4}F_{\mathcal{B}y}. \quad (2.117)$$

The non-equilibrium bounce back boundary condition can only enforce either the density or the velocity otherwise the system will be over-constrained. Contrary to the equilibrium boundary condition, this non-equilibrium bounce-back is able to enforce exactly a parabolic profile. The resulting density (respectively velocity) is computed from the known distribution functions and the desired velocity (respectively density):

$$\rho_w - \rho_w u_{wx} = f_1 + 2(f_7 + f_4 + f_8) - \frac{1}{2}F_{\mathcal{B}x} \quad (2.118)$$

Similarly, if we apply the non-equilibrium bounce-back to the right boundary of the domain, we find

$$f_4 = f_2 - \frac{2}{3}\rho_w u_{wx} + \frac{1}{6}F_{\mathcal{B}x}, \quad (2.119)$$

$$f_7 = f_9 - \frac{1}{2}(f_3 - f_5) - \frac{1}{6}\rho_w u_{wx} + \frac{1}{2}\rho_w u_{wy} + \frac{1}{6}F_{\mathcal{B}x} - \frac{1}{4}F_{\mathcal{B}y}, \quad (2.120)$$

$$f_8 = f_6 + \frac{1}{2}(f_3 - f_5) - \frac{1}{6}\rho_w u_{wx} - \frac{1}{2}\rho_w u_{wy} + \frac{1}{6}F_{\mathcal{B}x} + \frac{1}{4}F_{\mathcal{B}y}. \quad (2.121)$$

2.7.5 Open boundary

In some problems, both density and velocity at the boundary are unknown. When the area of interest is far from the boundary, a simple first order interpolation of the missing (post-streaming) distribution functions is enough. For the right boundary of a two dimensional domain, we have

$$f_7(x_b, y_b, t) = f_7(x_b - 1, y_b, t) \quad (2.122)$$

$$f_4(x_b, y_b, t) = f_4(x_b - 1, y_b, t) \quad (2.123)$$

$$f_8(x_b, y_b, t) = f_8(x_b - 1, y_b, t) \quad (2.124)$$

This brief overview of the boundary conditions describes simple boundary conditions for different cases: periodic, prescribed density and velocity, no-slip, prescribed density or velocity, and a null gradient for the distribution functions. There are plenty more formulations for the boundary conditions in LBM. Especially, the previous boundary conditions are expressed for straight walls. Boundary conditions for curved walls are possible but often degrade the accuracy of the solution while being the only way to go beyond "lego-land".

2.8 Synthesis

In the previous section, we attempted to cover the basics of the lattice Boltzmann method. From the continuum Boltzmann equation, we discretize the velocity space by means of truncation of Hermite series and Gauss-Hermite quadratures. The choice of a small velocity set (truncation order) limits the application to isothermal flows. Then, we use the method of characteristics, a trapezoidal integration rule, and a suitable change of variable to obtain an explicit discrete equation in time and physical space. This results in a strong coupling between the kinetic velocities, the space and time steps. The equation is solved on a lattice and may be divided into two sub-steps: collision and streaming. According to the deviation from the equilibrium, the Chapman-Enskog expansion procedure predicts the macroscopic behavior of the lattice Boltzmann equation. Thus if the Knudsen number is small enough, we recover the Navier-Stokes equation and obtain a significant the relationship between the relaxation time of the BGK collision operator and the macroscopic viscosity. We also address more advanced

collision operators in order to remedy some stability defects of the BGK collision operator and the formulation of boundary conditions in LBM. This rather complete overview, but far from being exhaustive, only considers a single fluid. The main objective is now to extend the lattice Boltzmann method to multiple species.

Chapter 3

Mixture of gases

In this section, we first present a general approach of diffusion of gases by means of the Maxwell-Stefan equations. We show the particularity of the mixture of three and more species and the so-called multi-component effects especially regarding the intuitive but unfortunately inadequate Fick's law.

3.1 Multi-component diffusion theory

The diffusion of multiple components in fluids (gases or liquids) has been extensively studied in chemical engineering. The diffusion theory can be obtained from different ways. It is usually derived from the irreversible thermodynamics starting with the entropy balance see for instance Ref. [33]. In the other hand, the diffusion theory can also be derived rigorously from statistical mechanics and especially the kinetic theory of gases (and liquids) and the Chapman-Enskog expansion [1, 34] (see also Appendix D and E of Ref. [35] for a simpler introduction). Another approach called "theory of mixtures" is based on the description of balance equations for each species [36]. All these routes are rather complementary and lead to the Maxwell-Stefan equations when pure diffusion is considered. We will present how these latter equations could be obtained from simple considerations following the approach of Ref. [37].

Let consider the diffusion of two gases at ambient pressure and temperature, each contained in bulbs that are joined by a capillary tube. The diameter of tube is large enough to assume the gases behave as continuum media. Each gas moves through each other with a local velocity \mathbf{u}_1 (respectively \mathbf{u}_2) for the gas contained in the first (respectively second) bulb. The difference between velocities causes a friction force. We focus on a small volume of the mixture in the capillary tube as depicted in Fig.3.1. In this small volume, the friction force depends on the velocity differences and the number of possible interactions, collisions, between the molecules of the two gases, which is proportional to x_1x_2 where x_m is the molar fraction of the m -th gas. In order to avoid confusion the subscript i, j, k are used to represent spatial coordinates whereas m, n are related to the mixture components.

The net force acting on the molecules of the first gas is the partial pressure $p_1 = x_1p$

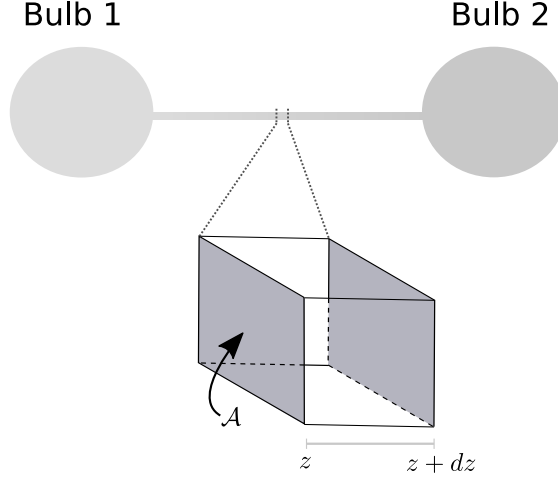


Figure 3.1 – Diffusion of two gases and a small control volume between z and $z + dz$ where \mathcal{A} is the area normal to diffusion.

multiplied by the area \mathcal{A} . We can write the net force acting on molecules of gas 1 per unit of volume in the z -direction as

$$\lim_{dz \rightarrow 0} \frac{\mathcal{A}p_1|_z - \mathcal{A}p_1|_{z+dz}}{\mathcal{A}dz} = -\frac{dp_1}{dz},$$

and adding the contribution from the other spatial direction gives ∇p_1 . So the net force acting on a molecule of the first gas per unit of volume is proportional to

$$\nabla p_1 \propto (x_1 x_2, \mathbf{u}_1 - \mathbf{u}_2), \quad (3.1)$$

$$\nabla p_1 = -\mathcal{F}_{12} x_1 x_2 (\mathbf{u}_1 - \mathbf{u}_2). \quad (3.2)$$

p_1 is the force per unit of volume trying to move the molecules of the first gas at relative velocities $(\mathbf{u}_1 - \mathbf{u}_2)$ with a concentration weight factor $x_1 x_2$ and a friction coefficient \mathcal{F}_{12} . The diffusion coefficient is introduced as $\mathcal{D}_{12} = p/\mathcal{F}_{12}$ and has a dimension of square meter per second. In chemical engineering the term driving force is often employed for $\mathbf{d}_m = (1/p)\nabla p_m = \nabla x_m$ despite not being a real mechanical force. We have for both gases

$$\mathbf{d}_1 = \nabla x_1 = -\frac{x_1 x_2 (\mathbf{u}_1 - \mathbf{u}_2)}{\mathcal{D}_{12}}, \quad (3.3)$$

$$\mathbf{d}_2 = \nabla x_2 = -\frac{x_1 x_2 (\mathbf{u}_2 - \mathbf{u}_1)}{\mathcal{D}_{21}}. \quad (3.4)$$

Since $\nabla x_1 + \nabla x_2 = \mathbf{0}$, the diffusion coefficient is symmetric $\mathcal{D}_{12} = \mathcal{D}_{21}$.

Expression for mixture of N gases can be obtained by considering the summation of

friction forces for each pair of gases [37]:

$$\mathbf{d}_m = \nabla x_m = - \sum_{n=1}^N \frac{x_m x_n (\mathbf{u}_m - \mathbf{u}_n)}{\mathcal{D}_{mn}} \quad \text{for } m = 1, \dots, N \quad (3.5)$$

$$= - \sum_{n=1}^N \frac{1}{c_t \mathcal{D}_{mn}} (x_n \mathbf{J}_m - x_m \mathbf{J}_n) \quad \text{for } m = 1, \dots, N. \quad (3.6)$$

The last equation is a more conventional formulation used in chemical engineering where the molar fluxes are given by $\mathbf{J}_m = c_m \mathbf{u}_m$ with c_m , the molar concentration of the component m and c_t , the total molar concentration of the mixture. Equations (3.5) or (3.6) are referred as the Maxwell-Stefan equations. These have been initially suggested by Maxwell more than one hundred fifty years ago for binary mixtures of gases using preliminaries of kinetic theory [38] and generalized by Stefan [39] for mixture of gases. Later these equations have been rigorously derived for ideal gases by means of kinetic theory [1, 34]. The binary or Maxwell-Stefan diffusion coefficients \mathcal{D}_{mn} are positive symmetric and do not depend on the composition of the mixture but on the temperature, pressure, and the molecular properties of the considered pair of gases. They can be calculated by means of molecular theories or from experimental data. The Maxwell-Stefan equations are still valid for non-ideal mixtures, dense gases, liquids, and polymers but the driving force, is replaced by the gradient of the chemical potential [37]:

$$\mathbf{d}_m = \frac{x_m}{RT} \nabla|_{p,T} \mu_m^{CH} \quad (3.7)$$

$$= \sum_{n=1}^{N-1} \Gamma_{mn} \nabla x_n, \quad \Gamma_{mn} = \delta_{mn} + x_m \frac{\partial \ln \gamma_m}{\partial x_n} \Big|_{p,T, x_p \neq n, x_p=1, \dots, N-1} \quad (3.8)$$

where μ_m^{CH} is the chemical potential of the species m , γ_m is the coefficient of activity, and Γ_{mn} is the thermodynamic correction factor, which is equal to one for ideal mixtures. For highly non-ideal mixtures, the thermodynamic correction factors strongly depends on the mixture composition [37, 40].

3.2 Limitations of Fick's law

In the case of a binary mixture, the molar flux from Eq. 3.6 can be rewritten as

$$\mathbf{J}_1 = -c_t \mathcal{D}_{12} \nabla x_1 = -c_t \mathcal{D}_{12} \mathbf{d}_1, \quad (3.9)$$

and the Maxwell-Stefan equations reduce to Fick's law. This formulation seems easier to manipulate and gives a direct relationship between the molar fluxes and the gradient of the molar fraction, nonetheless its application to three and more components has severe flaws and could lead to some misconceptions of mass transfer. To highlight the fact that the formulation of the Fick's law may be inadequate to simulate multi-component flows, we focus on the diffusion of three gases. Let consider the following experimental apparatus composed of two equal bulbs filled with different mixtures of gases and joined

by a small capillarity tube (similar as Fig.3.1). The initial composition of nitrogen, hydrogen, and carbon dioxide are stated in Table 3.1. This experiment has been proposed in Ref. [41] and the results are shown in Fig.3.2.

left bulb (1)	right bulb (2)	Does N_2 transfer	}	from left to right?
$x_{N_2} = 0.46$	$x_{N_2} = 0.52$			from right to left?
$x_{H_2} = 0.54$	$x_{H_2} = 0$			not at all?
$x_{CO_2} = 0$	$x_{CO_2} = 0.48$			all the three above?

Table 3.1 – Initial composition of a "simple" diffusion of three gases and a question.

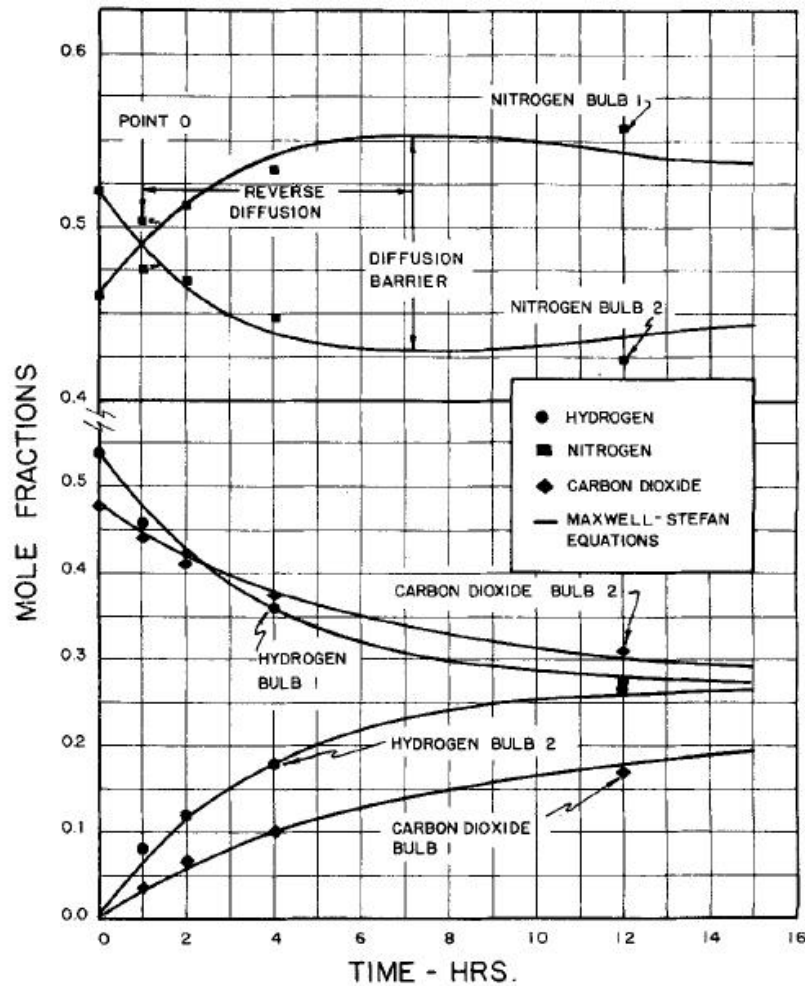


Figure 3.2 – Time evolution of the mixture in each bulb. Experimental data from Ref. [41], with permission.

As expected, the hydrogen and carbon dioxide diffuse in the opposite direction of their concentration gradient but the nitrogen exhibits a non-standard behavior. First the nitrogen diffuses from the high concentration to the low concentration (from left to right). After approximately one hour, the concentration of nitrogen in both bulbs becomes equal but the nitrogen continues to diffuse in the same direction, against its own concentration gradient. After seven hours, the concentration of N_2 reaches a plateau and does not evolve even in the presence of a fairly large concentration gradient. These non-standard phenomena are identified as osmotic diffusion, reverse diffusion, and diffusion barrier. They are depicted in Fig. 3.3 and are specific to the mixing of three and more components. Finally, the concentration in both bulbs slowly tends towards the same value.

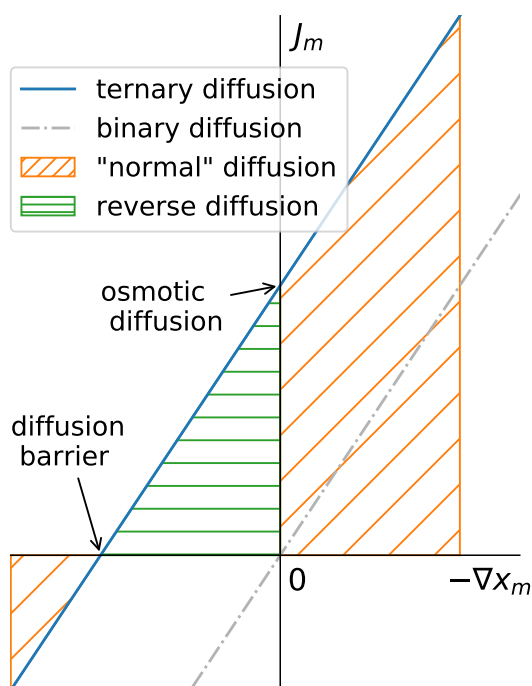


Figure 3.3 – Sketch of possible multi-component diffusion effects and their definition.

As shown in Fig.3.2, the evolution of the mixture composition in each bulb is well predicted by the Maxwell-Stefan equations but the tentative to explain it with conventional Fick's law Eq. (3.9) fails. The first remark is that contrary to the binary case where the driving forces have to be equal in magnitude but opposite in sign $\nabla x_1 = -\nabla x_2$, no such requirement exists in a ternary mixture where only the summation of the driving forces has to be zero. Thus we can expect a different dynamic compared to binary mixtures. Forgetting about Fick's law, it is easy to physically interpret what is happening. The hydrogen diffuses to the other bulb because there is far more hydrogen in the left bulb than in the right bulb, indeed the random thermal motions will on average cause the

hydrogen to move to the less populated bulb. Carbon dioxide is also subject to the same mechanism. On the contrary, at some points, the nitrogen seems to be dragged by the carbon dioxide. There is actually more friction between the heavy molecules of carbon dioxide and nitrogen than between the light molecules of hydrogen and nitrogen. In consequence, the diffusion of nitrogen is at some point governed by the concentration gradients of hydrogen and carbon dioxide, rather than its own concentration gradient, which is relatively small. Note that using a different initial mixture composition, the reverse diffusion phenomena could also occur with the carbon dioxide instead of nitrogen.

It is still possible to obtain a Fick-like expression for the fluxes by means of a matrix formulation. First, we remark that there are $N - 1$ independent fluxes since $\sum_{m=1}^N \mathbf{J}_m = \mathbf{0}$. Eq. 3.6 can be recast to a $N - 1$ dimensional matrix problem

$$c_t \mathbf{d}_m = -B_{mm} \mathbf{J}_m - \sum_{n \neq m, n=1}^{N-1} B_{mn} \mathbf{J}_n, \quad (3.10)$$

where $[B_{mn}]$ is a $N - 1$ square matrix, with diagonal terms $B_{mm} = x_m / \mathcal{D}_{mN} + \sum_{n \neq m, n=1}^N x_n / \mathcal{D}_{mn}$ and off-diagonal terms $B_{mn} = -x_m (1 / \mathcal{D}_{mn} - 1 / \mathcal{D}_{mN})$. Its inverted form gives the generalized Fick's law:

$$\begin{pmatrix} \mathbf{J}_1 \\ \vdots \\ \mathbf{J}_{N-1} \end{pmatrix} = -c_t [B_{mn}]^{-1} \begin{pmatrix} \mathbf{d}_1 \\ \vdots \\ \mathbf{d}_{N-1} \end{pmatrix}. \quad (3.11)$$

Let $[B_{mn}]^{-1} = [D_{mn}]$. For an ideal ternary mixture this reduces to

$$\mathbf{J}_1 = -c_t D_{11} \nabla x_1 - c_t D_{12} \nabla x_2, \quad (3.12)$$

$$\mathbf{J}_2 = -c_t D_{21} \nabla x_1 - c_t D_{22} \nabla x_2, \quad (3.13)$$

$$\text{and } \mathbf{J}_3 = -\mathbf{J}_1 - \mathbf{J}_2. \quad (3.14)$$

where D_{mn} is a multi-component Fick diffusion coefficients:

$$D_{11} = \mathcal{D}_{13} (x_1 \mathcal{D}_{23} + (1 - x_1) \mathcal{D}_{12}) / \hat{D}, \quad (3.15)$$

$$D_{12} = x_1 \mathcal{D}_{23} (\mathcal{D}_{13} - \mathcal{D}_{12}) / \hat{D}, \quad (3.16)$$

$$D_{21} = x_2 \mathcal{D}_{13} (\mathcal{D}_{23} - \mathcal{D}_{12}) / \hat{D}, \quad (3.17)$$

$$D_{22} = \mathcal{D}_{23} (x_2 \mathcal{D}_{13} + (1 - x_2) \mathcal{D}_{12}) / \hat{D}, \quad (3.18)$$

$$\text{with } \hat{D} = x_1 \mathcal{D}_{23} + x_2 \mathcal{D}_{13} + x_3 \mathcal{D}_{23}. \quad (3.19)$$

We note that that the cross-coefficients D_{mn} are responsible for the multi-component effects. These are significant when $|D_{mn} \nabla x_n| \geq |D_{mm} \nabla x_m|$.

The multi-component Fick diffusion coefficient D should not be confused with the Maxwell-Stefan (also called binary) diffusion coefficients \mathcal{D} . For a mixture of two species, both coefficients are equivalent. For three components and more, a Fick-like formulation is still possible but it is often inadequate because the Fick diffusion coefficients are not

as practical as the Maxwell-Stefan diffusion coefficients. First, four Fick diffusion coefficients are needed to describe a ternary mixture. These coefficients may be positive or negative, are usually non-symmetric, and vary according to the mixture composition. In addition, D_{mn} has less physical meanings in that it does not reflect the $m-n$ interactions and their numerical values depend on the particular choice of component numbering. Finally, the multi-component Fick diffusion coefficients have to be manipulated with great care since they depend on the choice of the associated fluxes. For instance, we can define four generalized Fick's laws in matrix form with commonly used fluxes where the uppercase \mathbf{J} denotes the molar fluxes and the lowercase \mathbf{j} stands for the mass fluxes:

$$(\mathbf{J}_m) = -c_t [D_{mn}] (\nabla x_m) \text{ with respect to the molar fraction,} \quad (3.20)$$

$$(\mathbf{j}_m) = -\rho_t [D_{mn}^y] (\nabla y_m) \text{ with respect to the mass fraction,} \quad (3.21)$$

$$(\mathbf{J}_m^c) = -[D_{mn}^c] (\nabla c_m) \text{ with respect to the molar concentration,} \quad (3.22)$$

$$(\mathbf{j}_m^\rho) = -[D_{mn}^\rho] (\nabla \rho_m) \text{ with respect to the density.} \quad (3.23)$$

All the four square $N - 1$ dimensional matrices of Fick diffusion coefficients above are generally different and the transformation from one to another is not trivial. The use of the species density or species molar concentration for the driving force is usually not recommended since they are not convenient variables [37].

To conclude, the multi-component Fick formulation is not as adequate as the Maxwell-Stefan approach which is based on the notion of friction forces. In fact, the difference is much more profound in some way similar to the chicken and the egg dilemma, in the sense that the Maxwell-Stefan formulation assumes that fluxes (velocities) difference results in driving forces, and in the other hand the generalized Fick formulation deduces the fluxes from the driving forces with the flaws we underlined. Only pure diffusion was considered here without any thermal (Soret) diffusion, external forces, convection, and viscous effects. We will show that in the lattice Boltzmann method the collision is in general modified to take into account the interactions between multiple species similar to the Maxwell-Stefan approach.

Part II

LBM for miscible gases: a forcing term approach

4	Lattice Boltzmann models for mixtures	57
5	A simplified kinetic model for multi-component mixtures	61
5.1	Lattice Boltzmann algorithm	61
5.2	Species with different molecular masses	63
6	Macroscopic limit	65
6.1	Macroscopic equations	65
6.2	Some variations on the equation formulation	65
6.3	Limit expressions	67
6.4	Transport coefficients	71
7	Numerical simulations	73
7.1	A- Decay of a density wave	73
7.2	B- Equimolar counter-diffusion	76
7.3	C- Loschmidt's tube	77
7.4	D- Opposed jets flow	80
8	Synthesis	83

Chapter 4

Lattice Boltzmann models for mixtures

In the simplest case of the mixing not affecting the flow dynamics, as is the case of the mixing of a dye or a tracing species, the Navier-Stokes or the lattice Boltzmann equations are solved to describe the flow dynamics, while the dye or species concentrations are modeled separately by simple convection-diffusion equations (passive scalar approach). However, mixing is often much more complex. The flow dynamics and the mixing process are heavily coupled and cannot be separated since mixing produces changes to the fluid. Mixing dynamics are then incredibly complicated as the interactions between various species need to be accounted for (e.g., collisions in the kinetic formulation). Whereas a large number of studies about global mixing dynamics are available, a good understanding of the microscopical processes involved in complex chemical mixing is still lacking.

The classical approach for the simulation of mixtures is based on the single-fluid approach that assumes as unknowns the species densities and the mixture velocity. The Navier-Stokes equations are solved for the mixture using phenomenological laws such as Fick's law or the Maxwell-Stefan equations for the species mass fluxes. This approach is often used in combustion with detailed chemistry, which involves a large number of species (see Ref. [42] for a lattice Boltzmann single-fluid model).

However, the use of a mixture velocity as a unique unknown can lead to some errors in the description of the flow dynamics. This is particularly true when the chemical properties of each species differ greatly and in situations where the mixing process depends on the chemical composition and the velocities of each species. For instance, consider the case of two different coflowing gases separated by a splitter plate. On either side of the plate, the dynamics is governed by Navier-Stokes equations and a velocity is defined for each gas. Past the splitter plate, the two gases start mixing. In the case of the single-fluid approach, only one velocity is specified for the mixture, which may be defined in terms of either a mass, molar, volume, or any other averages. Instead, in order to accurately depict the transient mixing dynamics, a more natural way is to consider the species densities and the velocities of each species as unknowns (as prior to mixing).

This is the so-called multi-fluid approach, which is comparable to the Maxwell-Stefan approach to mass transfer.

The LBM provides an alternative and convenient way to model fluid flows compared to conventional macroscopic approaches [4]. Indeed, the algorithm is simple, computationally efficient due to its explicit formulation and is easily adapted for parallel computing. The LBM is therefore particularly appealing for the simulation of miscible mixtures. In the multi-fluid strategy, one introduces a distribution function for each species. In single species flows, the collision of particles is approximated by the Bhatnagar-Gross-Krook (BGK) collision operator [3] and the distributions relax to equilibrium values at a rate that depends on the relaxation time. In the case of a mixture, there is no unique BGK formulation. Hence, different LBMs for multi-component flows have been developed depending on the underlying kinetic theory of the mixture being investigated. One possible approach is to split collisions between molecules of the same species (self-collision) and collisions between molecules of different species (cross-collision). Luo and Girimaji [43] employ a linear collision based on Sirovich's kinetic theory of mixtures [44]. This work is further extended from binary to multi-component flows in Refs. [45, 46]. In his early work, Asinari [47, 48] uses a model derived from Hamel's kinetic theory [49]. Other noticeable split collision models can be found in [50] and [51]. The latter authors exploit a fast-slow decomposition (quasi-equilibrium to equilibrium), which is further extended in reference [52] to thermal multi-component flows. Other approaches are based on a single global collision term such as Asinari's model [53], derived from the AAP-BGK collision operator [54]. The equilibrium velocity for each species is given by the conservation of species momenta. Diffusive and viscous effects are separated in the momentum space. References [55, 56, 57] have slightly modified the formulation of the equilibrium state and the definition of the equilibrium velocity, and applications to electrolytes are reported in Ref. [58].

All the previous models have very different formulations, but it is worth pointing out that for binary mixtures, they can be written as

$$\frac{\partial f_\alpha^m}{\partial t} + \mathbf{e}_\alpha^m \cdot \nabla f_\alpha^m = -\frac{1}{\tau_m} (f_\alpha^m - G_\alpha^{m(eq)}), \quad \text{for } m = 1, 2. \quad (4.1)$$

$G_\alpha^{m(eq)}$ is a local equilibrium which varies according to the considered model. Nonetheless, the right-hand side, the collision step, always obeys to

$$\sum_\alpha \frac{1}{\tau_m} (f_\alpha^m - G_\alpha^{m(eq)}) = 0, \quad (4.2)$$

$$\sum_\alpha \mathbf{e}_\alpha^m \frac{1}{\tau_m} (f_\alpha^m - G_\alpha^{m(eq)}) = A_{mn}(\mathbf{u}_m - \mathbf{u}_n) = A_{mn} \frac{\rho}{\rho_n} (\mathbf{u}_m - \mathbf{u}), \quad (4.3)$$

where A_{mn} may depend on the component density, pressure, diffusion coefficient, etc, but not on the velocities. The first equation means that there is no source term for the mass as expected. The second equation states that species momentum is no longer conserved during the collision, and the momentum variation has a similar form as the friction force

mentioned in the Maxwell-Stefan derivation. The other higher-order moments of the collision differ according to the different models, and no other similitude can be found.

The different mesoscopic models lead to various macroscopic equations. The notion of species momentum balance equations and species viscous stress are often not highlighted. Instead, previous authors generally focus on recovering the total (mixture) momentum equation. Consequently, even if a distribution function (and the related moments: density, momentum, etc) for each component of the mixture is defined, most previous LBM models for multiple species flows employed the assumption of a mixture viscosity for all species rather than using a viscous diffusion proper to each component as we could expect. Besides, the collision is usually heavily modified compared to the standard formulation to take into account the interactions between species. This increase of complexity makes the algorithm more computationally expensive, and above all, it can not be incorporated easily in existing LBM codes since the collision step has to be rewritten. Finally, a more simple way may exist by introducing the friction forces directly in the lattice Boltzmann formulation. This results in the separation of how to handle two physical phenomena in LBM: viscous dissipation is related to the BGK collision operator and (molecular) diffusion is associated with the inter-molecular friction force. This idea will be developed in the next chapter.

This approach should not be seen as inferior compared to prior models that try to implement the interaction from a purely collision-based point of view. Indeed, an accurate description of the kinetic of mixtures of gases with the LBM is a pipe-dream considering the over-simplified (BGK-like) collision operator, the use of average transport coefficients (mixture viscosity and mixture average diffusion coefficient), and last the limitation caused by the truncation of the velocity space which restricts us to gases not too far from their equilibrium state, i.e., Navier-Stokes level of description.

In this chapter, we present a lattice Boltzmann model for the simulation of miscible gases where the diffusion between species is taken to account by means of a friction force. Furthermore, to be rather complete, we discuss the formulation of transport coefficients, in the proposed approach no average assumption is required, and they are derived from the kinetic theory of gases. We also address the problem of simulation species having dissimilar molecular masses. This issue is specific to the LBM for mixtures because of the fixed speed of sound on the lattice. This difficulty is circumvented by using a forcing term to alter the species equation of state. This latter force, the friction force, and the formulation of the transport coefficients constitute the three building blocks of the present model. The model satisfies the indifferenciability principle, namely, for a mixture of like gases, it reduces to a single species BGK model. In addition, the macroscopic Maxwell-Stefan equations are recovered for purely diffusive flows when convection is negligible. One major advantage of the proposed method is the easiness of implementation. Since the collision is not modified, the method can be introduced in any other lattice Boltzmann algorithm to take into account complex diffusion among species.

Chapter 5

A simplified kinetic model for multi-component mixtures

5.1 Lattice Boltzmann algorithm

A mixture is composed of multiple species and each species is defined by its own distribution function, which is governed by its own kinetic equation. For the sake of simplicity we consider only a BGK-like collision operator. More advanced collisions operators such as multiple relaxation time, entropic, regularized, or cumulant operators, mostly developed to remedy some stability defects, could also be implemented [21, 27, 28, 31]. Let m and n denote different species ($m, n = 1, 2, \dots, N$; N being the total number of species). The distribution function of species m , f_α^m , obeys the following discrete kinetic equation:

$$f_\alpha^m(\mathbf{x} + \mathbf{e}_\alpha \delta_t, t + \delta_t) = f_\alpha^m(\mathbf{x}, t) - \frac{\delta_t}{\tau_m} \left[f_\alpha^m(\mathbf{x}, t) - f_\alpha^{m(eq)}(\mathbf{x}, t) \right] + \left(1 - \frac{\delta_t}{2\tau_m}\right) \delta_t S_\alpha^m(\mathbf{x}, t) \quad (5.1)$$

where \mathbf{x} , t , α , and τ_m are, respectively, the spatial coordinate, the time, the number of discrete kinetic velocities \mathbf{e}_α , and the relaxation time of each species. The equilibrium distribution functions, $f_\alpha^{m(eq)}$, are given by the standard polynomial formulation

$$f_\alpha^{m(eq)} = \rho_m \omega_\alpha \left[1 + \frac{\mathbf{u}_m \cdot \mathbf{e}_\alpha}{c_s^2} + \frac{(\mathbf{u}_m \cdot \mathbf{e}_\alpha)^2}{2c_s^4} - \frac{\mathbf{u}_m \cdot \mathbf{u}_m}{2c_s^2} \right]. \quad (5.2)$$

S_α^m is the source term for each species similar to Guo's forcing scheme [13], widely used in order to include forces in the lattice Boltzmann algorithm,

$$S_\alpha^m = \omega_\alpha \left[\frac{\mathbf{e}_\alpha - \mathbf{u}_m}{c_s^2} + \frac{(\mathbf{e}_\alpha \cdot \mathbf{u}_m) \mathbf{e}_\alpha}{c_s^4} \right] \cdot \mathbf{F}_m, \quad (5.3)$$

\mathbf{F}_m being the force acting on the m th species which is derived in the following to take into account the species interactions.

In this study, we use the so-called D2Q9 isothermal, two-dimensional and nine-velocity discretisation. Extension to the three-dimensional formulation (D3Q19 or D3Q27) is straightforward. The pseudo sound velocity is $c_s^2 = \frac{1}{3}$, the kinetic velocities are expressed as

$$\mathbf{e}_\alpha = \begin{bmatrix} 0 & 1 & 0 & -1 & 0 & 1 & -1 & -1 & 1 \\ 0 & 0 & 1 & 0 & -1 & 1 & 1 & -1 & -1 \end{bmatrix}^T \quad 1 \leq \alpha \leq 9, \quad (5.4)$$

and the lattice weights are equals to

$$\omega_\alpha = \left[\frac{4}{9} \quad \frac{1}{9} \quad \frac{1}{9} \quad \frac{1}{9} \quad \frac{1}{9} \quad \frac{1}{36} \quad \frac{1}{36} \quad \frac{1}{36} \quad \frac{1}{36} \right]^T \quad 1 \leq \alpha \leq 9. \quad (5.5)$$

The macroscopic quantities, namely the density and momentum of each species, are obtained by computing the different moments of the distribution functions.

$$\rho_m = \sum_\alpha f_\alpha^m, \quad \rho_m \mathbf{u}_m = \sum_\alpha f_\alpha^m \mathbf{e}_\alpha + \frac{\delta t}{2} \mathbf{F}_m. \quad (5.6)$$

The resulting macroscopic equations are the conservation equations for low Mach number flows subjected to a body force (for example, the gravity). In order to take into account the interaction of miscible species, we introduce diffusion forces or friction forces from the Maxwell-Stefan approach to mass transfer:

$$\mathbf{F}_{\mathcal{D},m} = -p \sum_{n=1}^N \frac{x_m x_n}{\mathcal{D}_{mn}} (\mathbf{u}_m - \mathbf{u}_n), \quad (5.7)$$

and \mathbf{F}_m becomes

$$\mathbf{F}_m = \mathbf{F}_{\mathcal{D},m} + \mathbf{F}_{\mathcal{B},m}, \quad (5.8)$$

where $\mathbf{F}_{\mathcal{B},m}$ is a body force. As a result, the discrete kinetic equations (5.1) for the various species are coupled through \mathbf{F}_m . Since the diffusion force $\mathbf{F}_{\mathcal{D},m}$ depends on the velocity, total pressure p , molar fractions x_m , and (Maxwell-Stefan) diffusion coefficients \mathcal{D}_{mn} , a linear system must be solved at each time step in order to compute the species momentum by means of Eq. (5.6). This force also called inter-molecular friction force depends on the relative velocity of species. Thus, when all species have the same velocity, no diffusion occurs. Notice that the intra-molecular friction, related to the viscosity, is already taken into consideration by the BGK collision similar to the case of a single component flow. The attempt to include the diffusion effects as a force acting on particles dates back to the early work on kinetic theory by Maxwell [38]. The same expression has been rigorously derived later by Chapman and Cowling [2], a detailed discussion is given by Hirschfelder, Curtiss, and Bird [1] (see also Ref. [34]) and Kerkhof and Geboers present a more recent derivation in Ref. [59]. Extended mathematics have to be performed to obtain this inter-molecular friction force from the kinetic theory, thus no derivation will be provided. The main steps of the derivation involve the use of the Chapman and Enskog expansion, the linearization of the collision integral Eq. (1.10) and its approximate solution by means of

a series expansion of the velocity distributions in Sonine, also called Laguerre, (and not Hermite) polynomials. An equivalent method using Hermite polynomials, Grad's 13th moment equations for mixtures, has been proposed by Zhdanov [60].

We return to the linear system involving the velocity, which can be written as

$$[Q_{mn}](\mathbf{u}_m) = (\mathbf{R}_m), \quad (5.9)$$

where $[Q_{mn}]$ is a square symmetric N -dimensional matrix equals to

$$Q_{mn} = -p\delta_t \frac{x_m x_n}{2\mathcal{D}_{mn}} \quad \text{for } m \neq n, \quad (5.10)$$

$$Q_{mm} = \rho_m - \sum_{n=1, n \neq m}^N Q_{mn}, \quad \text{and} \quad (5.11)$$

$$\mathbf{R}_m = \sum_{\alpha} e_{\alpha} f_{\alpha}^m + \frac{\delta_t}{2} \mathbf{F}_{\mathcal{B},m}. \quad (5.12)$$

This matrix has some nice properties, it is symmetric, diagonally dominant, and the diagonal terms are strictly positive. In consequence, the matrix is invertible and definite positive. The system can be solved efficiently by using Cholesky's decomposition.

5.2 Species with different molecular masses

In the standard lattice Boltzmann equation, the pseudo (isothermal) speed of sound (c_s) is fixed by the lattice. For D2Q9 velocity set, c_s is equal to $c_s^2 = 1/3$ (in lattice units for a reference temperature and molecular mass) for all species, which is not the case for mixture of species having different molecular masses. Indeed, recalling that the partial pressure obeys the ideal gas law, from the definition of the isothermal speed of sound of a species ($c_{s,m}^2 = \frac{\partial p_m}{\partial \rho_m}|_T$), one defines $c_{s,m}^2 = RT/M_m$ and $p_m = \rho_m c_{s,m}^2$, where R is the universal gas constant.

In order to account for the differences in the species pseudo speed of sound, one can modify the equilibrium distribution functions [61]. However, as shown by those authors, the maximum molecular mass ratio is limited to three. Furthermore, this approach adds some errors in the viscous stress tensor which can be reduced by increasing the velocity set from D2Q9 to D2Q13 [62]. Nonetheless, the molar mass ratio is still limited to three because of stability issues, and expanding the number of velocities makes the algorithm more complex and costly. Another strategy is to set the pseudo speed of sound in terms of the minimum molecular mass [61]. Thus, in one time step, the lightest species streams exactly to the next lattice point, while the heavier species stream between the original lattice point and the next one. Populations for the heavier species are then interpolated to the next lattice point. This process can simulate binary diffusion with molar mass ratio up to nine before the accuracy decreases because of the interpolation that adds numerical diffusion. This approach is very expensive. Indeed, it requires the use of an interpolation scheme for each species populations in each kinetic velocity directions (i.e., 8 in D2Q9).

In the present study, a variable pseudo speed of sound is introduced through a body force [63]. This strategy is simple since neither interpolation, nor extended velocity set, nor modified equilibrium is required. In particular, Guo's forcing scheme [13] is used, and the forcing term is calculated according to

$$\mathbf{F}_{\mathcal{B},m} = (1 - \beta_m)c_s^2 \nabla \rho_m, \quad (5.13)$$

where the gradient term is computed by means of a compact scheme

$$\nabla \rho_m(\mathbf{x}) = \frac{1}{c_s^2} \sum_{\alpha} \omega_{\alpha} \mathbf{e}_{\alpha} \rho_m(\mathbf{x} + \mathbf{e}_{\alpha}). \quad (5.14)$$

The partial pressure then becomes

$$p_m = \beta_m c_s^2 \rho_m, \quad (5.15)$$

where $\beta_m = c_{s,m}^2/c_s^2$ is the ratio between the species and the standard LBM pseudo speed of sound. This forcing strategy changes only the equation of state, and the relation between the partial pressure and density is modified according to the molecular mass of the species. This approach has also the advantage that the partial viscosity [Eq. (6.3)] is always defined in terms of the standard LBM pseudo speed of sound c_s . In practice, we usually define a reference species n whose speed of sound is the same as c_s equal to $1/3$ in lattice units ($\beta_n = 1$, $p_n = \rho_n c_s^2 = \rho_n RT/M_n$) and $\beta_m = M_n/M_m$ are then the ratio of molecular masses ($p_m = \rho_m c_{s,m}^2 = \rho_m c_s^2 \beta_m = \rho_m RT/M_m$).

Chapter 6

Macroscopic limit

6.1 Macroscopic equations

In this section we present the macroscopic limit of the proposed model via the Chapman-Enskog analysis. This multiple scale expansion provides a relation between the mesoscopic scale of the Boltzmann equation and the macroscopic scale of the Navier-Stokes equation. This derivation is straightforward and is similar to the standard lattice Boltzmann model with a force arising from Guo's forcing scheme (see Sec. 2.5 or Ref. [13]). Therefore in the low Mach and continuum limit, the kinetic equation (5.1) and its moments (5.6) are equivalent to the following macroscopic equations:

$$\partial_t \rho_m + \nabla \cdot (\rho_m \mathbf{u}_m) = 0, \quad (6.1)$$

$$\begin{aligned} \partial_t (\rho_m \mathbf{u}_m) + \nabla \cdot (\rho_m \mathbf{u}_m \mathbf{u}_m) = & -\nabla p_m + \nabla \cdot \left[\mu_m \left(\nabla \mathbf{u}_m + (\nabla \mathbf{u}_m)^T \right) \right] \\ & - p \sum_{n=1}^N \frac{x_m x_n}{\mathcal{D}_{mn}} (\mathbf{u}_m - \mathbf{u}_n) + \mathbf{F}_{\mathcal{B},m} \end{aligned} \quad (6.2)$$

where the partial pressure is equal to $p_m = \rho_m c_s^2$, and the total pressure is given by Dalton's law $p = \sum_{m=1}^N p_m$. The dynamic viscosity of species m is expressed in terms of the relaxation time according to

$$\mu_m = \rho_m c_s^2 \left(\tau_m - \frac{\delta_t}{2} \right). \quad (6.3)$$

6.2 Some variations on the equation formulation

Previous equations are expressed in the frame of reference of a given species m . Equations for the whole mixture can be obtained by summation over all species. From Eq. (6.1), the continuity equation for the mixture is recovered:

$$\partial_t \rho + \nabla \cdot (\rho \mathbf{u}) = 0, \quad (6.4)$$

with $\rho = \sum_m \rho_m$ and $\rho \mathbf{u} = \sum_m \rho_m \mathbf{u}_m$. Similarly, the balance equation for the mixture momentum reads

$$\partial_t(\rho \mathbf{u}) + \nabla \cdot (\rho \mathbf{u} \mathbf{u}) = -\nabla p + \nabla \cdot \left[\mu \left(\nabla \mathbf{u} + (\nabla \mathbf{u})^T \right) \right] + \sum_m \mathbf{F}_{B,m} + \Upsilon, \quad (6.5)$$

where the mixture viscosity is $\mu = \sum_m \mu_m$, and Υ is the collected terms specific to the species acting on the mixture momentum. Υ is composed of two contributions stemming from the species stress tensor and the species convective term, which the derivations are given below.

In order to avoid any confusion, the symbols \otimes is employed to specify the outer-product. This tensor operator is not commutative. The identity $(\alpha \mathbf{u}) \otimes \mathbf{v} = \mathbf{u} \otimes (\alpha \mathbf{v}) = \alpha(\mathbf{u} \otimes \mathbf{v})$ will be useful as well as the distributive property over the vector addition: $\mathbf{u} \otimes (\mathbf{v} + \mathbf{w}) = \mathbf{u} \otimes \mathbf{v} + \mathbf{u} \otimes \mathbf{w}$ and $(\mathbf{u} + \mathbf{v}) \otimes \mathbf{w} = \mathbf{u} \otimes \mathbf{w} + \mathbf{v} \otimes \mathbf{w}$. Starting from the mixture momentum $\rho \mathbf{u} = \sum_m \rho_m \mathbf{u}_m$, one defines a species "diffusion" velocities: $\mathbf{v}_m = \mathbf{u}_m - \mathbf{u}$.

Concerning the convective part, one can write

$$\sum_m (\rho_m \mathbf{v}_m \otimes \mathbf{v}_m) = \sum_m [\rho_m (\mathbf{u}_m - \mathbf{u}) \otimes (\mathbf{u}_m - \mathbf{u})] \quad (6.6)$$

$$= \sum_m [\rho_m \mathbf{u}_m \otimes \mathbf{u}_m - \rho_m \mathbf{u}_m \otimes \mathbf{u} - \rho_m \mathbf{u} \otimes \mathbf{u}_m + \rho_m \mathbf{u} \otimes \mathbf{u}] \quad (6.7)$$

$$= \sum_m (\rho_m \mathbf{u}_m \otimes \mathbf{u}_m) - \sum_m (\rho_m \mathbf{u}_m \otimes \mathbf{u}) - \sum_m (\mathbf{u} \otimes \rho_m \mathbf{u}_m) + \sum_m (\rho_m \mathbf{u} \otimes \mathbf{u}) \quad (6.8)$$

$$\begin{aligned} &= \sum_m (\rho_m \mathbf{u}_m \otimes \mathbf{u}_m) - \sum_m \begin{bmatrix} \rho_m u_{m,x} u_x & \rho_m u_{m,x} u_y & \rho_m u_{m,x} u_z \\ \rho_m u_{m,y} u_x & \rho_m u_{m,y} u_y & \rho_m u_{m,y} u_z \\ \rho_m u_{m,z} u_x & \rho_m u_{m,z} u_y & \rho_m u_{m,z} u_z \end{bmatrix} \\ &- \sum_m \begin{bmatrix} u_x \rho_m u_{m,x} & u_x \rho_m u_{m,y} & u_x \rho_m u_{m,z} \\ u_y \rho_m u_{m,x} & u_y \rho_m u_{m,y} & u_y \rho_m u_{m,z} \\ u_z \rho_m u_{m,x} & u_z \rho_m u_{m,y} & u_z \rho_m u_{m,z} \end{bmatrix} + \sum_m (\rho_m \mathbf{u} \otimes \mathbf{u}) \end{aligned} \quad (6.9)$$

$$= \sum_m (\rho_m \mathbf{u}_m \otimes \mathbf{u}_m) - \rho \mathbf{u} \otimes \mathbf{u} - \mathbf{u} \otimes (\rho \mathbf{u}) + \rho \mathbf{u} \otimes \mathbf{u} \quad (6.10)$$

$$= \sum_m (\rho_m \mathbf{u}_m \otimes \mathbf{u}_m) - \rho \mathbf{u} \otimes \mathbf{u}, \quad (6.11)$$

where the scalar identify is used to obtain Eq. (6.8) from Eq. (6.7) and Eq. (6.11) from Eq. (6.10), and the distributive property is used to obtain Eq. (6.10) from Eq. (6.8). In consequence, one can find

$$\sum_m \nabla \cdot (\rho_m \mathbf{u}_m \otimes \mathbf{u}_m) = \nabla \cdot (\rho \mathbf{u} \otimes \mathbf{u}) + \sum_m \nabla \cdot (\rho_m \mathbf{v}_m \otimes \mathbf{v}_m). \quad (6.12)$$

In addition, the summation of the species stress tensor over all species gives

$$\sum_m \nabla \cdot \left[\mu_m \left(\nabla \mathbf{u}_m + (\nabla \mathbf{u}_m)^T \right) \right] = \sum_m \nabla \cdot \left[\mu_m \left(\nabla (\mathbf{v}_m + \mathbf{u}) + (\nabla \mathbf{v}_m + \mathbf{u})^T \right) \right] \quad (6.13)$$

$$= \sum_m \nabla \cdot \left[\mu_m \left(\nabla \mathbf{v}_m + (\nabla \mathbf{v}_m)^T \right) \right] + \nabla \cdot \left[\sum_m \mu_m \left(\nabla \mathbf{u} + (\nabla \mathbf{u})^T \right) \right] \quad (6.14)$$

$$= \sum_m \nabla \cdot \left[\mu_m \left(\nabla \mathbf{v}_m + (\nabla \mathbf{v}_m)^T \right) \right] + \nabla \cdot \left[\mu \left(\nabla \mathbf{u} + (\nabla \mathbf{u})^T \right) \right] \quad (6.15)$$

The extra terms (compared to the single fluid theory) in the mixture momentum equation are gathered in upsilon:

$$\Upsilon = - \sum_m \nabla \cdot (\rho \mathbf{v}_m \mathbf{v}_m) + \sum_m \nabla \cdot \left[\mu_m \left(\nabla \mathbf{v}_m + (\nabla \mathbf{v}_m)^T \right) \right]. \quad (6.16)$$

The first terms is reminiscent of the Reynolds's stresses in turbulent flow and the second term may be related to the Korteweg stresses observed experimentally with miscible liquids in capillarity flows [64, 65]. These phenomena could have a non-negligible effect on the interface between the fluids. In consequence, Υ is generally not zero.

6.3 Limit expressions

6.3.1 Pure diffusion

We now focus on the limit expressions of the previous equations. Using the dimensionless formulations of Eqs (6.1) and (6.2), one can estimate, *a priori*, the order of magnitude of each term. In the following, we will show that the Maxwell-Stefan equations are recovered in the case of pure diffusion. We first begin with the inter-molecular friction force, which yields to the estimate

$$\mathbf{F}_{\mathcal{D},m} = -p \sum_{n=1}^N \frac{x_m x_n}{\mathcal{D}_{mn}} (\mathbf{u}_m - \mathbf{u}_n) = \mathcal{O}(p_{ref} u_{\Delta} / \mathcal{D}_{ref}), \quad (6.17)$$

where u_{Δ} is an appropriate velocity difference between species, and quantities with the ref subscript represent an estimate of their order of magnitude. In a similar way, we have

$$\partial_t (\rho_m \mathbf{u}_m) = \mathcal{O}(\rho_{ref} u_{ref} / t_{ref}), \quad (6.18)$$

$$\nabla \cdot (\rho_m \mathbf{u}_m \mathbf{u}_m) = \mathcal{O}(\rho_{ref} u_{ref}^2 / L_{ref}), \quad (6.19)$$

$$\nabla p_m = \mathcal{O}(p_{ref} / L_{ref}), \quad (6.20)$$

$$\nabla \cdot \left\{ \mu_m \left[\nabla \mathbf{u}_m + (\nabla \mathbf{u}_m)^T \right] \right\} = \mathcal{O}(\mu_{ref} u_{ref} / L_{ref}^2). \quad (6.21)$$

The species momentum convection can be neglected compared to the diffusion if Eq. (6.19) \ll Eq. (6.17), i.e., $\text{Ma}^2 \ll \text{Pe}_\Delta$, where the Mach number is defined as $\text{Ma} = u_{ref}/c_{s,ref}$ and the Péclet number is $\text{Pe} = L_{ref}u_\Delta/\mathcal{D}_{ref}$. Similarly, the shear forces are negligible if Eq. (6.21) \ll Eq. (6.17), i.e., $\text{Ma}^2 \ll \text{Pe}_\Delta \text{Re}$ with $\text{Re} = L_{ref}u_{ref}/\nu_{ref}$. As u_Δ may change during the mixing, the influence of the different terms in Eq. (6.2) may vary in time and space.

Let assume a low Mach flow whose dynamic is mostly diffusive. We can neglect the contributions associated with convection ($\text{Ma}^2 \ll \text{Pe}_\Delta$) and shear forces ($\text{Ma}^2 \ll \text{Pe}_\Delta \text{Re}$). In addition, the characteristic time is given by $t_{ref} = L_{ref}^2/\mathcal{D}_{ref}$ and $u_{ref} = u_\Delta$, therefore the species acceleration can also be neglected, Eq. (6.18) \ll Eq. (6.17). Hence, Eq. (6.2) reduces to

$$\nabla p_m = p \sum_{n=1}^N \frac{x_m x_n}{\mathcal{D}_{mn}} (\mathbf{u}_n - \mathbf{u}_m). \quad (6.22)$$

If we sum this equation over all species, we obtain

$$\nabla p = 0. \quad (6.23)$$

As a result for this specific case, the process is isobaric. Using Dalton's law, Maxwell-Stefan's equations are easily recovered from Eq. (6.22):

$$\begin{aligned} \nabla x_m &= \sum_{n=1}^N \frac{x_m x_n}{\mathcal{D}_{mn}} (\mathbf{u}_n - \mathbf{u}_m) \\ &= \sum_{n=1}^N \frac{x_m \mathbf{N}_n - x_n \mathbf{N}_m}{c_t \mathcal{D}_{mn}}, \end{aligned} \quad (6.24)$$

where we have introduced the species molar concentration $c_m = x_m c_t$ and the species molar flux $\mathbf{N}_m = c_m \mathbf{u}_m$, c_t being the mixture molar concentration. In the case of an equimolar binary mixture, Fick's law is obtained $\mathbf{N}_1 = -c_t \mathcal{D}_{12} \nabla x_1$ or $\mathbf{u}_1 = -x_1^{-1} \mathcal{D}_{12} \nabla x_1$.

6.3.2 Poiseuille flow

In order to investigate the influence of the inclusion of inter-molecular friction force, we derive the solution of a two-dimensional planar Poiseuille flow for a spatially homogeneous binary mixture. We consider a flat channel of height $2h$. The previous momentum Eq. (6.2) is written in a dimensionless formulation using non-dimensional quantities $p^* = p/(\rho U^2)$, $u_m^* = u_m/U$, $x^* = x/h$, and $y^* = y/h$ with $y^* \in [-1, 1]$. One finds

$$-x_1 \frac{dp^*}{dx^*} + \frac{1}{\text{Re}_1} \partial_{y^*}^2 (u_1^*) + \text{Pe} p^* x_1 x_2 (u_2^* - u_1^*) = 0, \quad (6.25)$$

$$-x_2 \frac{dp^*}{dx^*} + \frac{1}{\text{Re}_2} \partial_{y^*}^2 (u_2^*) + \text{Pe} p^* x_1 x_2 (u_1^* - u_2^*) = 0, \quad (6.26)$$

where we define the species Reynolds number $\text{Re}_m = \rho U h / \mu_m$, which corresponds to the Reynolds number if the species is alone. The mixture Reynolds number is given by $\text{Re} = \rho U h / \mu = \text{Re}_1 \text{Re}_2 / (\text{Re}_1 + \text{Re}_2)$, and the usual Péclet number is $\text{Pe} = U h / \mathcal{D}_{12}$. By differentiating two times the first equation along the y -direction and subsequently eliminating u_2^* , a fourth order linear differential equation for u_1^* is obtained

$$\partial_{y^* y^* y^* y^*}^4 (u_1^*) - \text{Pe}(\text{Re}_1 + \text{Re}_2) p^* x_1 x_2 \partial_{y^* y^*}^2 (u_1^*) = -\text{Pe} \text{Re}_1 \text{Re}_2 p^* x_1 x_2 \frac{dp^*}{dx^*} \quad (6.27)$$

We assume a non-slip velocity condition at the top and bottom boundaries such as

$$u_m^*(y^* = -1) = 0, \text{ and } u_m^*(y^* = 1) = 0, \quad m = 1, 2. \quad (6.28)$$

It should be noted that a velocity slip boundary is usually used for mixture of gases in micro-channels due to rarefaction effects. Here, we suppose that the Knudsen number is small enough ($< 10^{-3}$, continuum flow regime) to neglect this phenomenon. With the help of the change of variable $X = \partial_{y^* y^*}^2 (u_1^*)$, we get for $m = 1, 2$:

$$\begin{aligned} u_m^*(y^*) &= \frac{\text{Re}}{2} \frac{dp^*}{dx^*} (y^{*2} - 1) \\ &+ (x_m \text{Re}_m - \text{Re}) \frac{dp^*}{dx^*} \frac{2}{\lambda^2} \frac{\sinh(\lambda)}{\sinh(2\lambda)} [\cosh(\lambda y^*) - \cosh(\lambda)], \end{aligned} \quad (6.29)$$

with

$$\lambda = \sqrt{\text{Pe}(\text{Re}_1 + \text{Re}_2) p^* x_1 x_2} \quad (6.30)$$

In Eq. (6.29), the first terms are the standard solution of a Poiseuille flow and the terms displayed on the second line is specific to the mixture. We recall that the mixture considered here is spatially homogeneous. Although the flow is caused by a pressure gradient and not a concentration difference, the species velocity profile is influenced by the presence of the other component. The maximal velocity of a standard Poiseuille profile is $U_{max}^* = -\frac{\text{Re}}{2} \frac{dp^*}{dx^*}$ where one generally sets $\frac{dp^*}{dx^*} < 0$ and we can rewrite the velocity profile as

$$\begin{aligned} u_m^*(y^*) &= U_{max}^* (1 - y^{*2}) \\ &- U_{max}^* [x_m (1 + \frac{\mu_n}{\mu_m}) - 1] \frac{4}{\lambda^2} \frac{\sinh(\lambda)}{\sinh(2\lambda)} [\cosh(\lambda y^*) - \cosh(\lambda)], \end{aligned} \quad (6.31)$$

for $m = 1, 2$ and $n \neq m = 1, 2$. The solution is well-defined for all values of λ and its limits are

$$\lim_{\lambda \rightarrow 0} u_m^*(y^*) = U_{max}^* [x_m (1 + \frac{\mu_n}{\mu_m})] (1 - y^{*2}), \quad m = 1, 2 \text{ and } n \neq m, \quad (6.32)$$

$$\lim_{\lambda \rightarrow \infty} u_m^*(y^*) = U_{max}^* (1 - y^{*2}). \quad (6.33)$$

In Figure 6.1, $u_m^*(y^* = 0)/U_{max}^*$ is plotted for the mixture composition $x_1 = 0.9$ and $x_2 = 0.1$ for various species viscosity ratios and λ values. From Eqs. (6.32) and (6.33),

one can deduce the influence of the molar fractions that mainly shifts up or down the plot for given λ . When the component viscosities differ greatly for small λ values, the species maximal velocity is larger than the usual maximal Poiseuille velocity for a given pressure gradient for the less viscous component and *vice versa* the species maximal velocity is smaller for the more viscous component.

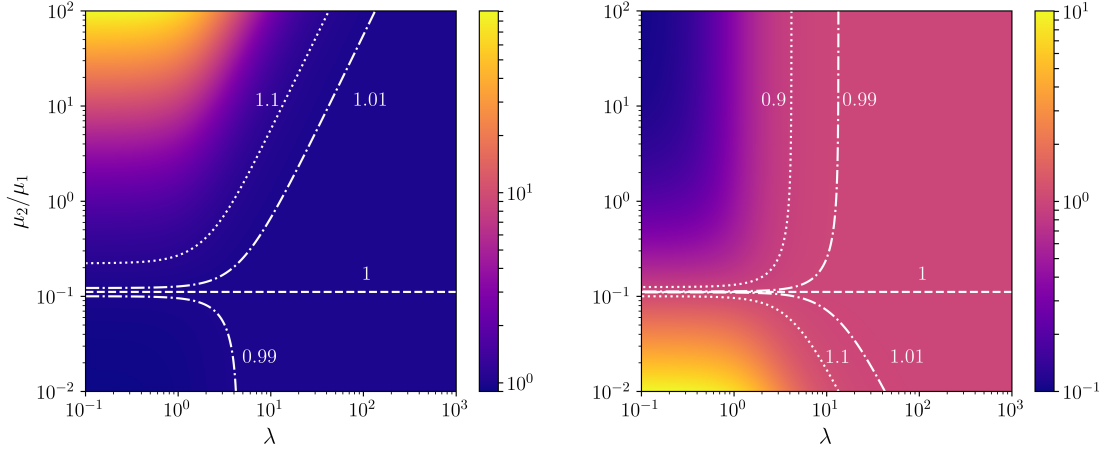


Figure 6.1 – $u_m^*(y^* = 0)/U_{max}^*$ for $x_1 = 0.9$, $x_2 = 0.1$ for different viscosity ratios and lambda values.

In reality, the component viscosity and λ are not independent parameters since they are related to the mixture composition and the transport coefficients (viscosity, diffusion coefficient) which depend on the molecular properties of the components. More details on transport coefficients will be given in the next section. For simple gases at atmospheric pressure, we can estimate the value of λ as

$$\lambda = \sqrt{\frac{1}{\mathcal{D}_{12}} \left(\frac{1}{\mu_1} + \frac{1}{\mu_2} \right) h^2 p x_1 x_2} \quad (6.34)$$

$$\approx \sqrt{10^5 \times (10^5 + 10^5) \times h^2 \times 10^5 \times 0.9 \times 0.1} \quad (6.35)$$

$$\approx h \times 10^7 \quad (6.36)$$

In this case, the species velocity profile does not follow the usual Poiseuille profile only for very small channels $h < 0.01\text{mm}$ ($\lambda < 100$). We point out that for a non-homogeneous mixture, we expect more deviations due to the diffusion. With this simple analytical solution, we have presented the mutual influence of two species in a Poiseuille flow. The species velocities may differ from the standard Poiseuille profile for a single fluid and, consequently, so does the resulting mixture velocity.

6.4 Transport coefficients

In the previous subsections, the equivalent macroscopic equations are presented. However the transport coefficients, viscosities, and diffusion coefficients still have to be defined.

The lattice Boltzmann scheme still retains a connection with the macroscopic scale through the relation between the relaxation time and the viscosity stemming from the Chapman-Enskog expansion [Eq. (6.3)]. Since each species has its own kinetic equation [Eq. (5.1)], N relaxation times (i.e., viscosities) need to be defined, and a relation between the mixture properties and species viscosity has to be specified. Some of the previous lattice Boltzmann multi-component models disregard this issue ([43, 46]), and others set the viscosities of each species equal to the mixture viscosity ([47, 48, 53, 55, 57]) or use Wilke's law ([51, 52]).

In the following, we present the submodel for the transport coefficients that we derive in the framework of the multi-fluid approach that constitutes one of the main features of our model. Fortunately, analytical expression for the transport coefficients for a dilute gas can be obtained by kinetic theory [1] (see also the reference [34], which is less detailed). By extending the works of Hirschfelder, Curtiss, and Bird to mixtures, Kerkhof and Geboers [59] define diffusion coefficients and species partial viscosities in terms of the molecular properties, temperature, and composition of the mixture.

In order to avoid confusion between pure viscosity and the viscosity of a species m in the mixture, we refer to the latter as the partial viscosity. Following Kerkhof and Geboers, the partial viscosities can be computed by solving the linear system

$$(\mu_m) = [P_{mn}]^{-1} \begin{pmatrix} 1 \\ \vdots \\ 1 \end{pmatrix} \quad (6.37)$$

with

$$P_{mm} = \frac{2}{k_B T} \left[\frac{4}{5} \Omega_{mm}^{(2,2)} + \sum_{n \neq m}^N \frac{x_n}{x_m} \frac{16}{15} \frac{\mathcal{M}_n}{(\mathcal{M}_m + \mathcal{M}_n)^2} \times \left(5 \mathcal{M}_m \Omega_{mn}^{(1,1)} + \frac{3}{2} \mathcal{M}_n \Omega_{mn}^{(2,2)} \right) \right] \quad (6.38)$$

and for off-diagonal elements ($n \neq m$),

$$P_{mn} = -\frac{2}{k_B T} \left[\frac{16}{15} \frac{\mathcal{M}_m \mathcal{M}_n}{(\mathcal{M}_m + \mathcal{M}_n)^2} \left(5 \Omega_{mn}^{(1,1)} - \frac{3}{2} \Omega_{mn}^{(2,2)} \right) \right], \quad (6.39)$$

where k_B is the Boltzmann constant, T the temperature, \mathcal{M}_m the mass of a single molecule for the species m , x_m the mole fraction, and the Ω -integrals are defined as in Ref. [1] and depend on the temperature and the molecular properties based on the Lennard-Jones potential (see Appendix C.1 for details). We underline that the matrix formulation of the partial viscosity can be found in Ref. [1] (§7.4.iii) if the summation over all species is not performed.

Combining some assumptions made in Ref. [1] (§8.2.iii) and additional approximations suggested in Ref. [66], the previous linear system can be simplified. This derivation is provided in Appendix C.2 for completeness since previous references do not use the same notation and thus is here available in a single consistent paragraph. Therefore, the partial viscosities depend on the composition of the mixture and can be expressed in terms of the molar fractions, the pure viscosities $\mu_{0,m}$, and the species molar masses, and a similar formula to Wilke's law is recovered yielding to

$$\mu_m = \frac{x_m \mu_{0,m}}{\sum_n^N x_n \Phi_{mn}} \quad (6.40)$$

with

$$\Phi_{mn} = \frac{1}{2\sqrt{2}} \left(1 + \frac{M_m}{M_n}\right)^{-\frac{1}{2}} \left[1 + \left(\frac{\mu_{0,m}}{\mu_{0,n}}\right)^{\frac{1}{2}} \left(\frac{M_n}{M_m}\right)^{\frac{1}{4}}\right]^2, \quad (6.41)$$

where $\mathcal{M}_m = M_m/\mathcal{N}_a$, with \mathcal{N}_a the Avogadro number and M_m the molar mass of species m . We point out that in kinetic theory, the pure viscosity has the following expression:

$$\mu_{0,m} = \frac{5k_B T}{8\Omega_{mm}^{(2,2)}}, \quad (6.42)$$

which is asymptotically consistent with Eqs. (6.38) and (6.39).

For the Maxwell-Stefan diffusion coefficients, we use the same expression obtained from the classical kinetic theory of gases [1] (see also Appendix C.3):

$$\mathcal{D}_{mn} = \mathcal{D}_{nm} = \frac{3(\mathcal{M}_m + \mathcal{M}_n) (k_B T)^2}{16p\mathcal{M}_m\mathcal{M}_n \Omega_{mn}^{(1,1)}}. \quad (6.43)$$

The diffusion coefficients are usually taken as constant at a given reference pressure and temperature since the pressure variation is not significant. In practice, the transport coefficients, pure viscosities and diffusion coefficients, can be set according to different strategies. For instance, they can be directly chosen in lattice units (as in Secs.7.1 and 7.2) depending on a given dimensionless number (Reynolds number, Péclet number, etc). In some cases, experimental values are available (as in Sec.7.3), or else the previous equations can be employed (as in Sec.7.4).

Chapter 7

Numerical simulations

In order to validate the proposed model, we present four two-dimensional cases referred to as A, B, C, and D. In case A, the forcing term approach is applied to the free decay of a density wave. In case B, two species having the same molecular mass diffuse in each other. These two cases are selected to assess the numerical capabilities of the proposed method, and the results are validated against analytical results. Then Loschmidt's tube experiment is reproduced in case C, which corresponds to the diffusion of a ternary mixture with different molecular masses. In case D, we simulate the interaction of two multi-component opposed jets. In all cases, the simulation is initialized with the equilibrium distribution Eq. (5.2).

7.1 A- Decay of a density wave

The accuracy of the forcing strategy to define the species pseudo speed of sound is assessed by simulating a single species flow corresponding to the decay of a free density wave damped by a low viscosity as proposed in Ref. [62]. By considering small perturbations of density and velocity from the linearized Navier-Stokes equations, the density and the velocity of the damped wave are given by

$$\rho = \rho_0 + \delta_\rho \exp(w_i t) \cos(kx - w_r t), \quad (7.1)$$

$$u = \frac{\delta_\rho}{k} \exp(w_i t) [w_r \cos(kx - w_r t) - w_i \sin(kx - w_r t)] \quad (7.2)$$

We perform simulations assuming two-dimensional periodic domain (n_x, n_y) . In order to compare our results with the analytical solution, we introduce the equivalent species pseudo speed of sound $c_e = \sqrt{\beta} c_s$ and ν the kinematic viscosity of the fluid, and set $\rho_0 = 1$ (average density), $\delta_\rho = 10^{-3}$ (amplitude of the density perturbation wave) and $\nu k / c_e = 10^{-2}$, k being the wave number $k = 2\pi / n_x$. In the harmonic decomposition, the dispersion relation yields a wave frequency that is split into a real and an imaginary

part:

$$w = w_r + iw_i, \quad (7.3)$$

$$w_r = \pm kc_e \sqrt{1 - \nu^2 k^2 / c_e^2}, \quad (7.4)$$

$$w_i = -kc_e(\nu k / c_e). \quad (7.5)$$

Simulations are carried out for different domain sizes n_x at various speed of sound ratios β while keeping $n_y = 5$ constant. As an example, we plot in Fig. 7.1 the temporal evolution of ρ and u at $n_x/4$ for $\beta = 0.05, 1, 4.3$ and $n_x = 128$. The dissipation error is undetectable and a small dispersion error is visible only for $\beta = 0.05$.

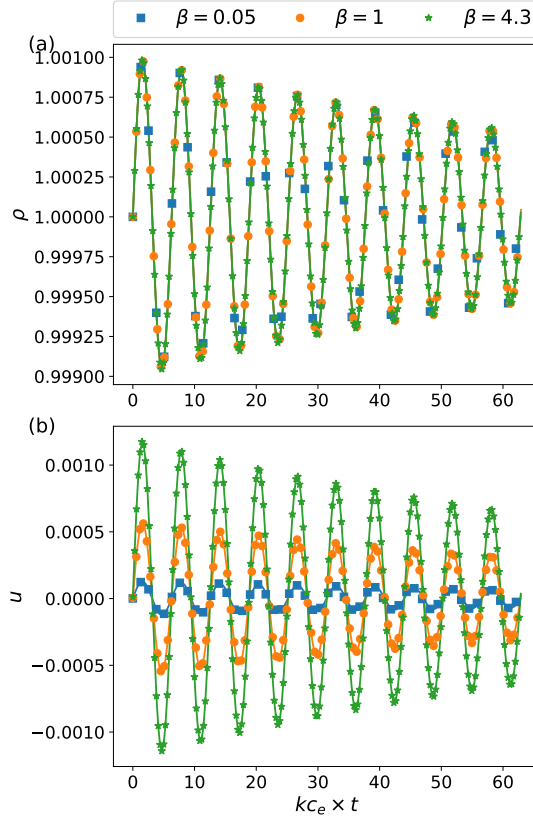


Figure 7.1 – (a) Temporal evolution of ρ and u (b) at $n_x/4$ for $\beta = 0.05, 1, 4.3$ and $n_x = 128$. Symbols and lines stand for simulation results and analytical solutions from Eqs. (7.1-7.2), respectively.

The relative global error of the density and the velocity field is defined in terms of the L2-norm

$$\varepsilon_\phi = \sqrt{\frac{\sum_i^{n_x} (\phi_i - \phi_{analytical,i})^2}{\sum_i^{n_x} \phi_{analytical,i}^2}}, \quad (7.6)$$

ϕ standing for either density or velocity. The results are compared at non dimensional time $ktc_e = 10 \times 2\pi$ and reported in Fig. 7.2 for various β and n_x . The model is found to be stable in the range $0.05 \leq \beta \leq 4.3$, indicating that our model is able to simulate molar mass ratios up to 86 with small errors on the density and velocity depending on the size of the grid and on the value of β .

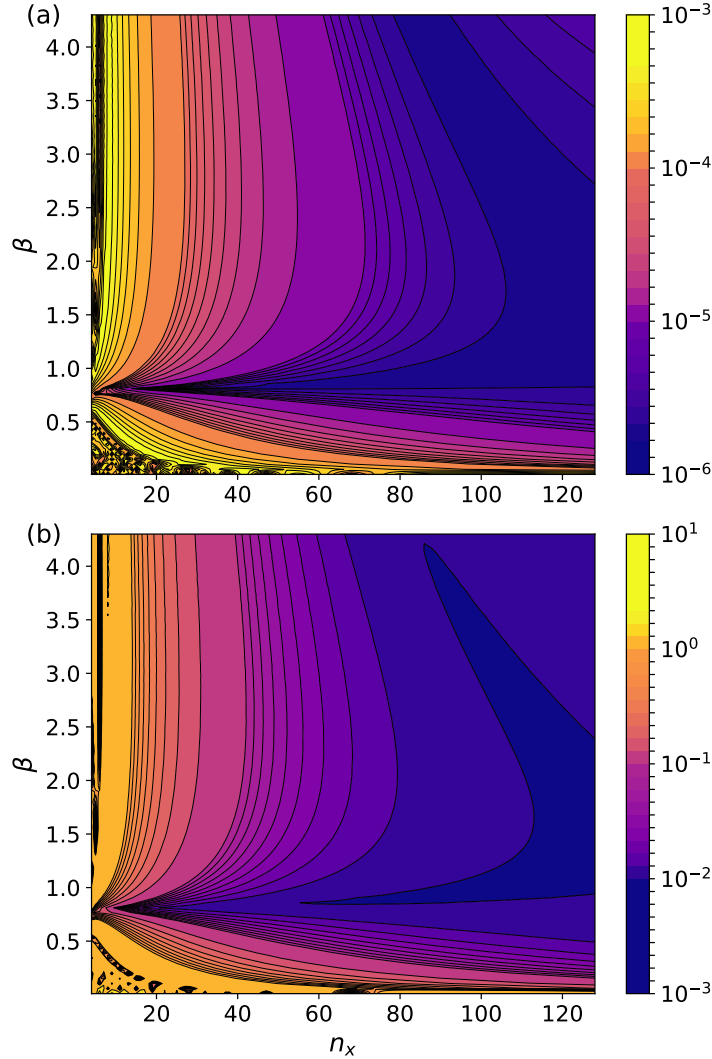


Figure 7.2 – (a) Relative errors of the density ε_ρ and velocity ε_u (b).

In Fig. 7.3, the proposed method is compared against the method of Ref. [62] where the equilibrium is modified and a larger velocity set is employed. The data are extracted from Fig.6 of Ref.[62] and the exact same case is simulated. With the proposed method, the relative errors are lower and the range of stable β values is greater. In Ref. [52], interpolations are used to simulate molecular weight ratios up to 1000. No direct com-

comparison is possible since no relative errors of the density and velocity are plotted, and both of these errors have different orders of magnitude. Nonetheless, the present method is easier to implement compare to interpolations which can be cumbersome to code in 3D, especially on boundary nodes. The gain in CPU time is not the main reason of the use of the proposed method. As a crude approximation, if we assume that the calculation of the density gradient has the same CPU cost as an interpolation of one distribution function, interpolations are $4 \times (N - 1)$ times more expensive than using a force to alter the equation of state in 2D where N is the number of species (one gradient calculation for each physical dimension vs one interpolation for each distribution function). For the $D3Q19$ velocity set, interpolations are approximately $6 \times (N - 1)$ more expensive. Anyway, the main CPU cost is as usual related to the collision operation.

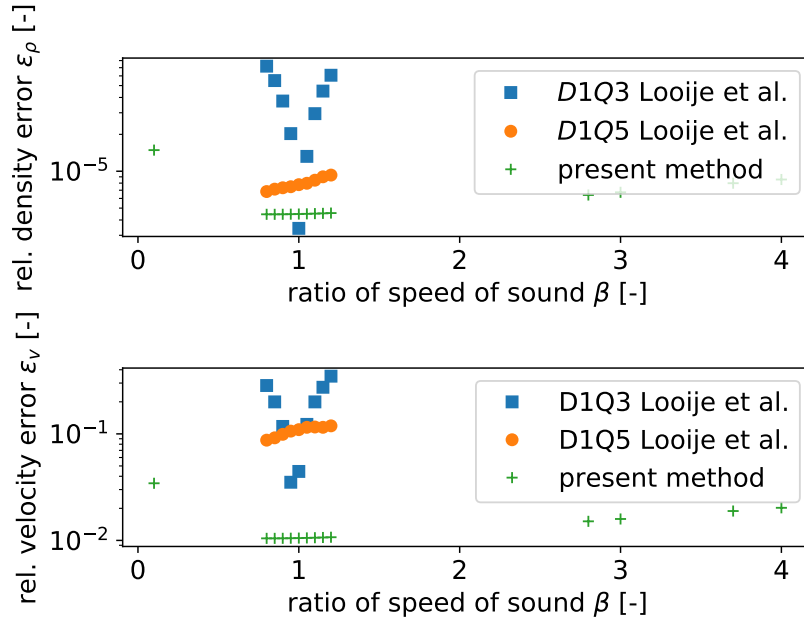


Figure 7.3 – Relative global errors for the decay of a density wave ($n_x = 256$).

7.2 B- Equimolar counter-diffusion

In this test case, we study the mixing between two species of equal molecular masses for which the mass transfer occurs only by diffusion, and governing equations are

$$\partial_t \rho_m = \mathcal{D} \nabla^2 \rho_m, \text{ for } m = 1, 2. \quad (7.7)$$

A particular solution of Eq. (7.7) is

$$\rho_m(x, t) = \rho_0 + (-1)^m \delta_\rho \exp(-k^2 \mathcal{D} t) \sin(kx). \quad (7.8)$$

We choose $\rho_0 = 1$, $\delta_\rho = 10^{-3}$, $k = 2\pi/n_x$, and use a two-dimensional periodic domain ($n_x = 200, n_y = 5$). As an example, we plot in Fig. 7.4 the temporal evolution of ρ_2 for $\mathcal{D} = 10^{-2}$ and $\tau = 1$ for both species. Numerical results are indistinguishable from the analytical solution Eq. (7.8).

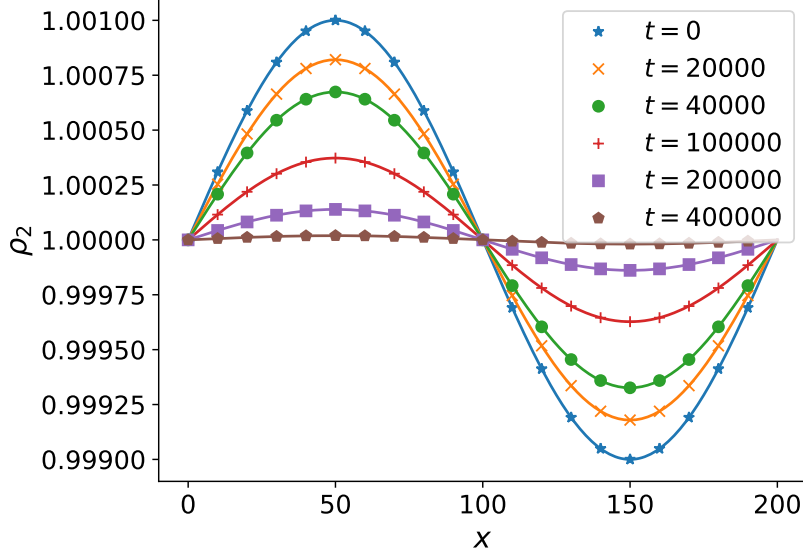


Figure 7.4 – Evolution of ρ_2 for $\tau = 1$ and $\mathcal{D} = 10^{-2}$ at different iterations. Symbols and lines stand for simulation results and analytical solutions from Eq. (7.8), respectively.

For comparison, we have evaluated the error of the diffusion coefficient at various \mathcal{D} and relaxation times τ (which is assumed to be the same for the two species). The relative error $\|D_{num} - D\|/D$ is reported in Fig. 7.5 where D_{num} is computed at $x = n_x/4$ by linear fit of Eq. (7.8) and D is set using Eq. (5.7). The numerical solution is in good agreement with the theoretical results for $\mathcal{D} < 0.1$ and for all relaxation times. We note that the relative error in density, ε_ρ as defined in Eq. (7.6), is three orders of magnitude smaller than the relative errors of the diffusion coefficient. The figure shows a discrepancy between the numerical and theoretical results for $\mathcal{D} > 0.1$. Having kept constant the size of the domain for all \mathcal{D} , this discrepancy is likely to be ascribed to a loss of spatial and temporal resolution. Nonetheless the relative error of the diffusion coefficient is always less than 0.4% for all τ . Different sizes of domain are used (not shown in the present study) and we recover the classic second-order accuracy in space indicating that the forcing approach does not deteriorate the accuracy of the LBM algorithm.

7.3 C- Loschmidt's tube

Having validated the ability of the method to simulate the decay of a single species density wave (at various different molar masses), and the counter-diffusion of species hav-

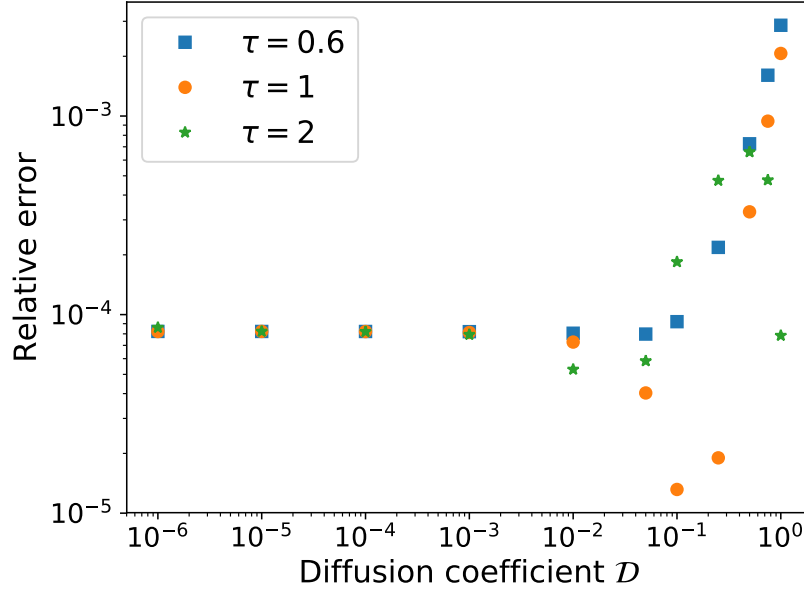


Figure 7.5 – Relative errors of the diffusion coefficient.

ing equal molecular masses (at various diffusion coefficients), we simulate the Loschmidt’s tube experiment [67]. The latter consists of the mixing of a ternary mixture of gases having different molecular masses (argon, methane, and hydrogen). For such a process, a diffusion reversal is observed depending on the initial species composition [41]. In particular, we have considered two tubes of the same dimension filled with mixtures of different composition in the left and right tubes that are joined at the beginning of the experiment. In the experiment the left and right mean compositions are measured in time during the mixing. In the experimental apparatus, the lengths of each tube is $L_{ref}/2 \approx 0.405$ and the period of observation is approximately 1h. The initial molar fractions are given in Table 7.1, and the other physical parameters are summarized in Table 7.2.

tube		x_{Ar}	x_{CH_4}	x_{H_2}
left	$(0 < x < L_{ref}/2)$	$0.509 - \delta$	2δ	$0.491 - \delta$
right	$(L_{ref}/2 < x < L_{ref})$	$0.485 - \delta$	$0.515 - \delta$	2δ

Table 7.1 – Initial molar fractions, in our simulation we take $\delta = 5 \times 10^{-4}$ (in the experiment, $\delta = 0$).

The simulation is carried out on a domain size of $(n_x, n_y) = (200, 25)$. Classical bounce-back rules are used on the left and right boundaries, and periodic conditions are applied on the top and bottom sides of the domain.

For computational purposes, we have rescaled the Maxwell-Stefan diffusion coeffi-

L_{ref}	[m]	$2\sqrt{1/60}\pi$		
p	[Pa]	101325		
T	[K]	307.15		
	m	Ar	CH_4	H_2
M_m	[g/mol]	39.948	16.0425	2.01588
$\mathcal{D}_{Ar\ m}$	[mm ² /s]	–	21.57	83.35
$\mathcal{D}_{CH_4\ m}$	[mm ² /s]	21.57	–	77.16
$\mathcal{D}_{H_2\ m}$	[mm ² /s]	83.35	77.16	–
$\mu_{0,m}$	[μPa/s]	22.83	11.35	9.18

Table 7.2 – Physical parameters of the experiment.

cients by a factor 10^3 , and the partial viscosities have been computed imposing the same species Schmidt numbers, which we define in terms of the pure viscosity as in the experiment. The aim of the rescaled factor is to increase the physical time step of the simulation and obtain results with less computational resources. Indeed, a rather small domain is used but Loschmidt’s experiment lasts 1h. Let us define the conversion factors between physical and LBM quantities for the length and the time:

$$C_l = \frac{l_{phy}}{l_{LBM}}, \quad C_t = \frac{t_{phy}}{t_{LBM}}. \quad (7.9)$$

In practice, we use the concept of lattice units where the LBM quantities are defined by space step $\delta_{x_{LBM}} = 1$ and time step $\delta_{t_{LBM}} = 1$. In physical units, the total length of the two tubes is 0.8112m and the domain size is equal to $n_x = 200$. This yields to a length conversion factor $C_l = 0.8112/200 = 4.056 \times 10^{-3}$ m. The diffusion coefficients, in lattice units, are given by:

$$\mathcal{D}_{LBM} = \mathcal{D}_{phy} \frac{C_t}{C_l^2} \quad (7.10)$$

Assuming the same diffusion coefficients in both LBM and physical systems results in $C_t = \frac{[s]}{[m^2]} C_l^2 = 1.6451 \times 10^{-5}$ s. The experience lasts about 1h which is approximately equivalent to 218×10^6 time steps in the LBM simulation. Using a rescaled factor and keeping the Schmidt number constant in both systems reproduce the same physics at a lower computational cost. Note that simulations with different sizes of the domain ($n_x = 200, 2000$) and rescaled factors ($10^3, 10^2$) leads to identical results subject to the standard LBM discretisation errors.

Figure 7.6 reports the evolution of the mean molar fractions for the left and right tubes in non-dimensional time units $t^* = t \times \mathcal{D}_{ArCH_4}/(L_{ref})^2$. The mean molar fractions are in very good agreement with the experimental data. As expected, initially argon diffuses in the same direction of the concentration gradient contrary to the behavior predicted by using Fick’s law. This reverse diffusion occurs on a scale of approximately 0.04 non-dimensional time units, and the concentration of argon attains a plateau in both tubes in spite of the presence of large concentration gradients. The other species do not exhibit such diffusion barrier. At later times, Fick’s like diffusion takes place. It

is important to point out that this complex diffusion dynamics can only be recovered by the Maxwell-Stephan equations [37].

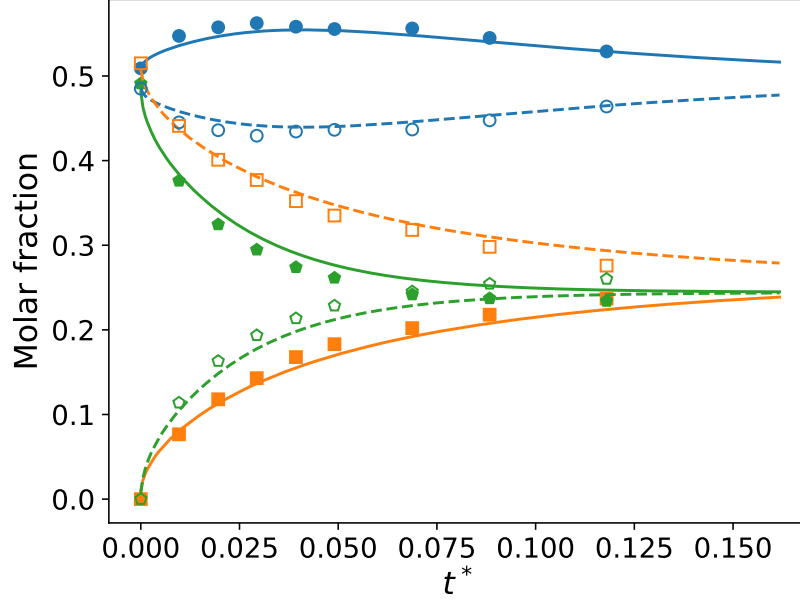


Figure 7.6 – Comparison between simulation (lines) and experimental data (symbols) extracted from Ref. [68]. Molar fraction of argon, blue; molar fraction of methane, orange; molar fraction of hydrogen, green. Solid lines and filled symbols, left tube; dashed lines and unfilled symbols, right tube.

7.4 D- Opposed jets flow

The model is finally validated for a flow whose dynamics is dominated by a convection-diffusion competing mechanism. The test case that we investigate is the same proposed in Ref. [51], which consists of two opposed jets of quaternary mixtures of gases having different initial concentrations (see Fig. 7.7 and Table 7.3). The domain size is $(n_x, n_y) = (200, 400)$ and the widths of the left and right incoming streams are the same and equal to $0.4n_y$. At left and right boundaries, equilibrium is assumed for the distribution functions, and the velocity is set equal to zero. For the left and right incoming streams, we assume that all species velocities are respectively equal to $U_L = U_0$ and $U_R = -0.936U_0$ (as inferred from Fig. 3 of Ref. [51]), and we chose $U_0 = 0.04$. At the top and bottom boundaries, the outer incoming distribution functions are extrapolated from the interior. The transport coefficients are evaluated by means of Eqs (6.40-6.43) at atmospheric pressure and temperature $T = 300\text{K}$. The species kinetic constants needed to evaluate the Ω -integrals are given in Table 7.4.

Figure 7.8 shows the distributions of the molar fractions and the mixture mass ve-

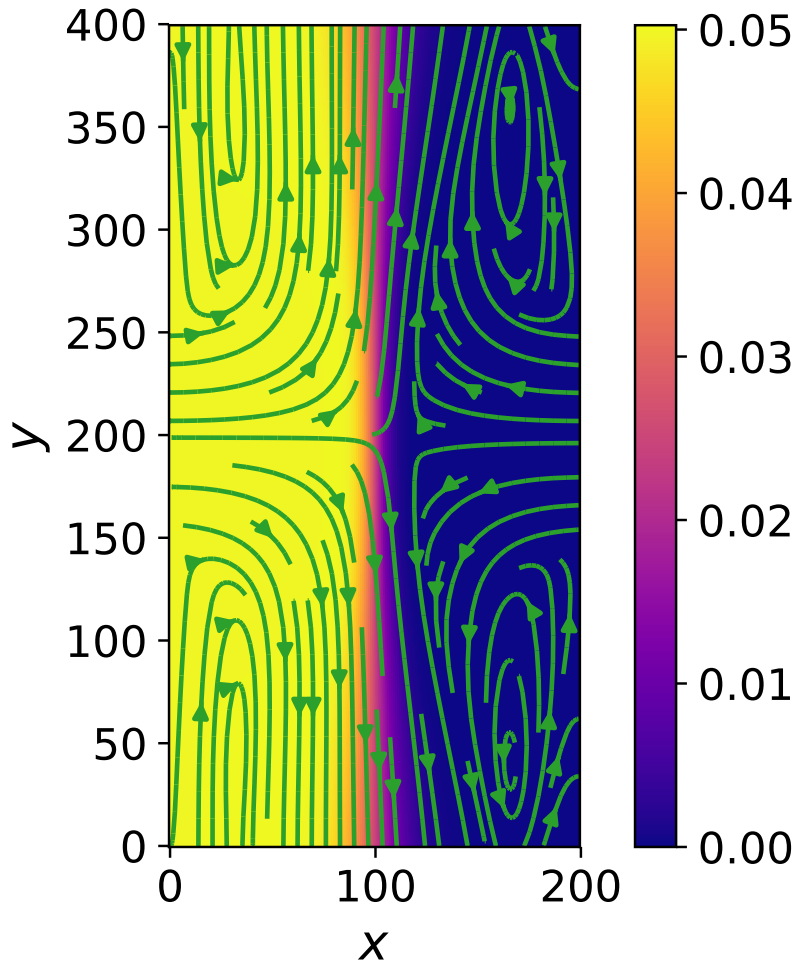


Figure 7.7 – Molar fraction and velocity streamline plot of H_2O .

locity at the symmetry plane ($y = n_y/2$) and at steady state. The results are in close agreement with Ref. [51] where the *CHEMKIN* package is used to calculate the transport coefficients and mixture-averaged diffusion coefficients are employed for each species. This is however only correct asymptotically when there is either only one bulk component and trace species, or when all species but one have nearly the same diffusion velocities, or when all the diffusion coefficients are the same. Despite using a simplifying mixture-average diffusion, the results are similar since the multi-components diffusion effects, which can not be captured with this assumption, are not significant. In addition, these transitory complex diffusion phenomena as in the case of the Loschmidt's tube experiment (Sec. 7.3) would not be visible on this steady state comparison. Figure 7.8 confirms that our model correctly predicts the dynamics of the flow characterized by a competing convection-diffusion mechanism.

stream	x_{H_2}	x_{N_2}	x_{O_2}	x_{H_2O}
left	0.10	$0.85 - \delta$	$0 + \delta$	0.05
right	$0 + \delta$	$0.9 - 2\delta$	0.10	$0 + \delta$

Table 7.3 – Initial molar fractions, in our simulation we take $\delta = 10^{-5}$ (in the experiment, $\delta = 0$).

m		H_2	N_2	O_2	H_2O
M_m	[g/mol]	2.01588	28.0134	31.9988	18.0153
ϵ_m/k_B	[K]	36.7	47.6	113.	775.
σ_m	[nm]	0.2959	0.385	0.433	0.252

Table 7.4 – Kinetic constants from Ref. [1].

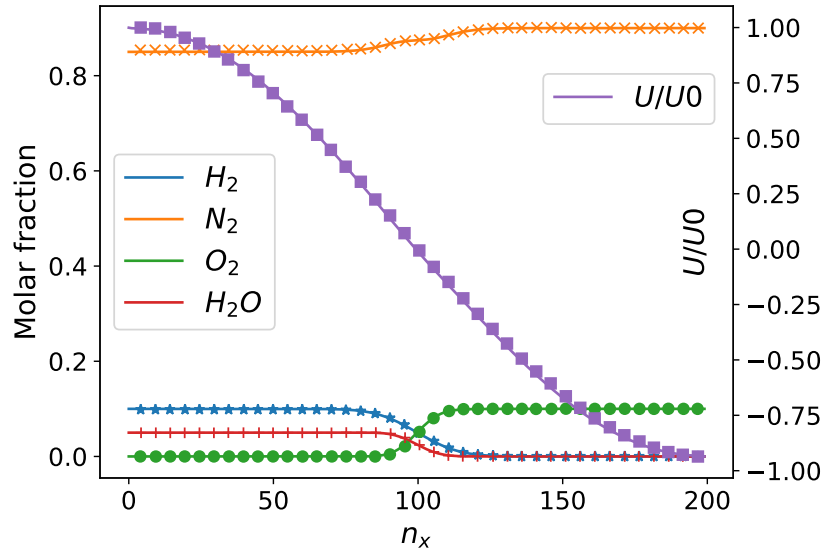


Figure 7.8 – Comparison between the present method (line) and LBM from Ref. [51] (symbols) at $y = n_y/2$.

Chapter 8

Synthesis

In the present chapter, we derive, explain and validate a lattice Boltzmann model for miscible gases. We show that the mixing dynamics of multi-species mixtures can be simulated by a forcing term in the lattice Boltzmann algorithm [Eq. (5.7)] and the addition of a body force to account for species having different molecular masses [Eq. (5.13)]. Furthermore, the model also relies on the use of transport coefficients that are calculated by an approximation of the relations obtained from kinetic theory [Eq. (6.40)].

The model is validated against analytical, experimental, and numerical results available in the literature. We have shown that the model can accurately simulate the decay of a density wave for a variety of pseudo speed of sound corresponding to molar mass ratios up to 86. The model adequately predicts the diffusion process in binary and ternary mixtures of gases as shown in the case of the equimolar counter-diffusion and Loschmidt's tube experiment. Complex diffusion phenomena such as reverse diffusion occur in ternary mixtures. These phenomena are well observed in our model, and the dynamics predicted by the Maxwell-Stefan equations is correctly recovered. The present model also adequately predicts the dynamics of flows where convection and diffusion compete as in the case of two opposed jets of mixtures.

Finally, one of the advantages of the forcing approach is the easiness of implementation. Since the collision is not altered, the method that we propose can easily be introduced in any other lattice Boltzmann algorithm in order to take into account complex diffusion among species. Upcoming applications of the present model focus on instabilities resulting from the transient mixing dynamics in porous media.

Part III

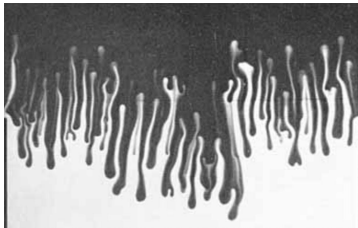
Simulation of the viscous fingering by the lattice Boltzmann method

9	Viscous fingering instability	89
10	Porous medium in LBM	93
10.1	Gray lattice Boltzmann	93
10.2	Brinkman drag force	94
11	Numerical simulations	95
11.1	Darcy's law	95
11.2	Viscous fingering	95
11.3	Viscous fingering caused by reverse diffusion	106
12	Synthesis	111

Chapter 9

Viscous fingering instability

Fluid flows and mixing in porous media play a key role in number of real-world engineering problems such as in chromatographic columns, in secondary and tertiary oil recovery, in carbon dioxide sequestration, and in micro-fluidic devices. Interfacial instabilities can be detrimental for the previous processes or on the contrary a way to improve the mixing. High Reynolds number flows can be actively stirred by turbulence but other mechanisms are needed in a porous medium. The generation of an interfacial instability is one mechanism among others that can improve the mixing. This instability can be driven by chemical reactions, density stratification (Rayleigh-Taylor instability), or difference in viscosity. Here, we focus on the latter, which is called viscous fingering or Saffman-Taylor instability. This interfacial instability occurs when a less viscous fluid displaces a more viscous fluid in a porous medium [69]. Finger-like patterns as shown in Fig. 9.1 emerge and grow, exhibiting complex dynamics. The influence of the instability should not be underestimated. Using data from a CO_2 sequestration project, the mixing zone after a shutdown time of approximately 150 years is estimated around 50 km long whereas if only pure diffusion is considered, the mixing zone would be roughly 5m [70].



(a) Viscous fingering in a gravity driven miscible displacement in a Hele-Shaw cell.



(b) Viscous fingering in an opaque medium visualized by X-ray absorption.

Figure 9.1 – Pictures from reference [69], with permission.

Porous media, such as natural soils or sedimentary rocks, are incredibly difficult to model due to the heterogeneous structure and composition of the pores at many different scales. Since they are opaque, most experimental investigations of the viscous fingering

phenomena are carried out on Hele-Shaw cells. A Hele-Shaw cell is composed of two parallel plates with a small gap. This flow configuration mimics the drag induced by a porous medium when the gap is small enough. From a numerical point of view, the simulation of a large-scale flow at the pore scale is often impractical because of long CPU time and excessive memory consumption. Hence, a volume average approach is usually used to overcome these difficulties. In this case, Darcy or Darcy-Brinkman semi-empirical equations are solved and porosity, permeability, and other measurements are defined. In the case of a single fluid, the Brinkman equation adds a drag force to the Stokes equations,

$$\nabla p = -\frac{\mu}{K}\mathbf{u} + \nabla \cdot \left[\mu_e \left(\nabla \mathbf{u} + (\nabla \mathbf{u})^T \right) \right] \quad (9.1)$$

where p is the pressure, K is the permeability of the medium, \mathbf{u} is the fluid velocity, and μ_e is the effective viscosity which may not be equal to the fluid viscosity. The Brinkman equations are a convenient transition model between Darcy regime ($K \ll L^2\mu/\mu_e$, with L the macroscopic characteristic length) and Stokes regimes ($K \gg L^2\mu/\mu_e$). In a Hele-Shaw cell, one can show that the flow is also governed by Darcy's law with an equivalent permeability of $b^2/12$ in the limit of low Reynolds number flow and $b/L \rightarrow 0$, where b is the small gap width. It is to be noted that the dynamics of the viscous fingering is mainly governed by the Darcy equation [69] therefore Stokes' term is not of primary importance and the effective viscosity is taken equal to the fluid viscosity unless otherwise stated. Indeed, most of the literature (see previous and next references) only considers Darcy's equations. The latter equations correctly described flows in Hele-Shaw cells and in simple porous media whereas Darcy-Brinkman's equations are often used as a transition model between porous flow and Stokes flow such as in the case of fractured porous media.

Now we consider a homogeneous porous medium and a zone where the viscosity varies greatly. Under suitable assumptions, the flow follows a one-dimensional Darcy's law and the pressure differential from both sides of the fictional interface as a result of a virtual displacement δx reads

$$\delta p = (p_{left} - p_{right}) = (\mu_{right} - \mu_{left})U/K\delta x \quad (9.2)$$

If the net total pressure δp is positive, then any small displacement will amplify, resulting in an instability. From this simple argument, the instability mechanism is driven by the viscosity difference on either side of the interface. If the displaced fluid is more viscous than the displacing ($\mu_{right} > \mu_{left}$) then the configuration is unstable, in the contrary ($\mu_{right} < \mu_{left}$) any small interface perturbation will be damped and the configuration is stable.

Since the pioneer work of Hill [71] in 1952 and Saffman and Taylor [72] in 1958, extensive investigations have been performed on both immiscible and miscible fluids. A distinctive characteristic of miscible fluids is the lack of a sharp interface and surface tension. Mixing produces changes in the fluid since the properties of the mixture vary continuously while diffusion occurs. Usually, the viscous fingering is modeled by using Darcy's law and a scalar transport equation for the concentration. A relation between the viscosity and the concentration of the components must be defined. Most articles

follow the standard literature rather than physical rigor and assume an exponential dependence.

Studies of the viscous fingering instability can be divided into two categories: linear stability analyses and non-linear simulations. The linear stability analysis is a classical tool to study the evolution of small perturbations that leads to the instability. The main mathematical challenge of the miscible viscous fingering is due to the unsteady base (i.e. unperturbed) state caused by diffusion. In practice, the quasi-steady-state approximation is employed and the linear stability analysis is applied on a frozen base state at successive frozen times [73, 74]. Other methods such as initial value problem or non-modal analysis (transient growth analysis) are possible. Excluding very short times, the different approaches are in good agreement [73, 75]. As its name implies, the linear stability analysis is restricted to early times. As the perturbation develops, non-linear interactions occur and the linearized equations are no longer valid. This leads to the second category: non-linear simulations where no approximation is made, thus the full life cycle of fingers, from onset to shutdown, can be studied. In this case, equations are solved with a stream-function formulation using spectral method [73, 74, 76, 77] or finite-difference method [78, 70]. The former is very efficient whereas the latter can be numerically stable for any viscosity ratios.

Lattice Boltzmann method was also used to study the viscous fingering phenomenon. In 1992, Holme and Rothman [79] propose a LBM for miscible binary fluids where one distribution function models an advection-diffusion equation and a second distribution function is employed for the mixture density and momentum balance equations. Then, they simulate the viscous fingering instability using their miscible model with a variable mixture viscosity and a drag force that mimics the effect of a porous medium. With a similar miscible LBM approach, Rokotomalala, Salin, and Watzky [80] study the miscible displacement of two fluids with different viscosities between two parallel plates. In the absence of porous medium, a single finger may appear depending on the diffusion and the viscosity contrast. This can be seen as a limit case of the viscous fingering instability. Contrary to the previous model where an advection-diffusion equation for the concentration is solved, a more natural approach in order to deal with diffusion in the frame of the lattice Boltzmann method is the use of an inter-molecular friction force. Indeed, the distribution function for the diffusion equation lost its molecular meaning and is no longer associated with the physical description of a species, i.e., collisions of molecules. More specifically, the diffusion equation is postulated and a kinetic scheme is tailored so as to solve it. Here, neither transport equation for the concentration, nor Darcy equation with exponential viscosity dependency are solved. Each species dynamic is governed by its own kinetic equation [Eq. (5.1)] where diffusion is taken into account by means of an inter-molecular force and the viscosity of species stemmed from the kinetic theory of gases [Eq. (6.40)]. Adopting a lattice Boltzmann approach, we investigate two strategies to mimic the porous medium effects: the gray lattice Boltzmann model assuming a partial reflection condition and the Brinkman force model adding a drag force.

Viscous fingering is a fascinating and a pertinent phenomenon to showcase the possi-

bilities of our miscible model. This instability exhibits complex dynamics depending on both molecular diffusion and viscosity namely inter-molecular friction forces and partial viscosities in our case. A few questions arise. Can we simulate the viscous fingering instability with the present model? What is the influence of the viscosity law? How the instability is modified when multi-component effects take place in ternary mixtures?

Chapter 10

Porous medium in the lattice Boltzmann method

In this chapter, we briefly present how to model the porous medium within a lattice Boltzmann framework. As described earlier, we seek for an average view of the porous medium and the equivalent target macroscopic equation is Darcy (-Brinkman) 's equation.

10.1 Gray lattice Boltzmann

Taking the advantage of the mesoscopic view of the lattice Boltzmann method, a porous medium can be modeled by different means. We first present the so-called gray lattice Boltzmann (GLBM) scheme where a special condition is applied on the whole domain: in each cell during the streaming step, the distribution functions are bounced back with a certain amount. Various schemes are proposed in the literature. In Ref. [81], the local pre-collision distribution functions are reflected whereas in Ref. [82], the local post-collision distribution functions are taken as reflected distribution functions. Yoshida and Hayashi [83] also suggest a gray lattice Boltzmann model based on Ref. [84] but the neighboring post-collision distribution functions are reflected. Despite some differences, all the previous gray lattice Boltzmann schemes [81, 82, 83] recover the Darcy-Brinkman equation [85]. In this study, the use of the model proposed in Ref. [83] is motivated by two main reasons. First, a redefinition of the macroscopic velocity is not required in this latter scheme. This redefinition would lead to complicated expressions especially on the boundary nodes since in the present approach, velocity and forces are coupled [Eqs. (5.6-5.7)]. Furthermore, the classical bounce-back boundary condition is obtained as a limit expression. If we use the notation Γ_α^m to substitute for the right-hand side of Eq. (5.1) (post-collision part), the following gray lattice Boltzmann scheme is obtained,

$$f_\alpha^m(\mathbf{x} + \mathbf{e}_\alpha \delta_t, t + \delta_t) = (1 - \theta_m) \Gamma_\alpha^m(\mathbf{x}, t) + \theta_m \Gamma_\alpha^m(\mathbf{x} + \mathbf{e}_\alpha \delta_t, t), \quad (10.1)$$

where $\Gamma_{\alpha}^m(\mathbf{x} + \mathbf{e}_{\alpha}\delta t, t)$ are the post-collision distribution functions from the opposite direction of α velocity located at the neighboring node and θ_m is the amount of reflection. The principle of the algorithm is depicted in Fig. 10.1

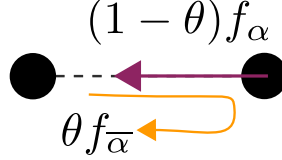


Figure 10.1 – Sketch of the gray lattice Boltzmann algorithm. The resulting streaming step in GLBM is composed of a fraction of the standard propagated distribution function and a reflected part from the opposite lattice direction.

When $\theta_m = 0$, the usual streaming step occurs and $\theta_m = 1$ is similar to the classical bounce-back (no-slip) condition. For $0 < \theta_m < 1$, the scheme mimics the dynamics of a porous medium and this approach should be related to a subgrid model for porous medium. The parameter θ_m depends on the viscosity of the fluid and the permeability of the considered porous medium and the following relation can be obtained [83, 85]

$$\frac{\mu_m}{K\rho_m} = \frac{2\theta_m}{(1 - \theta_m)\delta t} \quad (10.2)$$

Here, θ is defined on the link between nodes instead of being a node based value. In each direction α of the lattice, θ is computed by the means of an interpolation between the two nodes. This ensures that the mass is conserved strictly by the scheme.

10.2 Brinkman drag force

In the second approach, referred as Brinkman force (BF) model, the porous medium resistance is included explicitly through a drag force in the lattice Boltzmann equation, e.g. [80, 86, 87, 88, 89, 90]. Here, we follow a similar approach and the forcing term is written as

$$\mathcal{F}_{porous,m} = -\frac{\mu_m}{K}\mathbf{u}_m. \quad (10.3)$$

Compared to the gray lattice Boltzmann, this strategy is local and has a negligible computational cost since we already implement a source term because of the intermolecular friction forces. As mentioned in Refs.[23, 24, 91], the numerical permeability depends lightly on the viscosity for both Brinkman force and gray lattice Boltzmann models. This nonphysical variation can be alleviated by keeping the so-called magic number Λ constant (see [22, 23, 24, 86, 91]). We use the multiple relaxation times (MRT) collision model with $\Lambda = 3/16$ corresponding to $s_q = 8\frac{2-1/\tau_m}{8-1/\tau_m}$.

Chapter 11

Numerical simulations

11.1 Darcy's law

In order to show that Darcy's law is recovered by both of the proposed schemes, a flow composed of two identical species ($m = 1, 2$ and $\beta_m = 1$) through a homogeneous porous medium is simulated. Domain size is set to ($n_x = 101$, $n_y = 20$). Periodic conditions are applied on top and bottom of the domain and a constant velocity profile ($u_{x,m} = U$, $u_{y,m} = 0$) is imposed at left and right side of the domain via the non-equilibrium bounce-back. Distribution functions are initialized at their equilibrium values with an uniform initial density field $\rho_1 = \rho_2$. Simulation is stopped when steady state is achieved. In Figure 11.1, the pressure drop between the left and right side of the domain is plotted against the horizontal inlet velocity. Both gray lattice Boltzmann and Brinkman force models give equivalent results and show the expected Darcy behavior of the simulated system.

This first result shows that both porous modeling strategies are able to accurately reproduce the standard behaviour of a porous medium for different values of K .

11.2 Viscous fingering

The viscous fingering instability occurs when a less viscous fluid invade a more viscous fluid. In the case of miscible fluids, if the interface between fluids is sharp enough, finger-like patterns emerge and grow, exhibiting complex dynamics. Following the literature, dimensionless parameters are defined such as the log-viscosity ratio, the Péclet number (ratio of the advective transport rate and the diffusive transport rate), and the Darcy number:

$$R = \ln \left(\frac{\mu_{0,2}}{\mu_{0,1}} \right), \quad \text{Pe} = \frac{UL_{ref}}{\mathcal{D}_{12}}, \quad \text{Da} = \frac{K}{L_{ref}^2}, \quad (11.1)$$

where U is the injected velocity and L_{ref} is the reference length. Here following Ref. [74], the characteristic scales are based on the convective length: L_{ref} is taken as the height of the domain and the reference time is $t_{ref} = L_{ref}/U$. If $R < 0$, the invading fluid is more

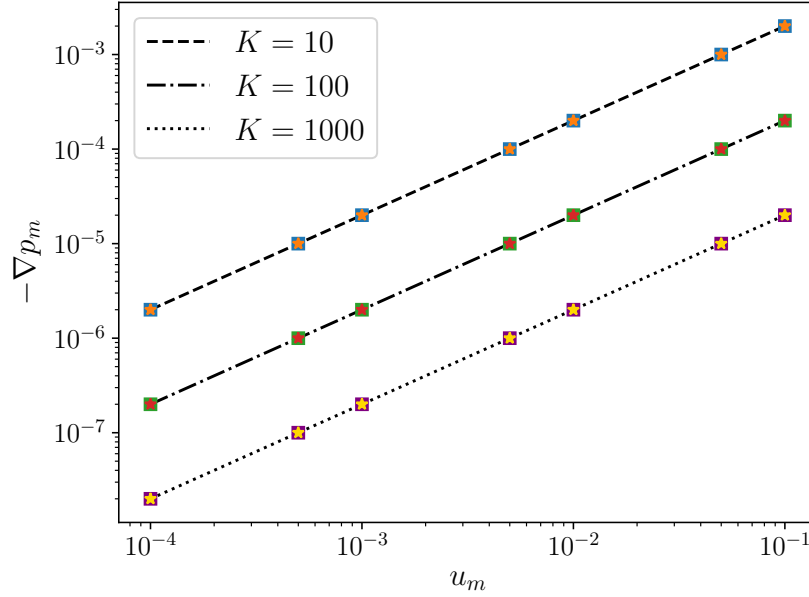


Figure 11.1 – Pressure drop according to the velocity for different permeability at fixed viscosity $\mu_{0,m} = 2 \times 10^{-1}$ lu. Values are given in lattice units (lu). Squares and stars stand for numerical results obtained respectively with the gray lattice Boltzmann and the Brinkman force schemes. Lines are the analytical solution $-\nabla p_m = \mu_m/KU$.

viscous than the resting fluid, and the interface is always stable. On the other hand, if $R > 0$, the invading fluid is less viscous than the resting fluid, and the interface between the two fluids may be unstable. The number of fingers increases with both the Péclet number and the ratio R . We recall that the relation between the pure viscosity and the species is given by Eq. (6.40). The influence of different parameters on the instability is studied. First, we present the numerical configuration employed to simulate the viscous fingering instability. The early times of the instability are compared with results from linear stability analysis and for intermediate times, we focus the evolution of the mixing length induced by the fingering. Effects of the Péclet number, and the porous model (gray lattice Boltzmann or Brinkman force models) are highlighted.

11.2.1 Numerical configuration

In the following simulations, the fluid consists of two species having equal molar masses ($\beta_m = 1$ $m = 1, 2$). The resting mixture is composed of molar fractions $x_1 = 0.1$ and $x_2 = 0.9$ and these are swapped for the injected mixture ($x_1 = 0.9$, $x_2 = 0.1$). The domain considered is two-dimensional and we impose periodicity at the top and bottom boundaries. At the left and right boundaries, a constant velocity condition equal to U is applied for both species. Each simulation is initialized by an almost sharp interface

with a small perturbation so as to trigger the instability,

$$x_1(x, y, t = 0) = 0.9 + (0.1 - 0.9) \left[0.5 + 0.5 \times \operatorname{erf} \left(\frac{x - 0.1}{\sqrt{t_0}} \right) + r(y) \times \exp \left(\frac{-(x - 0.1)^2}{t_0} \right) \right], \quad (11.2)$$

$$x_2(x, y, t = 0) = 1 - x_1(x, y, t = 0), \quad (11.3)$$

where the function r returns a random number which is uniformly distributed in the interval $[0, 10^{-5}]$, and the same seed is used for the pseudo-random generator in each simulation. We set $t_0 = 10^{-6}$ to avoid strong gradients. The initial total pressure is computed from Darcy's law for the mixture

$$p(x, y, t = 0) = p_{ref} + (1 - x) \frac{\mu_1(x) + \mu_2(x)}{K} U, \quad (11.4)$$

with $p_{ref} = 1$ lu, and the distribution functions are initialized at their equilibrium values plus the first order deviation from Eq. (2.91). A sketch of the numerical configuration is displayed in Fig. 11.2.

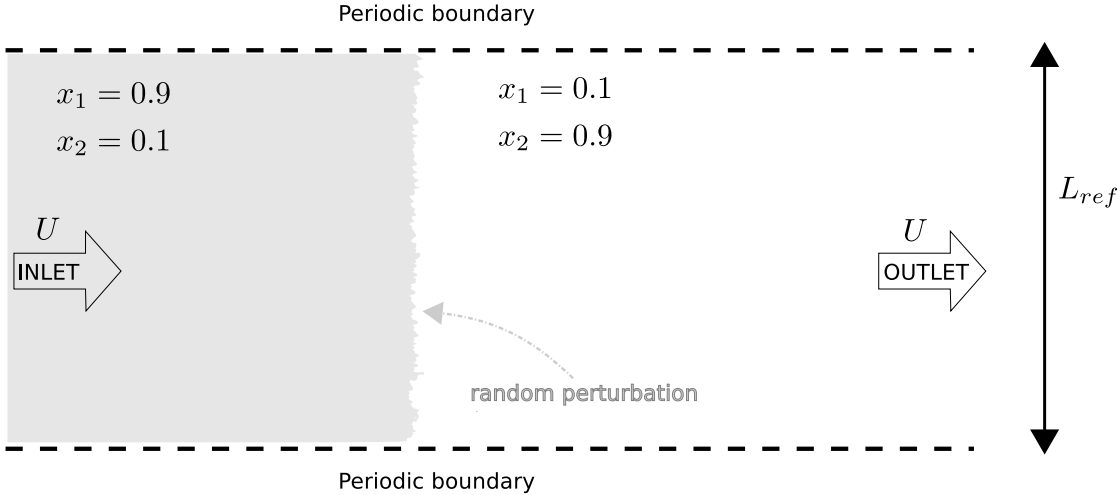


Figure 11.2 – Sketch of the initial configuration and boundary conditions.

The viscous fingering instability is of course three-dimensional. However, according to Homsy and Zimmerman [76], the non-linear mechanisms found in two-dimensional persist in three dimensions and for long times the evolution of the fingers remains unchanged from two dimensions (see also Ref. [77]). This suggests that two-dimensional simulations are sufficient to capture much of the essential physical features of viscous fingering. We also make a few additional assumptions. The porous medium is assumed to be isotropic and the permeability is given by a scalar value. Viscous fingering in anisotropic media is studied by means of a linear stability analysis for instance in Ref. [92]. The flow is

more stabilized when the ratio of longitudinal to transverse anisotropic permeability is increased. Similarly, we only consider molecular diffusion and do not take into account the (anisotropic) dispersion caused in the flow at the pore scale since a general Taylor dispersion model is not known. One can note that the previous authors find from the linear stability analysis that the flow is more stable when the ratio of longitudinal to transverse anisotropic dispersion is decreased. With these assumptions, we will be able to compare our results with the classical literature.

A fine spatial discretization is required in order to resolve accurately all the length scales of the instability, especially at high Péclet numbers. Preliminary simulations are performed to find the appropriate grid spacing. Three square grids are considered with different resolutions corresponding to $n_y = 1000, 2000, 4000$ where L_{ref} is kept constant. The initial random perturbation is based on the grid where $n_y = 1000$ and interpolations are used for higher resolutions. Otherwise stated, we set

$$R = 3 (\mu_{0,2} \approx 20\mu_{0,1}), \quad \text{Pe} = 5000, \quad \text{Da} = 6.25 \times 10^{-8}, \quad (11.5)$$

$$\text{Re}_{0,1} = \frac{UL_{ref}\rho_{ref}}{\mu_{0,1}} = 10, \quad \text{Ma} = \frac{U}{c_s} = \sqrt{3} \times 10^{-3}. \quad (11.6)$$

With this specific value of Mach number, the inlet velocity is equal to 10^{-3} lu. This corresponds to a low Reynolds flow in the Darcy regime at moderate Péclet number and viscosity ratio. We recall that two different system of units are defined. On one hand there is the lattice unit system where the time and space step are equal to one, and on the other hand the physical system. Nonetheless, all the dimensionless numbers are equal for either system of units.

For each resolution at different times, we carry out a fast Fourier transform (FFT) of the fingers. In particular, we take a slice of the domain where the mean molar fraction along the transverse direction is included in the interval $[0.11, 0.89]$. Afterwards, we average along the longitudinal direction and apply a FFT to obtain the spectrum of the interface deformation according to the y-axis spatial frequency as plotted in Fig.11.3. Results for different resolutions are compared at the same non-dimensional time

$$t^* = \frac{t}{t_{ref}} = \frac{tU}{L_{ref}}. \quad (11.7)$$

For short times, the lowest resolution corresponding to $n_y = 1000$ is not able to resolve the high frequencies of the instability. As the time progresses, larger structures appear and are captured by three resolutions, but for $n_y = 1000$ the amplitude of the fingers is slightly over-predicted. Resolutions corresponding to $n_y = 2000$ and $n_y = 4000$ give equivalent results suggested that the main length scales of the instability are sufficiently well resolved. Nonetheless, we point out that global quantities such as the mean molar fraction or the mixing length are less sensitive to the resolution and can be adequately captured even with a very coarse grid. Theses results are in agreement with the linear stability analysis of a steep initial profile made in Ref. [74]. At initial time $t = 0$, an analytical dispersion curve can be obtained and the cutoff wave number is found equal to $RPe/4 = 3750$ corresponding to a wave length of 0.0016. With a

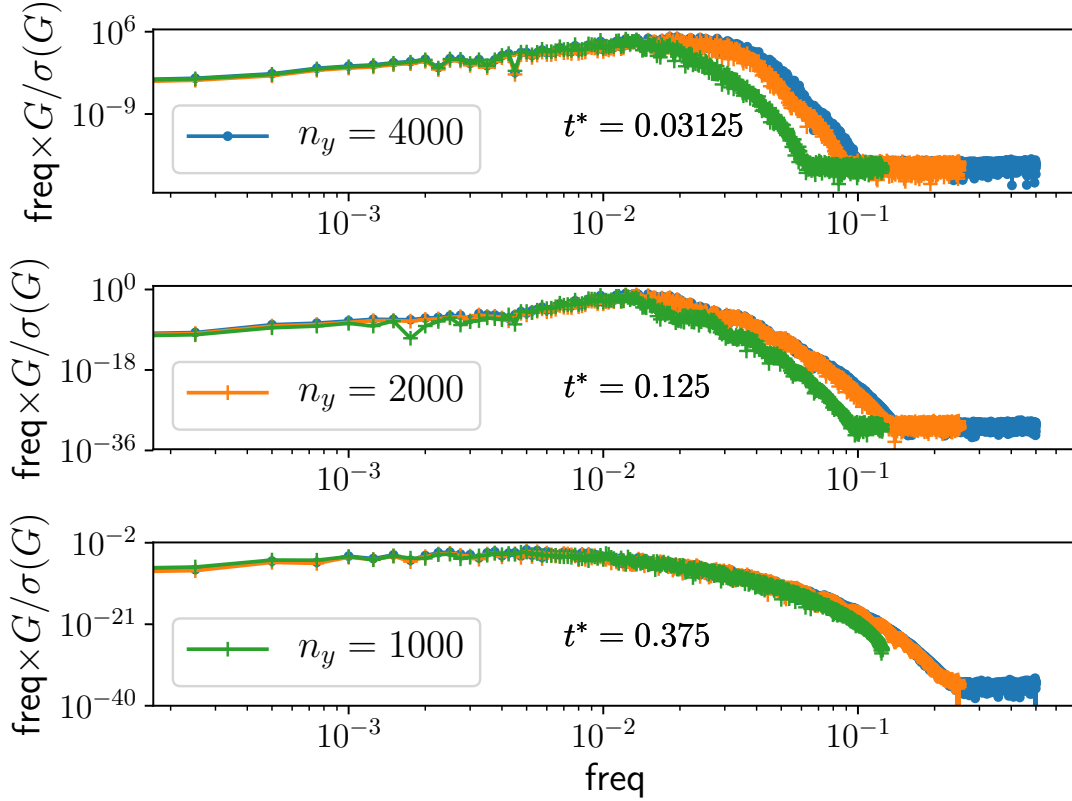


Figure 11.3 – Power spectral density at different times t^* for different resolutions equivalent to blue, $n_y = 4000$; orange, $n_y = 2000$; green, $n_y = 1000$. $G = \hat{x}\hat{x}^\dagger$ where \hat{x}^\dagger is the conjugate of the Fourier coefficients \hat{x} . G is normalized by its variance: $\sigma(G)$.

resolution of 0.001, the grid $n_y = 1000$ is inadequate for the present Péclet number. We will use mainly two resolutions corresponding to $n_y = 4000$ in order to accurately capture all the small scales at early times and a lower resolution equivalent to $n_y = 2000$ for simulations dedicated to intermediate times so as to reduce the computational cost. Indeed, since the instability is convected at the injected velocity, a longer domain is needed to observe the development of the instability. Unfortunately, a formulation of the lattice Boltzmann scheme in the reference frame moving with the velocity of the injected fluid is not trivial and requires the use of rectangular lattices which are beyond the scope of this work (see for instance Refs. [93, 94, 95]).

The study will be divided into two parts: early times and intermediate times. For early times, we will compare our results with the literature where the concentration goes down to zero. With the present model this is not possible since a tangible amount of species has to be modeled. The molar fractions of the invading mixture are therefore set to $x_1 = 0.999$, $x_2 = 0.001$ and swap for the displaced mixture. For intermediate times, molar fractions 0.9 and 0.1 are sufficient to obtain the global behavior of the instability

with a coarse grid.

11.2.2 Early times

At early times, the interface between the two mixtures spreads because of diffusion and start to deform. At the very beginning, the flow is linearly unstable and perturbations grow exponentially. The onset of fingers is explored by many authors using linear stability analysis [69, 73, 74, 75, 70, 92]. The Darcy's equation, the continuity equation, and the transport equation for the concentration are linearized and a dispersion equation is solved so as to compute the growth rate of the perturbation. An analytical solution is only known for the initial time and numerical methods have then to be employed. Linear stability analysis can also be directly performed in the lattice Boltzmann framework (see. [96, 97]) however this approach is still in its infancy and is only applied to simple single fluid flows. In this study we carry out non-linear simulations with the aforementioned lattice Boltzmann model and compute the growth rate of the perturbation *a posteriori*. This present approach has the advantage to avoid the development of another tool and is valid for the whole instability including the non-linear stage. The molar fractions can be decomposed into a base state x_m^0 and a perturbative component x'_m ,

$$x_m(\mathbf{x}, t) = x_m^0(\mathbf{x}, t) + x'_m(\mathbf{x}, t). \quad (11.8)$$

We assume that the perturbation can be expressed in the form of

$$x'_m(\mathbf{x}, t) = x'_m(\mathbf{x}) \exp(\sigma t) \quad (11.9)$$

where σ is the growth rate of the perturbation. The dispersion curves are obtained by applying a fast Fourier transform (FFT):

$$x'_m(\mathbf{x}, t) = x_m^0(\mathbf{x}, t) - x_m(\mathbf{x}, t) \quad (11.10)$$

$$\hat{x}(x, k, t) = \text{FFT}_y(x'_m(\mathbf{x}, t)) \quad (11.11)$$

$$a(k, t) = \|\hat{x}(x, k, t)\|_2 = \sqrt{\int \hat{x} \cdot \hat{x}^\dagger dx} \quad (11.12)$$

$$\sigma(k, t) = \frac{d \ln(a(k, t))}{dt} \quad (11.13)$$

where \hat{x}^\dagger is the complex conjugate of \hat{x} , k is the wave number and we choose a time step sufficiently small such as the growth rate can be considered as constant between two derivation steps. a represents a measure in the Fourier space of the amplification of the perturbed molar fraction. Only relevant growth rates are of interest, consequently the growth rate of perturbations whose amplitude is less than $10^{-4} \times \max_{\forall k}(a(k, t))$ is filtered out. The perturbative components are computed by subtracting the components from the non-linear perturbed solution to the components from the base state. This base state is obtained by simulating the exact same conditions with no initial perturbation.

No finger emerges in this case. Therefore two simulations with and without initial perturbations are performed for each case studied.

First, we compare in Fig. 11.4 the results obtained from the gray lattice Boltzmann and the Brinkman force models. Both approaches lead to equivalent growth rates. Thus, at early times, the linearly development of the instability is well captured by the two models. The growth rate decreases in time. The most dangerous wave number (k_{max}) corresponding to the largest growth rate as well as the threshold (first wave number at which $\sigma = 0$) and the cutoff (k_c) (last wave number at which $\sigma = 0$) wave numbers are reduced as the instability progresses resulting in widening fingers. The rest of the simulations are performed with the Brinkman force model otherwise stated.

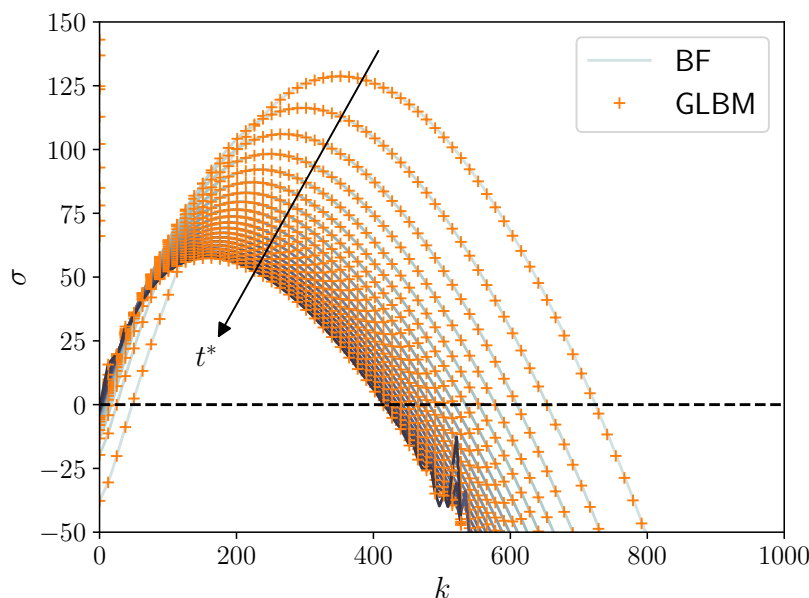


Figure 11.4 – Dispersion curve for $Pe = 2000$ at various times from $t^* = 0.005$ to $t^* = 0.1$ with a times step $\Delta t^* = 0.05$. Lines and symbols stand for the Brinkman force model and gray lattice Boltzmann. The color gradient of the lines denotes the time evolution. ($n_x = 4000$, $n_y = 4000$).

In figure 11.5, the growth rate for different Péclet numbers at $t^* = 0.01$ and $t^* = 0.1$ is compared with the results from Ref. [74] where a linear stability analysis using a self-similar quasi-steady-state-approximation is employed. A close overall agreement is found for the different Péclet numbers. The discrepancies between linear stability analysis and non-linear simulations are more pronounced at early times ($t^* = 0.001$) as already pointed out by refs. [73, 75]. The previous authors mention that, for short times, inverse value problem and non-modal analysis are closer to non-linear simulations results. As expected, excellent agreement is found at latter times ($t^* = 0.1$) for $Pe < 5000$. For $Pe = 5000$, non-linear interactions occur and the perturbation can no longer be described by Eq. (11.9). Note that the linear description of instability could be still valid at the

time $t^* = 0.1$ if the flow is initially perturbed by only one wave number instead of being excited on the whole spectrum. This more accurate strategy required to run a simulation (two precisely for the perturbed and non-perturbed cases) for each wave number of interest. This becomes rapidly unpractical if one wants to study the time evolution of the instability as the relevant wave numbers where $\sigma > 0$ depends on time and shift toward smaller wave numbers as time progresses.

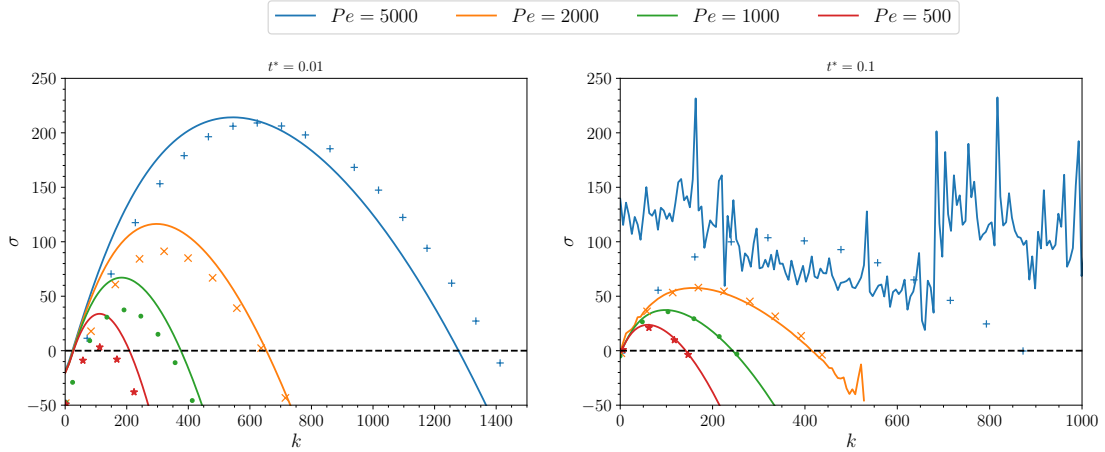


Figure 11.5 – Dispersion curves for $R = 3$ at $t^* = 0.01, 0.1$ with different Péclet values. Lines stand for the simulation and the symbols are data obtained by a linear stability analysis from Ref. [74]. ($n_x = 4000, n_y = 4000$).

Diffusion acts as a stabilization factor by smoothing perturbations and heading to an homogeneous mixture. Hence, as shown in Fig. 11.5, the instability is more dominant at higher Péclet numbers. A lower fluid dispersion expands the range of unstable wave numbers and increases the growth rate. The cutoff wave number increases with the Péclet number whereas it has a very limited influence on the threshold wave number. This can be easily seen on neutral stability curves (contours of $\sigma = 0$) plotted in Fig. 11.6. The differences from the bell-shaped curve is due to the non-linear interactions. The area above the neutral curve defines the region of instability. As described earlier, this region increases with the Péclet number. The minimum (t_{crit}^*, k_{crit}) on the neutral curves is the limit below the perturbation is stable. It is interesting to note that we can also define a critical Péclet number Pe_{crit} and its value depends on the time. For $Pe = 500$ and $Pe = 1000$, the flow is initially stable then becomes unstable at latter times whereas for $Pe = 5000$ at $t^* = 0$ the flow seems already unstable. For very short times, the growth of the interface caused by large diffusion (low Péclet numbers) surpasses the exponential growth of the perturbation. This also implies that, as expected, there is a minimal critical Péclet number such as the flow is always stable when the diffusion is large enough. Nonetheless, more simulations with smaller time steps and various Péclet numbers should be performed to quantity this phenomenon and dismiss numerical transient artifacts especially for large Péclet numbers. The time variations of the most

dangerous wave number and respectively the cutoff wave number follows the same trend. In Appendix D.1, the most dangerous and the cutoff wave numbers are plotted in a logarithm scale according to the time and straight lines are obtained for $t^* > 0.01$. For a log viscosity ratio $R = 3$, the most dangerous wave number decreases rapidly then slower as $k_{max} \sim t^{*-0.26}$ compared to the cutoff wave number where $k_c \sim t^{*-0.36}$. We can also compute approximately the change with the Péclet number, $k_c \sim Pe^{0.59}$ and $k_{max} \sim Pe^{0.70}$. As seen in fig. 11.6, a higher Péclet number expands considerably the range of unstable wave numbers. High Péclet number flows are difficult to simulate because of limitations required on time and space resolutions if one wants to resolve all the length scales of the instability.

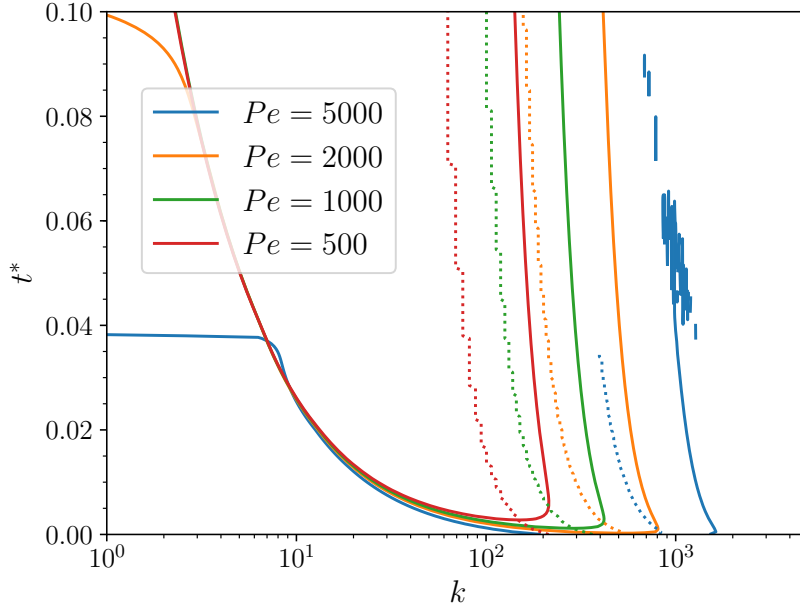


Figure 11.6 – Neutral stability curves ($\sigma = 0$) for different Péclet numbers at $R = 3$ according to the time and the wave number. Dashed lines represent the most dangerous wave number k_{max} . For $t^* > 0.035$ and $Pe = 5000$, non-linear interactions take place and the most dangerous wave number is not plotted. ($n_x = 4000$, $n_y = 4000$).

11.2.3 Intermediate times

Figure 11.7 shows a sequence of snapshots of a simulation performed with the Brinkman force model at $R = 3$, $Pe = 2000$. At early times ($t^* \leq 0.1$), the sharp interface diffuses and begins to deform. This stage is called the linearly unstable regime and linear stability analysis tools are suitable to describe the instability as shown previously. Many thin fingers develop and strong linear interactions take place as seen at $t^* = 0.46, 1.07, 3.05$. These can be identified as spreading, shielding, fading, and coalescence. By spreading, we refer to the process whereby one finger is slightly ahead of others. The finger grows

very quick and the gradient steepens between the finger and the surrounding more viscous fluid. The finger may then widen at the tip and shields the growth of the smaller neighboring fingers. Few thin fingers fade and diffuse in the ambient fluid resulting in a region of intermediate viscosity. Coalescence phenomenon describes the merging of two or more fingers together. This mechanism is fundamental since it is the merging of smaller fingers in the nearby dominant finger that keeps supplying the latter with less viscous fluid as we can see from the third snapshot of Fig. 11.7. The present dynamics of the simulation is rich displaying all major mechanisms. For higher Péclet numbers, the flow exhibits also more complex behaviors such as tip splitting, when a finger splits into two at the tip and side branching when a finger splits at its side [69, 70]. These fascinating interaction mechanisms lead globally to a coarsening of the fingers in the transverse direction and a growth of the fingers in the longitudinal direction. The number of fingers and the intensity of these interactions increase with the Péclet number and the log-viscosity ratio. Finally for $t^* > 3$, the few remaining fingers grows at constant rate. At very late time (not observed here, see the discussion in ref.[70]), the fingers should mix with the ambient fluid and are convected at a given speed close to the injected velocity. The length of the fingers should stay roughly the same since the interface is diffuse enough to smooth out the viscosity and concentration gradients.

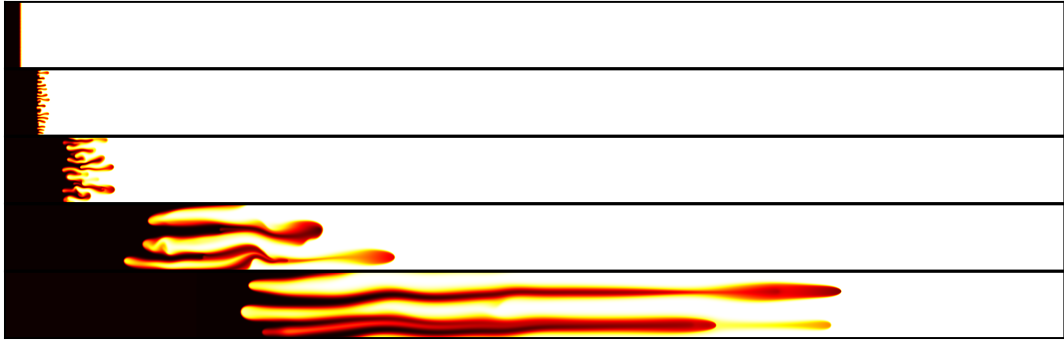
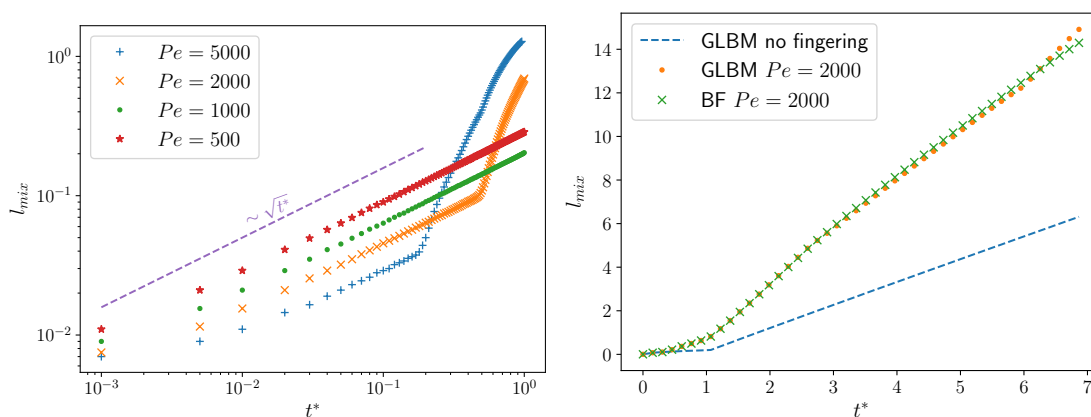


Figure 11.7 – Instability development for $R = 3$, $Pe = 2000$ at $t^* \approx 0.15, 0.46, 1.07, 3.05, 6.10$. The whole domain ($n_x = 8192$, $n_y = 512$) is plotted. The color-map (black-red-yellow-white) represents the variation of the molar fraction from $x_1 = 0.9$ to $x_1 = 0.1$. Same scaling is used for both x and y-axes.

A convenient way to describe the global dynamic is by observing the evolution of the mixing length, which is defined here as the distance where the transverse molar fraction is included between 0.89 and 0.11. In Figure 11.8a, the mixing length is represented in logarithmic scale according to t^* for various Péclet numbers at $R = 3$. Two different regimes are clearly visible. In the first regime, the diffusion dominates the growth of the mixing length, which is proportional to $\sqrt{t^*}$ as in the case of no viscosity contrast ($R = 0$, pure diffusion). Afterward, a transition regime may occur and depends on the Péclet number. The second regime can be seen in Fig. 11.8b. The mixing length

is represented in linear scale to better highlight the longtime behavior and the linear evolution of the fingers. The growth of the mixing length is linear in time suggesting that the advection now dominates. It is interesting to note that both regimes exist even when the initial molar fractions are not perturbed and no finger emerges. In this latter case, the development of the mixing length is reduced in the second regime. For instance in Fig. 11.8b, the approximate slope is 1 with no finger, whereas the slope is around 2.2 with fingering. Compared to the pure diffusive case, the mixing length is heavily affected by the viscous fingering instability. The two regimes are not specific to the viscous fingering but rather depends on the governing mechanism (diffusion or advection dominated). As the instability is more intense, the transition time decreases and the duration of this transition increases. During this transition, strong non-linear interactions occur as it can be seen in Fig. 11.7 at $t^* \approx 0.46, 1.07, 3.05$.

We would like to make a few remarks concerning the mixing length. This quantity is not appropriate if one wants to determine the time when fingers become visually perceptible. Actually, when the perturbations start to interfere non-linearly such as at $t \approx 0.1$ for $Pe = 2000$, the deformation of the interface is imperceptible. Fingers become noticeable later during the diffusion dominated regime. A better measurement of the visible onset of the fingers is given by a sudden growth of the interfacial length $I(t) = \iint [(\partial x_1 / \partial x)^2 + (\partial x_1 / \partial y)^2]^{\frac{1}{2}} dx dy$. In Appendix D.2, the contour map of the molar fraction x_1 at $t^* = 0.9$ is plotted for different Péclet numbers.



(a) Logarithm scaling for different Pe . ($n_x = 4000, n_y = 2000$). (b) Linear scaling at $Pe = 2000$. ($n_x = 8192, n_y = 512$).

Figure 11.8 – Temporal evolution of the mixing length at $R = 3$.

Finally, Fig. 11.8b shows no significant difference between the gray lattice Boltzmann and the Brinkman force model. The small deviation for $t^* > 6.5$ is probably due to the influence of the boundary condition close to the location of the fingers. Same dynamic results independently on how the porous media is modeled. Both gray lattice Boltzmann and the Brinkman force model adequately reproduce the viscous fingering instability although based on a fundamentally different formulation.

11.3 Viscous fingering caused by reverse diffusion

In the previous results, the relation between the viscosity and the concentration is given by Eq. (6.40) and not the exponential dependence usually found in the literature (see e.g. [69, 73, 74]). However, the calculated growth rates are in good agreement with Ref. [74] as shown in Fig. 11.5. This could be expected as for binary mixture Fick or Maxwell approach are equivalent and for species having the same molecular mass, the mixture viscosity $\mu_1 + \mu_2$ has a similar shape as $\mu_{0,2}e^{-Rx_1}$. For a binary mixture with species having different molecular masses, the variation of the mixture viscosity according to the mixture composition is more complex and can be non-monotonic: the maximum of the mixture viscosity can take place at intermediate molar fractions. The behavior of the instability is much more complex. A linear stability analysis shows that all non-monotonic viscosity profiles, irrespective of their end-point viscosities, become unstable [98]. This means that viscous fingering effectively occurs provided only that the Péclet number is sufficiently high. Significant differences in the (non-linear) development of fingers between monotonic and non-monotonic viscosity profiles are explained in Ref. [99]. Due to the stable barrier in the non-monotonic profile, fingers spread further in displacing fluid than in the displaced fluid. More complicated configurations can happen in the case of reacting mixture $A + B \rightarrow C$ depending the properties of the reactants and the product. The viscosity profile can be monotonic or non-monotonic and changes in time according to the diffusion and reaction rates. Some phenomena are identical to those observed in the viscous fingering of a finite slice [100] because of the finite-size of the chemical reaction zone. De Wit and other authors study numerically and experimentally the influence of the reaction on the viscous fingering instability, see Refs. [101, 102, 103, 104], to name a few. Nonetheless, they do not focus on the diffusion involving by the reactants and the product of the chemical reaction. Most of the analyses assumed generalized Fick formulation with the same or a constant Fick diffusion coefficient for all species, which is incorrect as already mentioned in Sec. 3.2 (see e.g. Eq. 3.15).

As we saw the viscous fingering instability is governed by diffusion and viscosity. Contrary to binary mixtures where each species diffuses at an equal rate ($\mathcal{D}_{12} = \mathcal{D}_{21}$), in ternary mixtures the components can diffuse at different rates ($\mathcal{D}_{12} \neq \mathcal{D}_{13} \neq \mathcal{D}_{22}$). Also, multi-component effects such as reverse diffusion, osmotic diffusion and diffusion barrier may take place and the overall diffusion dynamics become more complex. While in binary mixtures, we have $x_1 = 1 - x_2$ and $\nabla x_1 = -\nabla x_2$, these constraints on the molar fractions in ternary mixtures are less strict: $x_1 + x_2 + x_3 = 1$ and $\nabla x_1 + \nabla x_2 + \nabla x_3 = \mathbf{0}$. In consequence, since the viscosity depends on the mixture composition, the viscosity evolution could change significantly compared to the binary case. The passage from a mixture composed of two species to a mixture composed of three species modify the dynamics of the core ingredients of the viscous fingering instability. In this section, we will focus on a particular flow configuration in order to highlight the non-negligible effect of ternary mixtures. The case where viscous fingering instability is induced by reverse diffusion as, to our knowledge, has not been investigated yet and is presented.

We consider three species having equal molecular masses in different quantities. The

composition of the invading and displaced mixtures is given in Table 11.1. The molar fractions of the first and second components follow a similar step-like pattern as in the case of the binary mixture. Note that here the first species is less present than the second species in the invading mixture and vice versa in the displaced mixture. The third species is in equal amounts in both invading and displaced fluids. Before defining additional physical parameters, we would like to present how this ternary mixture will be visualized. Each species is associated with a Red-Green-Blue (RGB) color channel. With this strategy, one is able to get the mixture composition from one single color-map similarly to the case of a binary mixture.



Molar fractions	Invading fluid	Displaced fluid
x_1 (R)	0.1	0.45
x_2 (G)	0.45	0.1
x_3 (B)	0.45	0.45
RGB color		

Table 11.1 – Composition of the invading and displaced mixtures.

We set the diffusion coefficients such as the third species will be subject to reverse diffusion. This can be estimated by means of the generalized Fick formulation in the case of pure diffusion (Sec. 3.2):

$$\mathbf{J}_2 = -c_t D_{22} \nabla x_2 - c_t D_{23} \nabla x_3, \quad (11.14)$$

$$\mathbf{J}_3 = -c_t D_{32} \nabla x_2 - c_t D_{33} \nabla x_3, \quad (11.15)$$

$$\text{and } \mathbf{J}_1 = -\mathbf{J}_2 - \mathbf{J}_3. \quad (11.16)$$

We want $\mathbf{J}_3 < \mathbf{0}$ and since $\nabla x_3 = \mathbf{0}$ and $\nabla x_2 = (< 0, 0)^T$, we should have $D_{32} < 0$. We recall the definition of the Fick diffusion coefficients from Eqs. (3.15) and (3.16):

$$D_{33} = \mathcal{D}_{13} (x_3 \mathcal{D}_{12} + (1 - x_3) \mathcal{D}_{23}) / \hat{D}, \quad (11.17)$$

$$D_{32} = x_3 \mathcal{D}_{12} (\mathcal{D}_{13} - \mathcal{D}_{23}) / \hat{D}, \quad (11.18)$$

$$\text{with } \hat{D} = x_1 \mathcal{D}_{23} + x_2 \mathcal{D}_{13} + x_3 \mathcal{D}_{23}. \quad (11.19)$$

Hence, we should set $\mathcal{D}_{23} > \mathcal{D}_{13}$. We choose the following diffusion matrix

$$\mathcal{D}_{mn} = \frac{L_{ref} U}{Pe} \begin{pmatrix} 0 & 1 & 0.1 \\ 1 & 0 & 1 \\ 0.1 & 1 & 0 \end{pmatrix}, \quad (11.20)$$

with $Pe = 5000$, $U = 2 \times 10^{-3} \text{lu}$, the Darcy number is unchanged $Da = 6.25 \times 10^{-8}$ and the porous medium is simulated using the Brinkman force strategy. Pure viscosities are set based on $Re_{0,1} = 10$ and $R_{12} = \ln(\mu_{0,1}/\mu_{0,2}) = 0$, $R_{13} = \ln(\mu_{0,1}/\mu_{0,3}) = 3$. The first and second components which vary on either side of the miscible interface have the same pure viscosity whereas the pure viscosity of the third species present in equal

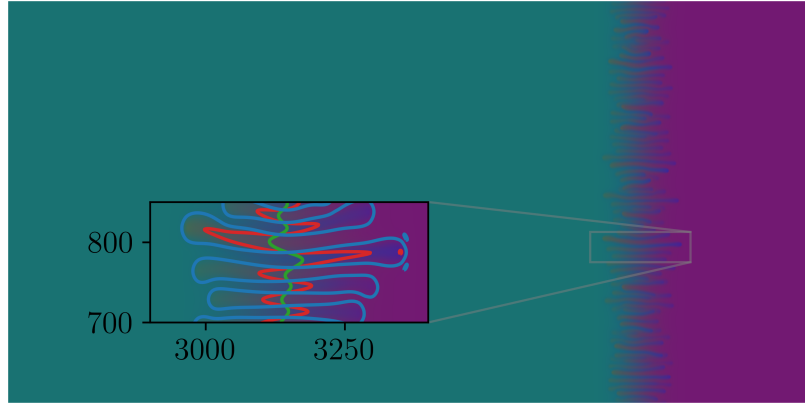


Figure 11.9 – Snapshot of the viscous fingering induced by reverse diffusion at $t^* = 1.8$. The whole domain ($n_x = 4000$, $n_y = 2000$) is plotted using the same aspect ratio for both x and y-axes. Each species is associated with a RGB channel. An enlargement is provided and contour-plots for $x_1 = x_2 = 0.275$ and $x_3 = 0.45$ are drawn.

amount in the domain is approximately twenty times lower. Compare to the binary case, the boundary conditions are modified. We still use the non-equilibrium bounce-back, which prescribes for each species either a pressure or a velocity at boundary nodes. For a mixture composed of two species, we impose a velocity and small changes of partial pressure, mixture composition, occur. In the case of three components, the variation of the mixture composition at boundaries compared to the initial target fluid becomes important so we choose to impose the pressure at both boundaries using Eq. (11.4) adapted for three species. However, this introduces a decrease of the inlet velocity as time progresses which means that the Péclet number loses some of its meaning.

Both invading and displaced mixtures have the same viscosity. If the diffusion coefficients have all the same value, no fingers appear. In this specific case, this reduces to a binary mixture as the first and second species are identical and, as expected, the flow is stable when both invading and displaced fluid viscosities are equal. However if we set $\mathcal{D}_{13} = 0.1\mathcal{D}_{12} = 0.1\mathcal{D}_{23}$, fingers develop as pictured in Fig. 11.9 although the initial configuration is stable. Small fingers develop at latter times compared with the binary case and their blue color suggests that they are mainly composed of the third species. From the enlargement, one can also notice that the interface of the first (red) species is also perturbed.

The fingering is actually caused by the reverse diffusion as inferred by Fig. 11.10. At the beginning of the simulation, the third and less viscous component is uniformly present. However, the third (blue) species starts to diffuse from the displaced to the invading mixtures (osmotic diffusion) and keeps diffusing against its concentration gradient (reverse diffusion) and the main flow. In consequence, at $t^* = 0.1$ a local increase of the concentration of the third species is clearly visible and is followed by a local decrease. This change of the mixture composition affects significantly the properties of the

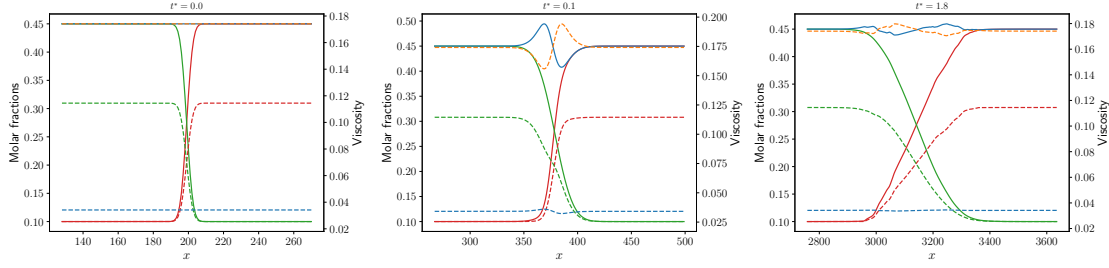


Figure 11.10 – Evolution at different times of the mean molar fraction over the transverse direction, continuous lines, and the mean partial viscosity over the transverse direction, dashed lines. Viscosities are normalized by the pure viscosity $\mu_{0,1}$. Red, first species; green, second species; blue, third species. Orange stand for the mean mixture viscosity over the transverse direction.

mixture and results locally in a decrease followed by an increase of the mixture viscosity that will trigger the instability. The effective viscosity ratio is lower and makes the instability less intense compared to the binary case. We recall that the mixture viscosity is computed *a posteriori* whereas only partial viscosities are employed in the model. At $t^* = 1.8$ the mean transverse molar fraction of the third species fluctuates because of the presence of fingers as show in Fig. 11.9.

From the enlargement of Fig. 11.9, one can observe the variation of the interface between the invading and the displaced mixtures. If the blue-colored fingers highlights the displacement of the third species because of the instability, the contour-plots show also some variations of the interface for the first (red) species. In figure 11.11, the molar fraction of each species is plotted. The right figure shows that some fingers are composed of a very high concentration of the third species. Counter-fingers, which moves from the right to the left, have a minimal molar fractions of $x_3 = 0.33$. We underline that reverse diffusion should still occur and tends to reinforce the fingers of medium concentration and limits the development of counter-propagating fingers of low concentration. However, the third species is not the only one to be subject to fingering. The interface of the first species is also significantly deformed. The invading fluid penetrates primarily the displaced fluid through the low viscosity fingers caused by the third species and avoids the zone of high viscosity. In consequence, small fingers of low concentration of the first species develop. One can notice that in contrary almost no fingering for the second species appears. The interface seems symmetrically diffuse. This phenomenon can be explained by means of the diffusion matrix Eq. (11.20). Since $\mathcal{D}_{13} < \mathcal{D}_{12}$, the first species diffuses predominantly in the second species compared to the third species that is why small fingers of low concentration of the first species are visible in fingering caused by the third species. Concerning the second component, we have $\mathcal{D}_{12} = \mathcal{D}_{23}$ and the second species diffuses in both species equitably.

We emphasize the importance of the ternary diffusion on the instability onset. Diffusion governs the reverse fingering, its strength, and its life span until the diffusion barrier

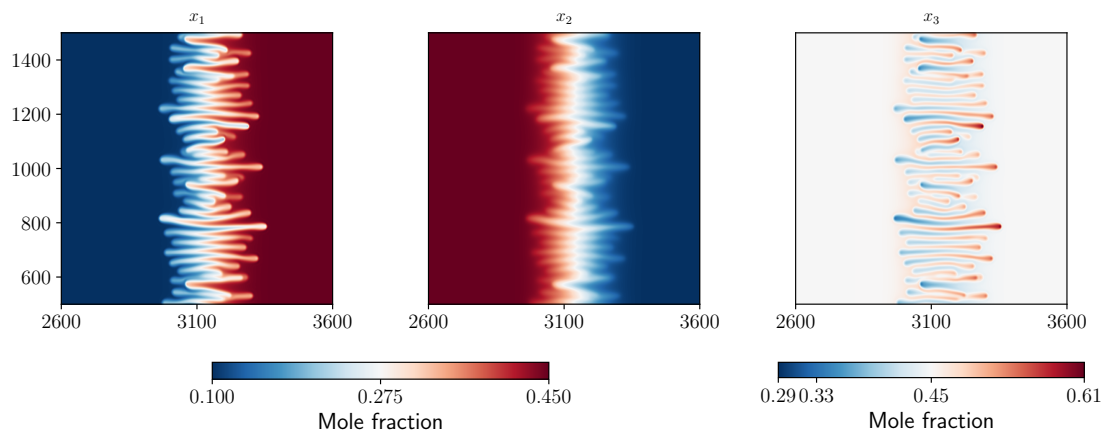


Figure 11.11 – Color-map of the molar fraction at $t^* = 1.8$ for each species. Portion of the domain ($n_x = 4000$, $n_y = 2000$).

point. Diffusion also controls the growth of the perturbations and stabilizes the flow as in the binary case. In the present configuration, we deliberately showcase the significant influence of reverse diffusion on a flow, which is initially stable. With the numbers of possible different configurations of viscosities and diffusion coefficients, a complete parametric study is out of the scope of the present work. Nonetheless, we expect to see more subtle or on the contrary dramatic changes due to the multi-component effects compared to the viscous fingering of two species.

Chapter 12

Synthesis

This last part is dedicated to the simulation of the viscous fingering instability. The interaction between the two (or three) miscible components are described by the aforementioned miscible lattice Boltzmann model. The core ingredients of the instability are related to the molecular diffusion and the viscosity, or more specifically inter-molecular friction forces and partial viscosities in our model. Generally, the instability occurs when a less viscous fluid displaces a more viscous fluid in a porous medium. Thus we investigate two strategies to mimic the effect of the porous medium: the gray lattice Boltzmann and Brinkman force models.

The viscous fingering is first studied in the case of a binary mixture. At early times in the linear regime, the growth rate of the perturbation is computed for different Péclet numbers. The growth rate, as well as the most dangerous and the cutoff numbers, increase with the Péclet number. A good agreement is found with a linear stability analysis where a quasi-steady-state-approximation is used. For intermediate times where strong linear interactions take place, the development of the instability is described globally through the mixing length. A high Péclet number leads to a more intense instability. Two regimes are visible. The growth of the mixing length is first dominated by diffusion and then by convection.

For both early and intermediate times investigated here, the gray lattice Boltzmann and Brinkman force models lead to equivalent results. The comparison with the literature, quantitatively for early times and qualitatively for intermediate times agrees well. This is very encouraging and gives much credence to the proposed lattice Boltzmann model. Indeed with a different approach, we recover accurately the physics of the viscous fingering.

Finally, the behavior of the instability can dramatically change for a mixture of three and more species compared to the binary case. For instance, viscous fingering could be induced by reverse diffusion despite having a stable initial flow configuration.

Conclusion

The first part of this thesis covers the basics of the lattice Boltzmann method. Starting from the kinetic theory of gas and the Boltzmann equation, a discrete formulation is proposed. A major tool to obtain the resulting macroscopic equations is the Chapman and Enskog expansion procedure. The relaxation time is thus related to the viscous dissipation. Independently, we introduce the Maxwell-Stefan approach to deal with pure diffusion between species. This approach is more convenient and has a more rigorous physical meaning for three and more species compared to the traditional Fick formulation. Besides, we showcase some non-trivial diffusion effects that may occur during the diffusion of three and more components such as osmotic diffusion, reverse diffusion, and diffusion barrier. The fundamental contribution of this thesis is to combine these ideas and propose a lattice Boltzmann model for miscible gases in the second part of this thesis.

Different lattice Boltzmann models for multi-component flows already exist. Since there is no unique and generally accepted BGK-like collision operator, each model depends on the underlying kinetic theory chosen. However, for all models in the case of binary mixtures, the variation of momentum induced by the collision has a similar form as the inter-molecular friction force, i.e., a coefficient multiplied by the velocity difference of the two species. Any previous model requires to heavily modified the collision step compared to the standard formulation so as to take into account the interactions between components. This increase of complexity makes the algorithm more computationally expensive, and above all, it cannot be easily incorporated in existing LBM codes. The collision being the cornerstone of the LBM, changing the collision means usually rewrite the code entirely. In the proposed approach, the standard equilibrium is employed combined with the inter-molecular friction force. Much less effort is therefore needed to upgrade a single-fluid code to take into account diffusion between multiple species. The viscous dissipation is related to the relaxation toward the equilibrium state, and the molecular diffusion is associated with the inter-molecular diffusion force. To calculate the transport coefficients, we make use of the kinetic theory of gases. In addition to the (Maxwell-Stefan) diffusion coefficient, a partial viscosity is also defined for each species. The problem of a fixed lattice speed of sound peculiar to the LBM is circumvented by using an artificial force to modify the species equation of state according to the molecular mass of the component. Excellent agreements are found against analytical, experimental, and numerical results. The complex diffusion dynamics of three and more species is recovered, and the proposed model is capable of simulating osmotic diffusion, reverse diffusion, and diffusion barrier phenomena. After being validated the basic features of our model, we apply it to the viscous fingering instability and discuss the results obtained in the last part of the thesis.

The simulation of the viscous fingering instability is achieved by considering two species in different proportions in a porous medium: a less viscous mixture displacing a more viscous mixture. The core ingredients of the instability are the diffusion and the viscosity contrast between the components. Two strategies are investigated to mimic the effects of the porous medium. The gray lattice Boltzmann and Brinkman force models, although based on fundamentally different approaches, give in our case equivalent results.

For early times, we focus on the growth rate of the perturbation and the influence of the Péclet number. Comparisons with linear stability analyses agree well with the growth rate calculated from the simulations. For intermediate times, the evolution of the mixing length can be divided into two stages dominated first by diffusion then by convection, as found in the literature. The whole physics of the viscous fingering is thus accurately simulated. Nevertheless, multi-component diffusion effects are usually not taken into account in the case of viscous fingering with three and more species. These effects are non-negligible as we showcase an initial stable configuration that becomes unstable. The reverse diffusion induces fingering whose impact depends on the diffusion between species. After a successful application of the proposed model on the viscous fingering, we are longing to tackle other problems involving multi-species flows.

Perspectives

The derivation of the proposed model is rigorously correct only for dilute gases. We could, to a certain extent, apply it to liquids and general gases. The Maxwell-Stefan equations are also valid for low and high densities, liquids, and polymers, so we can assume that the inter-molecular friction force still adequately describe the molecular diffusion in these cases. The partial pressure is not well defined for a non-ideal gas, and its gradient should be substituted by the gradient of chemical potential. Transport coefficients should be calculated using the Eyring (liquids) or Enskog (dense gases) kinetic theories [1]. More fundamental studies are required on the model. For instance, the simulation of a mixing layer between three species could point out some interesting mechanisms. A comparison with a recent and well-documented experiment would be beneficial. A starting point could be to quantify the influence of the partial viscosities based on the experiments of variable viscosity jet flows carried out in Ref. [105].

Concerning the viscous fingering simulations, different configurations with the ternary mixture should be considered. A parametric study could be performed and draw out the first results obtained here. Another possibility is to model the pores at a global level instead of mimicking the porous medium. In spite of being computationally expensive, this simulation would highlight the different scale of the porous medium in play. Finally, we could notice that the porous drag force has a similar form as the Boussinesq's approximation made in double-diffusive convection problems in oceans, and opens new perspectives for the proposed model.

The following publications are related to this work (see also Appendix E):

- Lucien Vienne, et al. “Lattice Boltzmann method for miscible gases: A forcing-term approach”. In: *Physical Review E*. [106]
- Lucien Vienne, et al. “Viscous fingering simulation by the lattice Boltzmann method”. Under preparation.

Appendix

A	Hermite polynomials and Gauss-Hermite quadrature	121
A.1	Hermite polynomials 1-dimensional space	121
A.2	Hermite polynomials in d-dimensional space	122
A.3	Gauss-Hermite quadrature	123
B	Programming considerations	127
B.1	Code	127
B.2	HPC	128
C	Kinetic theory for the calculation of transport coefficients	129
C.1	Omega-integrals	129
C.2	Wilke's law	130
C.3	A more common formulation of the diffusion coefficient	132
D	Viscous fingering	135
D.1	Most dangerous and cutoff wave numbers	135
D.2	Color maps of the molar fraction for different Péclet numbers	135
E	Parallel activities	137
E.1	Conferences and discussions	137
E.2	Ercoftac Montestigliano spring-school	137
F	Résumé étendu des travaux de la thèse en français	143

Appendix A

Hermite polynomials and Gauss-Hermite quadrature

A.1 Hermite polynomials 1-dimensional space

Hermite polynomials are an orthogonal polynomials sequence defined by the weight function

$$\omega(x) = \frac{1}{\sqrt{2\pi}} e^{-x^2/2}, \quad (\text{A.1})$$

which is normalised so that $\int_{-\infty}^{\infty} \omega(x) dx = 1$. The expression of the weight function may slightly vary in the literature and accordingly the definition of the Hermite polynomials could be a little different. The n -th order of Hermite polynomials are constructed from the Rodrigues' formula

$$H^{(n)}(x) = (-1)^n \frac{1}{\omega(x)} \frac{d^n}{dx^n} \omega(x), \quad (\text{A.2})$$

and the first few polynomials are

$$H^{(0)}(x) = 1, \quad (\text{A.3})$$

$$H^{(1)}(x) = x, \quad (\text{A.4})$$

$$H^{(2)}(x) = x^2 - 1, \quad (\text{A.5})$$

$$H^{(3)}(x) = x^3 - 3x. \quad (\text{A.6})$$

One can find the recursion formula

$$H^{(n+1)}(x) = xH^{(n)}(x) - \frac{d}{dx}H^{(n)}(x) = xH^{(n)}(x) - nH^{(n-1)}(x) \quad (\text{A.7})$$

One of the interesting properties of the Hermite polynomials is their orthogonality with respect to the weight function $\omega(x)$

$$\int_{-\infty}^{\infty} \omega(x) H^{(m)}(x) H^{(n)}(x) dx = n! \delta_{mn}, \quad (\text{A.8})$$

APPENDIX A. HERMITE POLYNOMIALS AND GAUSS-HERMITE QUADRATURE

where δ_{mn} is the Kronecker symbol, i.e., $\delta_{mn} = 1$ if $m = n$ and 0 otherwise.

Any function f that is square integrable can be expanded in terms of Hermite polynomials as

$$f(x) = \sum_{n=0}^{\infty} a^{(n)} H^{(n)}(x). \quad (\text{A.9})$$

The Hermite expansion coefficient $a^{(n)}$ can be computed by multiplying the previous equation Eq. (A.9) by $\omega(x)H^m(x)$ and integrating

$$\int_{-\infty}^{\infty} \omega(x)H^m(x)f(x)dx = \sum_{n=0}^{\infty} a^{(n)} \int_{-\infty}^{\infty} \omega(x)H^m(x)H^{(n)}(x)dx = m! a^{(m)} \quad (\text{A.10})$$

$$a^{(m)} = \int_{-\infty}^{\infty} \frac{1}{m!} \omega(x)H^m(x)f(x)dx \quad (\text{A.11})$$

where the orthogonal property of the Hermite polynomials has been used to simplify the summation. Instead of using Eqs. (A.9) and (A.11), the following alternative expression is preferred

$$f(x) = \omega(x) \sum_{n=0}^{\infty} \frac{1}{n!} a^{(n)} H^{(n)}(x), \quad (\text{A.12})$$

where the expansion coefficient $a^{(n)}$ is given by

$$a^{(n)} = \int_{-\infty}^{\infty} H^m(x)f(x)dx. \quad (\text{A.13})$$

This (Gram-Charlier) series converges only if f approach zero faster than $e^{-x^2/4}$. In practice, this assumption is correct for gases that are not too far from the equilibrium state (at the equilibrium: $f \sim e^{-x^2/2}$) [12].

A.2 Hermite polynomials in d-dimensional space

All of these previous expressions can be generalized to a d -dimensional space as shown by Grad [107].

$$\mathbf{H}_i^{(n)}(\mathbf{x}) = (-1)^n \frac{1}{\omega(\mathbf{x})} \nabla_i^n \omega(\mathbf{x}), \quad \omega(\mathbf{x}) = \frac{1}{(2\pi)^{d/2}} e^{-\mathbf{x}^2/2} \quad (\text{A.14})$$

where $\mathbf{x}^2 = \mathbf{x} \cdot \mathbf{x}$ and the operator ∇_i^n is equivalent to

$$\nabla_i^n = \nabla_{(i_1, \dots, i_n)}^n = \frac{\partial}{\partial x_{i_1}} \cdots \frac{\partial}{\partial x_{i_n}}. \quad (\text{A.15})$$

With this definition, the first few polynomials are

$$H^{(0)}(\mathbf{x}) = 1, \quad (\text{A.16})$$

$$H_i^{(1)}(\mathbf{x}) = x_i, \quad (\text{A.17})$$

$$H_{ij}^{(2)}(\mathbf{x}) = x_i x_j - \delta_{ij}, \quad (\text{A.18})$$

$$H_{ijk}^{(3)}(\mathbf{x}) = x_i x_j x_k - x_i \delta_{jk} - x_j \delta_{ki} - x_k \delta_{ij}. \quad (\text{A.19})$$

The orthogonal relation becomes

$$\int \omega(\mathbf{x}) \mathbf{H}_i^{(m)}(\mathbf{x}) \mathbf{H}_j^{(n)}(\mathbf{x}) d\mathbf{x} = \prod_{p=1}^d n_p! \delta_{mn} \delta_{ij}^n, \quad (\text{A.20})$$

where δ_{ij}^n is the generalization of the Kronecker symbol, which is equal to 1 if (i_1, \dots, i_n) is a permutation of (j_1, \dots, j_n) and 0 otherwise. For $\mathbf{i} = (i_1, i_2, i_3, i_1)$, $n_1 = 2, n_2 = 1$, and $n_3 = 1$.

Finally, a function f that is square integral can be expanded as

$$f(\mathbf{x}) = \omega(\mathbf{x}) \sum_{n=0}^{\infty} \frac{1}{n!} \mathbf{a}_i^{(n)} \mathbf{H}_i^{(n)}(\mathbf{x}), \quad \text{with} \quad (\text{A.21})$$

$$\mathbf{a}_i^{(n)} = \int f(\mathbf{x}) \mathbf{H}_i^{(n)}(\mathbf{x}) d\mathbf{x} \quad (\text{A.22})$$

We point out that both $\mathbf{a}_i^{(n)}$ and $\mathbf{H}_i^{(n)}$ are tensors of rank n and this leads to this equivalent formulation

$$f(\mathbf{x}) = \omega(\mathbf{x}) \left(a^{(0)} H^{(0)} + \sum_{i=1}^d a_i^{(1)} H_i^{(1)} + \sum_{i,j=1}^d a_{ij}^{(2)} H_{ij}^{(2)} + \sum_{i,j,k=1}^d a_{ijk}^{(3)} H_{ijk}^{(3)} + \dots \right) \quad (\text{A.23})$$

A.3 Gauss-Hermite quadrature

A Gaussian quadrature approximates the following integral with only q points,

$$\int_a^b \omega(x) f(x) dx = \sum_{\alpha=0}^q \omega_{\alpha} f(x_{\alpha}), \quad (\text{A.24})$$

where $\omega(x)$ is an arbitrary weight function, ω_{α} are the weight of the quadrature, and x_{α} are the abscissas of the quadrature, which are the roots of the orthogonal polynomials for the scalar product $\int_a^b \omega(x) g(x) h(x) dx$. This quadrature is exact for any polynomials f of degree $2q - 1$ or less.

In particular if we choose the weight function as Eq. (A.1), the Gauss-Hermite quadrature is obtained. We recall that the expression of the weight function may slightly vary in the literature, and so as the weights and the abscissas. The abscissas are then the roots of the Hermite polynomials and the corresponding weights are [5]

$$\omega_{\alpha} = \frac{q!}{[qH^{(q-1)}(x_{\alpha})]^2}. \quad (\text{A.25})$$

Using Eqs. (A.3-A.6), the Gauss-Hermite quadrature up to $q = 3$ is constructed as shown in Table A.1.

The Gauss-Hermite quadrature can be generalized into a d -dimensional space.

$$\int \omega(\mathbf{x}) f(\mathbf{x}) d\mathbf{x} = \sum_{\alpha=0}^{q^d} \omega_{\alpha} f(\mathbf{x}_{\alpha}) \quad (\text{A.26})$$

APPENDIX A. HERMITE POLYNOMIALS AND GAUSS-HERMITE QUADRATURE

Number of abscissas q	Polynomial degree $2q - 1$	Abscissas x_α	Weight ω_α
1	1	0	1
2	3	-1, 1	1/2, 1/2
3	5	$-\sqrt{3}, 0, \sqrt{3}$	1/6, 2/3, 1/6

Table A.1 – Gauss-Hermite quadrature up to $q = 3$, which is exact for polynomials of degree 5 or less.

For instance, if we want to approximate a fifth-degree polynomial, the one-dimensional quadrature for $q = 3$ is used repeatedly. For a two-dimensional space, we find a nine points quadrature presented in Table A.2.

α	1	2 – 5	6 – 9
Abscissas	(0, 0)	$(\pm\sqrt{3}, 0)$ $(0, \pm\sqrt{3})$	$(\pm\sqrt{3}, \pm\sqrt{3})$
Weight	4/9	1/9	1/36

Table A.2 – Gauss-Hermite quadrature for a fifth-degree polynomial in two-dimensional space.

Similarly for a 3-dimensional space, the quadrature is obtained by a production of the 1-dimensional formula (see Table A.3). From the 27 points quadrature, one can derive

α	1	2 – 7	8 – 19	20 – 27
Abscissas	(0, 0, 0)	$(\pm\sqrt{3}, 0, 0)$ $(0, \pm\sqrt{3}, 0)$ $(0, 0, \pm\sqrt{3})$	$(\pm\sqrt{3}, \pm\sqrt{3}, 0)$ $(\pm\sqrt{3}, 0, \pm\sqrt{3})$ $(0, \pm\sqrt{3}, \pm\sqrt{3})$	$(\pm\sqrt{3}, \pm\sqrt{3}, \pm\sqrt{3})$
Weight	8/27	2/27	1/54	1/216

Table A.3 – Gauss-Hermite quadrature for a fifth-degree polynomial in three-dimensional space.

equivalent quadratures with less points, 15 (Table A.4) and 19 (Table A.4) abscissas [5].

Other and high order quadratures are possible [5] but only a few, like those presented here, coincide with normal Cartesian coordinates. The use of a quadrature compatible with a uniform Cartesian grid results in a perfect streaming step.

α	1	2 – 7	8 – 15
Abcissas	(0, 0, 0)	$(\pm\sqrt{3}, 0, 0)$ $(0, \pm\sqrt{3}, 0)$ $(0, 0, \pm\sqrt{3})$	$(\pm\sqrt{3}, \pm\sqrt{3}, \pm\sqrt{3})$
Weight	2/9	1/9	1/72

Table A.4 – Alternative Gauss-Hermite quadrature with 15 abscissas for a fifth-degree polynomial in three-dimensional space.

α	1	2 – 7	8 – 19
Abcissas	(0, 0, 0)	$(\pm\sqrt{3}, 0, 0)$ $(0, \pm\sqrt{3}, 0)$ $(0, 0, \pm\sqrt{3})$	$(\pm\sqrt{3}, \pm\sqrt{3}, 0)$ $(\pm\sqrt{3}, 0, \pm\sqrt{3})$ $(0, \pm\sqrt{3}, \pm\sqrt{3})$
Weight	1/3	1/18	1/36

Table A.5 – Alternative Gauss-Hermite quadrature with 19 abscissas for a fifth-degree polynomial in three-dimensional space.

Appendix B

Programming considerations

B.1 Code

The code employed in the present work is written from scratch using a combination of FORTRAN and Python. All the computations are done in FORTRAN routines which are wrapped in Python through the F2PY wrapper. Python is only used for the pre-processing, the scheduler and the data tree. Therefore, we join the advantages of both languages: the fast execution of FORTRAN and the ease of use and the plethora of libraries of Python.

The lattice Boltzmann algorithm involves only a few numerical operations and is mainly limited by the memory access speed. Most of the time spent in LBM is due to the memory transfer and not computations. Different possibilities exist to store data from slow to high-speed access: disk, memory, caches, and registers. Usually the program stores variables in the main memory and when computations are required, data are transferred from the memory to the registers. If the same data are reused again, a copy may be made and store in the caches to speed-up further accesses. Most optimizations of memory-bound programs are performed by reusing as much as possible the caches. Indeed when a data is copied to the caches, nearby data are also copied too. Memory layout has thus a significant impact on the performance. The lattice Boltzmann method is primarily composed of two steps: collision and streaming. Unfortunately, the optimal memory layout is different for both of these steps. In collision, the distribution functions from all the directions α at a single node \mathbf{x} are needed ($f[\alpha, \mathbf{x}]$ is optimal in FORTRAN column-major order) whereas the streaming steps requires all the neighboring node for each direction ($f[\mathbf{x}, \alpha]$ is optimal in FORTRAN column-major order). A wrong memory layout could be catastrophic and results in an algorithm at least two times slower. No general rule exists and the most efficient memory layout depends strongly on the computing architecture (caches sizes and other optimizations), and the domain size simulated and the number of velocities (9 in 2D, 15, 19, or 27 in 3D). We recommend to test and adapt the memory layout specifically to the target machine.

We would like also to provide two recommendations. First, when using a MRT collision operator, one should carry out the matrix-vector multiplication by hand and

code the result. Second, when performing the streaming step, do not use two arrays for the post-collision and post-streaming distribution functions. Only one array for the distribution functions is needed. During the streaming, the array has simply to be browsed in the standard way or in the reverse order depending on the memory layout and velocities to update and avoid to overwrite the relevant distribution functions.

B.2 HPC

High-Performance Computing denotes strategies to improve and achieve a high level of performance. As we mentioned before the limiting factor in the Lattice Boltzmann method is data transfers. One possible way to improve the code is to use multiple computational units, from hundreds to thousands, for the same problem and thereby data transfers are carried out in parallel. In the current code (D2Q9 and D3D19), this is accomplished by the means of the Message Passing Interface (MPI) paradigm. The problem domain is divided into multiple sub-domains where calculations are performed independently and synchronization is realized by sending-receiving messages. In practice, the computational domain is expanded with a layer of ghost nodes, which store a copy of the neighboring node from the adjacent MPI process and are updated just before the non-local streaming step. Reading and writing data in a unique file is also done in parallel using MPI dedicated functions and data-types. Other strategies have been investigated and tested to improve the code performance such as vectorizations, openMP, openACC (GPU), and cache blocking. Nonetheless, code optimization although being important is very time-consuming and we decide to stay with a standard MPI domain decomposition. We insist again that the memory layout impact is significant and may change compared to the standard sequential case, especially for GPU architectures.

The author acknowledges the "Institut du Développement et des Ressources en Informatique Scientifique" (IDRIS) for their advanced training courses regarding MPI, vectorization, openMP, and openACC.

Appendix C

Kinetic theory for the calculation of transport coefficients

C.1 Omega-integrals

We specify the expression of the Ω -integrals. We recall that the interactions of a similar pair of molecules can be approximated by the Lennard-Jones potential.

$$\varphi(r) = 4\epsilon \left[\left(\frac{\sigma}{r} \right)^{12} - \left(\frac{\sigma}{r} \right)^6 \right], \quad (\text{C.1})$$

where r is the distance between the molecules, σ the collision diameter, and ϵ the depth of the potential well. For a dissimilar (m, n) pair of molecules, we use the following standard mixing rules:

$$\sigma_{mn} = (\sigma_m + \sigma_n)/2, \quad (\text{C.2})$$

$$\epsilon_{mn} = \sqrt{\epsilon_m \epsilon_n}, \quad (\text{C.3})$$

$$\frac{1}{\psi_{mn}} = \frac{1}{\mathcal{M}_m} + \frac{1}{\mathcal{M}_n}. \quad (\text{C.4})$$

Unlike the rigid sphere model, the Lennard-Jones potential is a physically realistic potential, and the Ω -integrals can not be calculated analytically. However, we compute the Ω -integrals for the rigid sphere and introduce the Ω^* ratio, which embodies the deviation of the Ω -integrals between the Lennard-Jones and rigid sphere potentials.

$$\Omega_{mn}^{*(i,j)} = \Omega_{mn}^{(i,j)} / \Omega_{mn}^{rs(i,j)} \quad (\text{C.5})$$

with

$$\Omega_{mn}^{rs(i,j)} = \sqrt{\frac{k_B T}{2\pi\psi_{mn}}} \frac{(j+1)!}{2} \left[1 - \frac{1}{2} \frac{1 + (-1)^i}{1+i} \right] \pi (\sigma_{mn})^2. \quad (\text{C.6})$$

$\Omega_{mn}^{*(i,j)}$ depends only on $T^* = Tk_B/\epsilon_{mn}$ and its value is obtained from a fitted curve computed from a numerical integration [59, 108]. For more details about the potentials, we invite the reader to read the Chapter 8 of Ref. [1].

APPENDIX C. KINETIC THEORY FOR THE CALCULATION OF TRANSPORT COEFFICIENTS

Despite the derivation is rigorously correct only for dilute gases, we could to a certain extent, apply these results to liquids and dense gases by means of the Eyring and Enskog theories, respectively.

C.2 Wilke's law

The partial viscosities are obtained by solving the linear system Eq. (6.37). This approach is computationally expensive since this system has to be solved for each time step on each grid point. In this section, we propose to derive a simpler expression for partial viscosities. We will combine some assumptions made in Ref. [1] (§8.2.iii) and additional approximations suggested in Ref. [66]. Equations (6.38) and (6.39) can be written as

$$P_{mm} = \frac{1}{\mu_{0,m}} + \sum_{n \neq m}^N \frac{1}{k_B T} \frac{x_n}{x_m} \frac{32}{3} \frac{\mathcal{M}_m \mathcal{M}_n}{(\mathcal{M}_m + \mathcal{M}_n)^2} \Omega_{mn}^{(1,1)} \times \left(1 + \frac{3}{5} \frac{\mathcal{M}_n}{\mathcal{M}_m} A_{mn}^* \right) \quad (\text{C.7})$$

and for $n \neq m$,

$$P_{mn} = -\frac{32}{3} \frac{1}{k_B T} \frac{\mathcal{M}_m \mathcal{M}_n}{(\mathcal{M}_m + \mathcal{M}_n)^2} \Omega_{mn}^{(1,1)} \left(1 - \frac{3}{5} A_{mn}^* \right) \quad (\text{C.8})$$

where $A_{mn}^* = \Omega^{*(2,2)}/\Omega^{*(1,1)}$ and $\mu_{0,m}$ is the pure viscosity of species m

$$\mu_{0,m} = 5k_B T / (8\Omega_{mm}^{(2,2)}). \quad (\text{C.9})$$

In general, the off-diagonal terms are small in comparison with the diagonal elements. If $A_{m,n}^* = 5/3 \forall(m, n)$, the off-diagonal terms vanish exactly. This assumption is proposed in Ref. [1] (§8.2.iii). When this assumption is made, the diagonal elements become

$$P_{mm} = \frac{1}{\mu_{0,m}} + \sum_{n \neq m}^N \frac{1}{k_B T} \frac{x_n}{x_m} \frac{32}{3} \frac{\mathcal{M}_n}{(\mathcal{M}_m + \mathcal{M}_n)} \Omega_{mn}^{(1,1)}. \quad (\text{C.10})$$

and for $n \neq m$,

$$P_{mn} = 0 \quad (\text{C.11})$$

Using Eq. (6.43), we rewrite Eq. (C.10) as

$$P_{mm} = \frac{1}{\mu_{0,m}} + \sum_{n \neq m}^N \frac{x_n}{x_m} \frac{2k_B T}{p \mathcal{M}_m \mathcal{D}_{mn}}. \quad (\text{C.12})$$

This yield to our first approximation of the partial viscosity according to the diffusion coefficients

$$\mu_m = \left[\frac{1}{\mu_{0,m}} + \frac{2RT}{p x_m M_m} \sum_{n \neq m}^N \frac{x_n}{\mathcal{D}_{mn}} \right]^{-1}, \quad (\text{C.13})$$

APPENDIX C. KINETIC THEORY FOR THE CALCULATION OF TRANSPORT
COEFFICIENTS

by definition, we have $\mathcal{M}_m = M_m \mathcal{N}_a$ where \mathcal{N}_a is the Avogadro number and M_m is the molar mass of species m and the universal gas constant $R = k_B \mathcal{N}_a$. The numerical constant 2 is often replaced by the empirical value 1.385 [109].

In the next paragraph, we make further assumptions result in an approximation of the partial viscosity in terms of pure viscosities. From Eq. (C.5) and Eq. (C.6), we write

$$\Omega_{mn}^{(1,1)} = \Omega_{mn}^{*(1,1)} \times \sqrt{\frac{k_B T \pi (\mathcal{M}_m + \mathcal{M}_n)}{2} \frac{1}{\mathcal{M}_m \mathcal{M}_n} \frac{1}{4} [\sigma_m + \sigma_n]^2}. \quad (\text{C.14})$$

For collisions between particles of the same species, we can invert Eq. (C.6),

$$\sigma_m = \sigma_{mm} = \left[\Omega_{mm}^{rs(1,1)} \times \sqrt{\frac{\mathcal{M}_m}{k_B T \pi}} \right]^{\frac{1}{2}} \quad (\text{C.15})$$

but the expression of $\Omega_{mm}^{rs(1,1)}$ can be computed from the pure viscosity

$$\Omega_{mm}^{rs(1,1)} = \frac{\Omega_{mm}^{(2,2)}}{2A_{mm}^* \Omega_{mm}^{*(1,1)}} = \frac{3}{16} k_B T \frac{1}{\Omega_{mm}^{*(1,1)} \mu_{0,m}}. \quad (\text{C.16})$$

Thus by combining Eqs. (C.15) and (C.16) into Eq. (C.14), we get

$$\begin{aligned} \Omega_{mn}^{(1,1)} &= \Omega_{mn}^{*(1,1)} \times \frac{3}{64\sqrt{2}} k_B T \sqrt{\frac{\mathcal{M}_m + \mathcal{M}_n}{\mathcal{M}_m \mathcal{M}_n}} \\ &\times \left[\left(\Omega_{mm}^{*(1,1)} \mu_{0,m} \right)^{-\frac{1}{2}} (\mathcal{M}_m)^{\frac{1}{4}} + \left(\Omega_{nn}^{*(1,1)} \mu_{0,n} \right)^{-\frac{1}{2}} (\mathcal{M}_n)^{\frac{1}{4}} \right]^2. \end{aligned} \quad (\text{C.17})$$

Let also assume as suggested in Ref. [66]

$$\frac{\Omega_{mn}^{*(1,1)}}{\Omega_{mm}^{*(1,1)}} \approx 1 \quad \text{and} \quad \frac{\Omega_{mn}^{*(1,1)}}{\Omega_{nn}^{*(1,1)}} \approx 1. \quad (\text{C.18})$$

These previous expressions do not necessary need to be viewed as equal. Therefore, the error caused by both assumptions may fortuitously cancel in Eq. (C.17). If we factorize, $\Omega_{mn}^{(1,1)}$ becomes

$$\Omega_{mn}^{(1,1)} = \frac{3}{64\sqrt{2}} k_B T \sqrt{\frac{\mathcal{M}_m + \mathcal{M}_n}{\mathcal{M}_n}} \times \frac{1}{\mu_{0,m}} \left[1 + \left(\frac{\mu_{0,m}}{\mu_{0,n}} \right)^{\frac{1}{2}} \left(\frac{\mathcal{M}_n}{\mathcal{M}_m} \right)^{\frac{1}{4}} \right]^2. \quad (\text{C.19})$$

Finally the diagonal elements P_{mm} Eq. (C.10) can be computed as

$$P_{mm} = \frac{1}{\mu_{0,m}} + \sum_{n \neq m}^N \frac{1}{2\sqrt{2}} \frac{x_n}{x_m} \left(\frac{\mathcal{M}_n}{\mathcal{M}_m + \mathcal{M}_n} \right)^{\frac{1}{2}} \times \frac{1}{\mu_{0,m}} \left[1 + \left(\frac{\mu_{0,m}}{\mu_{0,n}} \right)^{\frac{1}{2}} \left(\frac{\mathcal{M}_n}{\mathcal{M}_m} \right)^{\frac{1}{4}} \right]^2. \quad (\text{C.20})$$

The partial viscosities are then equal to

$$\mu_m = \frac{\mu_{0,m}}{1 + \sum_{n \neq m}^N \frac{x_n}{x_m} \Phi_{mn}} = \frac{x_m \mu_{0,m}}{\sum_n^N x_n \Phi_{mn}} \quad (\text{C.21})$$

with

$$\Phi_{mn} = \frac{1}{2\sqrt{2}} \left(1 + \frac{M_m}{M_n}\right)^{-\frac{1}{2}} \left[1 + \left(\frac{\mu_{0,m}}{\mu_{0,n}}\right)^{\frac{1}{2}} \left(\frac{M_n}{M_m}\right)^{\frac{1}{4}}\right]^2. \quad (\text{C.22})$$

This formulation of the partial viscosities is much simpler than solving the linear system Eq. (6.37) since the former only involves the molar fractions, and the pure viscosity and the molar mass of each species. If one defines the mixture viscosity as

$$\mu_{mixture} = \sum_m^N \mu_m, \quad (\text{C.23})$$

Wilke's law for the viscosity of a gas mixture is then recovered [66]. The summation of partial viscosities over all species results in Wilke's law. Therefore, Wilke's law is a consequence and not the origin of the derivation of the partial viscosities. Indeed recovering Wilke's law is consistent with the mixture momentum equation.

In figure C.1, viscosities of binary mixtures *He-Ar* and *CO₂-C₃H₈* calculated by inversion of the matrix are plotted as well as the approximated solution. Concerning the system inversion, the Ω -integrals are first computed for the rigid sphere model using Table C.1 and the deviation between the Lennard-Jones and rigid sphere potentials Ω^* is obtained by a fitting curve from a numerical integration [59, 108].

m		<i>Ar</i>	<i>He</i>	<i>CO₂</i>	<i>C₃H₈</i>
M_m	[g/mol]	39.948	4.0026	44.0095	44.0956
ϵ_m/k_B	[K]	124.	35.70	190.	206.
σ_m	[nm]	0.3418	0.2576	0.3996	0.5240

Table C.1 – Kinetic constants from Ref. [1].

C.3 A more common formulation of the diffusion coefficient

The notation used here is based on Molecular theory of gases and liquids by Hirschfelder, Curtiss, and Bird [1]. A more common formulation for the diffusion coefficient is given by Hirschfelder-Bird-Spotz or in chapter 11 of Ref. [108] and can be obtained following the definitions given in Appendix C.1.

$$\mathcal{D}_{mn} = \mathcal{D}_{nm} = \frac{3(\mathcal{M}_m + \mathcal{M}_n)}{16p\mathcal{M}_m\mathcal{M}_n} \frac{(k_B T)^2}{\Omega_{mn}^{(1,1)}}. \quad (\text{C.24})$$

APPENDIX C. KINETIC THEORY FOR THE CALCULATION OF TRANSPORT COEFFICIENTS

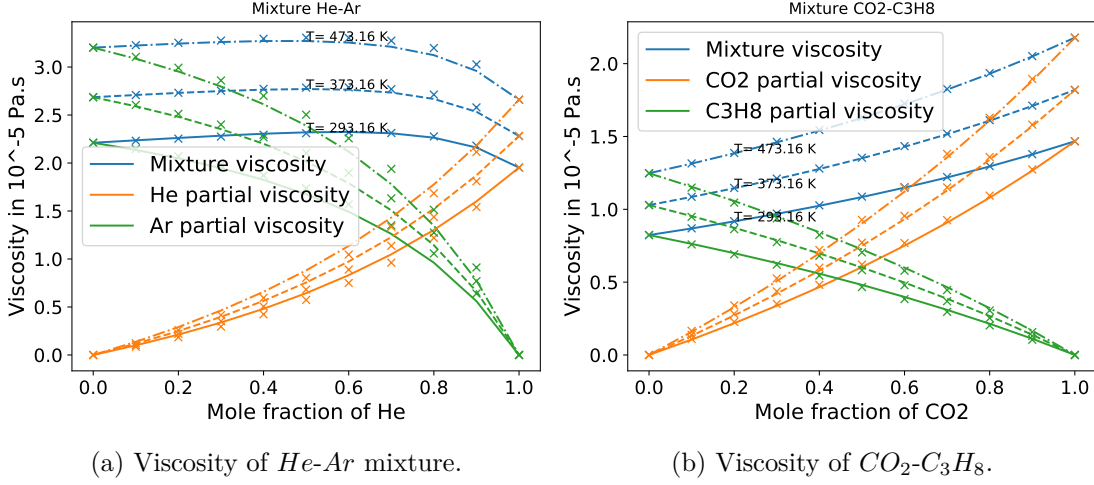


Figure C.1 – Viscosity of a binary mixture. Lines stand for viscosity calculated by inversion of the matrix. Markers represent the approximated solutions.

Using Eq. (C.5) and Eq. (C.6) yield

$$\Omega_{mn}^{(1,1)} = \Omega_{mn}^{rs(1,1)} \times \Omega_{mn}^{*(1,1)}, \quad (\text{C.25})$$

$$\Omega_{mn}^{(1,1)} = \sqrt{\frac{k_B T}{2\pi} \frac{\mathcal{M}_m + \mathcal{M}_n}{\mathcal{M}_m \mathcal{M}_n}} \pi \sigma_{mn}^2 \Omega_{mn}^{*(1,1)}. \quad (\text{C.26})$$

$$\mathcal{D}_{mn} = \frac{3}{16} \left(\frac{2\pi}{\mathcal{M}_{mn}} \right)^{1/2} \frac{(k_B T)^{5/2}}{p \pi \sigma_{mn}^2 \Omega_{mn}^{*(1,1)}} \quad (\text{C.27})$$

$$\mathcal{D}_{mn} = \frac{3}{16} \left(\frac{2\pi}{\mathcal{M}_{mn}} \right)^{1/2} \frac{(k_B T)^{3/2}}{n \pi \sigma_{mn}^2 \Omega_{mn}^{*(1,1)}} \quad (\text{C.28})$$

where we introduce the reduced mass $\mathcal{M}_{mn} = \mathcal{M}_m \mathcal{M}_n / (\mathcal{M}_m + \mathcal{M}_n)$ and use the ideal gas law $p = nk_B T$ with n the number density of molecules. The diffusion coefficient is formulated this way (in terms of $\Omega_{mn}^{(1,1)}$ instead of $\Omega_{mn}^{*(1,1)}$) in order to be consistent with the formulation of Eqs. (6.38) and (6.39). In addition, this formulation does not postulate any form of the interaction potential. The expression from Hirschfelder-Bird-Spotz assumes that the Ω -integrals are calculated from the rigid sphere model multiplied by the deviation between the Lennard-Jones and rigid sphere potentials (Eq. C.5).

Appendix D

Viscous fingering

D.1 Most dangerous and cutoff wave numbers

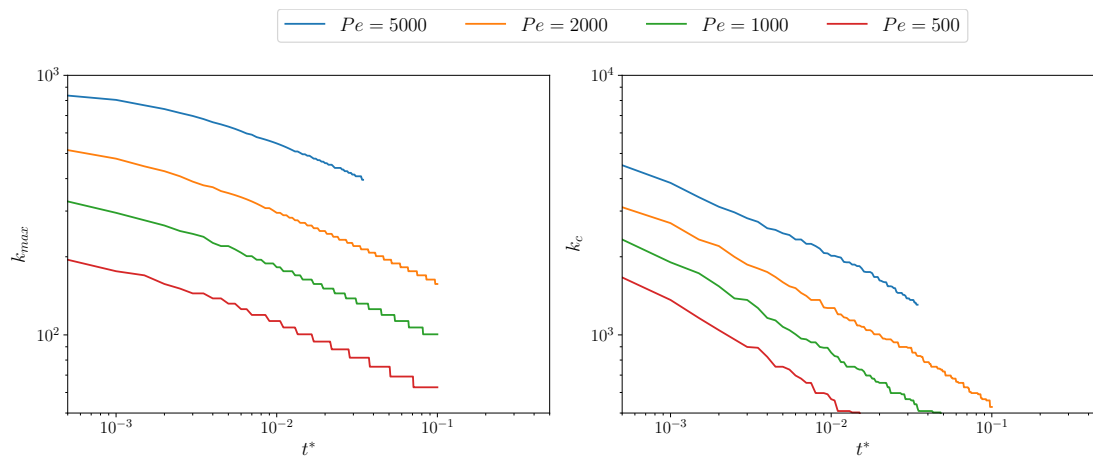


Figure D.1 – Most dangerous (k_{max}) and cutoff wave numbers according to times for different Péclet numbers. For $t^* > 0.035$ and $Pe = 5000$, non-linear interactions take place and corresponding points are not plotted. $k_c \sim t^{*-0.36}$ and $k_{max} \sim t^{*-0.26}$.

D.2 Color maps of the molar fraction for different Péclet numbers

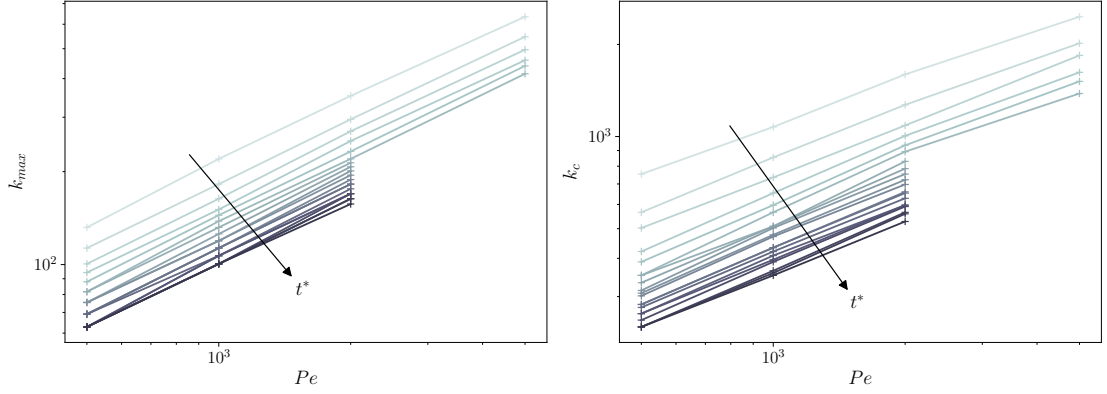


Figure D.2 – Most dangerous (k_{max}) and cutoff wave numbers according to the Péclet numbers for different times. The color gradient of lines denotes the time evolution from $t^* = 0.005$ to 0.1 with $\Delta t^* = 0.05$. For $t^* > 0.035$ and $Pe = 5000$, non-linear interactions take place and corresponding points are not plotted. $k_c \sim Pe^{0.59}$ and $k_{max} \sim Pe^{0.70}$.

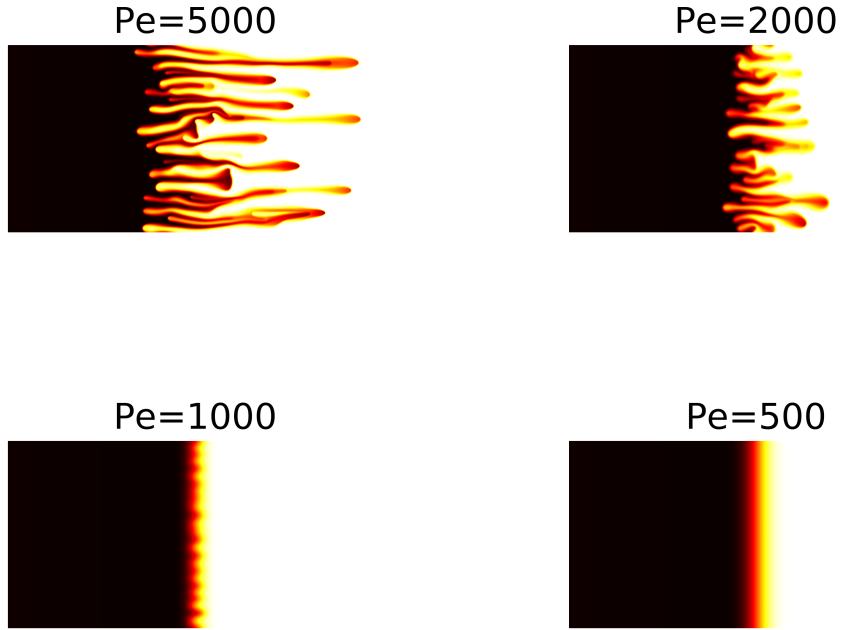


Figure D.3 – Instability development for $R = 3$ and different Péclet values at $t^* = 0.9$. The whole domain ($n_x = 4000, n_y = 2000$) is plotted. The color-map (black-red-yellow-white) represents the variation of the molar fraction from $x_1 = 0.9$ to $x_1 = 0.1$. Same scaling is used for both x and y-axes.

Appendix E

Parallel activities

E.1 Conferences and discussions

In the course of the three years of this thesis, I have the opportunity to attend some conferences. In chronological order, they are

- ICMMES 2017, Nantes (FR), poster
- DSFD 2018, Worcester (US), poster
- AIAA aviation 2019, Dallas (US), talk & proceeding [110]
- ICMMES 2019, Edinburgh (UK), talk

Also I acknowledge Prof. DUBOIS for the organization of monthly meetings as part of the Groupe de travail "Schémas de Boltzmann sur réseau".

E.2 Ercoftac Montestigliano spring-school

In April 2018, I attended the Ercoftac Montestigliano spring-school. This one week-long workshop includes lectures and a group project. The main topic was the lattice Boltzmann method and our group project was dedicated to moving curved boundaries. I provide below some extracts of the report.

Fluid-Solid interactions in the lattice Boltzmann method

Maximilian Egg¹, Lucien Vienne²

¹ Imperial College London, England

² Conservatoire National des Arts et Métiers, France

E.2.1 Abstract

This short report is a summary of our work during our stay at the ERCOFTAC Montestigliano Workshop. The topic covered in this workshop was the lattice Boltzmann method, introducing this numerical method to those who had not encountered it

previously as well as allowing those familiar with it to broaden their knowledge. After several introductory lectures, we were tasked with studying the implementation of curved and moving boundaries in the framework of the lattice Boltzmann method. We present here the method used and a few results obtained.

E.2.2 Acknowledgements

We would like to acknowledge and thank Ilya Karlin and Fabian Bösch for their significant work in running this workshop. They prepared several outstanding lectures to demonstrate the power of the lattice Boltzmann method, as well as guiding us in the implementation thereof by providing an excellent skeleton code for us to begin with. Furthermore, they provided invaluable advice during the group project stage and helped us achieve an in-depth understanding of the features of the lattice Boltzmann method. This report would not have been possible in its present form without their considerable help. We would also like to thank the organizers of the workshop, Peter Schmid and Shervin Bagheri, who worked tirelessly in the background to give us a platform to work and learn during our stay. Lastly, we would like to thank ERCOFTAC for funding this workshop and providing us with an opportunity to experience techniques which may not be within our own research areas. To conclude, we would both like to emphasize that we very much enjoyed our stay at the ERCOFTAC Montestigliano Workshop, and were able to come away with much more than we had ever anticipated.

E.2.3 Introduction

The lattice Boltzmann method (LBM) is a method for simulating fluid flows by solving a simplified kinetic model. Distribution functions (populations) are governed by the Boltzmann equation where collisions are approximated by a Bhatnagar-Gross-Krook (BGK) collision operator. More advanced collision operators have been developed, including the multiple relaxation time, cumulant, regularized or entropic LBM, which are usually introduced to remedy stability defects.

It can be shown that the Navier-Stokes equations are recovered through the Chapman and Enskog expansion procedure in the hydrodynamic limit and the macroscopic quantities can be computed through population moments. Due to the discretisation of the kinetic velocity space, the LBM is mostly limited to weakly compressible flows (small Mach number $Ma \leq 0.3$). Nonetheless, the LBM has successfully been applied to several different fields such as acoustics, thermal flows, multiphase flows, flows through porous media, and multi-species flows. Thanks to its mesoscopic features, easily understandable and implementable algorithm and great performance in parallel computing, the LBM can be a powerful tool for the simulation of complex flows.

One area of particular interest is fluid-solid interactions, due to its pervasiveness in so many industrial applications. By extension this implies that the study of boundary conditions within the LBM framework can be of significant interest. The unique feature of the lattice Boltzmann method is the fact, that it operates by streaming and colliding populations, which means that imposing macroscopic variables like density or

momentum require the introduction of a kinetic representation to mimic this macroscopic picture. The most popular and easiest LBM fluid-structure interaction is called bounce-back. Bounce-back imposes a no-slip condition on the solid surface by reflecting the populations going into the solid back into the opposite direction. Its advantages like mass conservation, ease of implementation and locality explain why it is a widely used boundary condition. However, in most practical problems, boundaries in fluid dynamics can not be considered as a flat, resting, rigid interface. The curved wall of a car or a plane can not be correctly modelled by the crude staircase approximation and when considering moving boundaries the bounce-back is unfit to deal with these complex fluid-solid interactions.

To model more complex solids, two main approaches are used in the literature to simulate moving curved boundaries: immersed boundary methods and Cartesian interpolation grid methods. Immersed boundary methods are based on the combination of the lattice (Eulerian grid) and Lagrangian markers which depict the solid frontiers. A force is then included at the Navier-Stokes level, according to a chosen kernel function, to mimic the influence of the solid on the fluid. This method was not used during our stay at Montestigliano, so we shall not present this method here and will solely focus on Cartesian interpolation grid methods which act on the populations, and are described in more details later.

This report is organized as follows: we first introduce the lattice Boltzmann method and the Grad's approximation for curved and moving boundaries followed by validations obtained for a stationary cylinder, an oscillating cylinder and multiple shapes. Results are quite satisfactory and prove that this boundary condition is applicable to the simulation of moving and curved boundaries in the lattice Boltzmann method. This report is based on the article [111] where the latter method is firstly introduced.

E.2.4 Some results

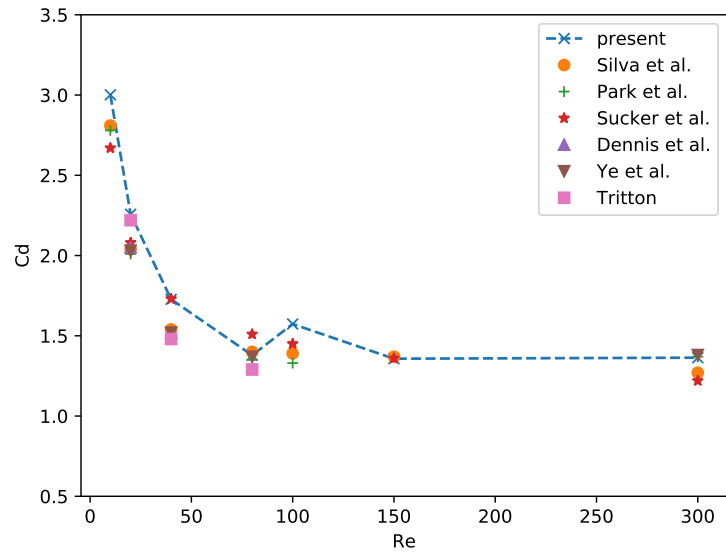


Figure E.1 – Drag coefficient comparison of a 2D-stationary cylinder with the implemented method and results found in the literature.

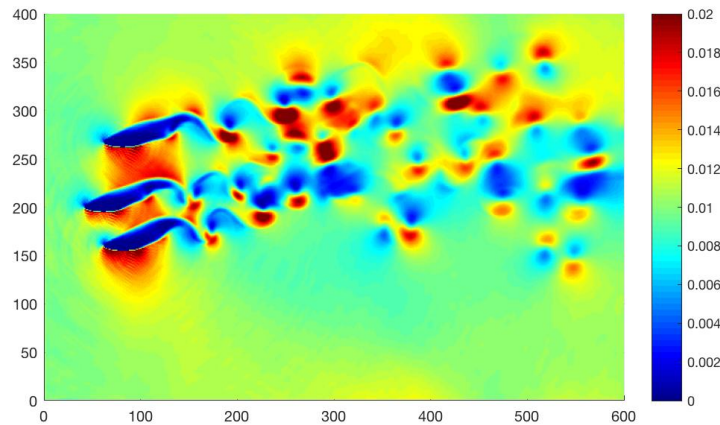


Figure E.2 – Velocity field of three moving (up and down) fishes.

E.2.5 Conclusion

The simplicity, efficiency and power of the LB method is demonstrated by the fact that we were able to implement a LB solver which was able to effectively simulate moving solids within a moving fluid. The theory underlining the computation is instinctive and simple to understand, while still remaining impressive in its ability to accurately simulate flowfields.

There were several extensions that we attempted to complete during our stay at the workshop, namely the effect of gravity and drag on a falling solid, where the velocity and acceleration are directly reliant thereupon. The force computations practically fall out for free from the LB solver, however the velocity implementation was not completed in time. Furthermore, a rudimentary passive-scalar field was introduced, however we were unable to verify the accuracy of it. However, these are not the only extensions that could have been implemented, only the ones that we decided to focus on. Other topics we may have explored are springs between solids, deforming shapes and multi-phase flows.

In conclusion, when the LB method is compared to other numerical methods, it is hard to understand why this method is not more popular. It is able to avoid any expensive meshing (and with moving solids re-meshing) and expensive derivative calculations while staying second-order accurate in time and space. The introduction of LB variables and the normalization thereof to unity, further adds to the simplicity of the method and its easy understanding.

While we were not able to achieve anything scientifically meaningful within our short stay at the Workshop, the power and capability of the LB method have definitely left an impression and we will aim to incorporate this numerical method in future research undertakings.

Annexe F

Résumé étendu des travaux de la thèse en français

Introduction

La mécanique des fluides est une branche de la physique dédiée à l'étude des écoulements de gaz et liquides. Prenons l'exemple de l'air que nous respirons, à notre échelle, cet air est continu et uniforme, et nous utilisons généralement les termes tels que sa densité ou sa vitesse pour le décrire. Toutefois, si on observe l'air à échelle suffisante ($\approx 10^{-9}\text{m}$), nous pourrions voir des milliards de molécules bougeant dans les sens et entrant en collision entre elles. Suivre tout ces mouvements individuellement demande un incroyable effort et n'est pas réaliste pour une quantité de gaz significative. L'évolution de la distribution des molécules de gaz est une quantité plus appropriée. C'est la voie choisie par la théorie cinétique des gaz dont la loi d'évolution est donnée par la célèbre équation de Boltzmann. Les effets des collisions ne sont pas triviaux et sont habituellement approximatés en définissant un état d'équilibre vers lequel le gaz tend à atteindre. Le temps requis pour que la distribution des molécules tend vers l'équilibre est principalement dû à la dissipation visqueuse causée par la collision des molécules. Si nous revenons à notre élément fondamental, l'air, nous notons qu'il est majoritairement composé de deux espèces : l'azote (N_2 , $\approx 78\%$) et l'oxygène (O_2 , $\approx 21\%$). En fait dans la nature, le mélange de différents composants est très courant et une espèce pure est généralement issue d'un procédé d'origine humaine. Dans le cas de mélange de composants, une approche évidente est alors de considérer l'évolution de la distribution de chaque type de molécules. La principale difficulté reste de prendre en compte de manière appropriée les effets des collisions entre les différents types de molécules.

Une solution analytique des écoulements d'un fluide est malheureusement connue uniquement pour des configurations simples. Nous rechercherons une solution approchée en considérant uniquement un certain nombre de trajectoires des molécules parmi l'ensemble des trajectoires possibles. De cette manière, le temps, l'espace, et la vitesse des molécules sont divisés en des éléments discrets représentant une réalité continue. Cette modélisation discrète du problème peut être résolu sur ordinateur à l'aide de techniques

numériques. La méthode de Boltzmann sur réseau (Lattice Boltzmann Method, LBM) est une formulation discrète particulière de l'équation de Boltzmann. Depuis ses débuts, il y a trente ans, cette méthode a gagné une certaine popularité, et elle est maintenant utilisée dans presque tous les problèmes habituellement rencontrés en mécanique des fluides notamment pour les écoulements multi-espèces. Son apparente simplicité et sa facilité d'implémentation par rapport aux méthodes traditionnelles pour résoudre des écoulements de fluides peut expliquer son utilisation croissante. Il faut cependant noter que ces deux précédents arguments sont seulement partiellement vrais : appliquer des démarches incroyables simples à un scénario complexe mènera à une fin compliquée.

Comme nous l'avons mentionner avant, la manière dont la distribution des molécules évolue après collision est décisive. Dans la méthode de Boltzmann sur réseau, il n'y a pas vraiment de consensus sur l'utilisation d'un unique opérateur de collision dans le cas de mélange de composants. Différent modèles pour des espèces miscibles ont été proposés selon la théorie cinétique sous-jacente choisie. Certains séparent la collision entre les molécules de même espèce et les molécules d'espèces différentes, d'autres emploient un équilibre global. L'étape de collision, déjà crucial, est alors modifiée et devient plus complexe. Dans le cadre de ce travail, une force de friction intermoléculaire est introduite pour modéliser les interactions entre les molécules de différent types causant principalement la diffusion entre les espèces. La collision habituelle, c'est à dire la relaxation vers l'état d'équilibre est utilisée. Les phénomènes de dissipation visqueuse (collision classique) et de diffusion moléculaire (force de friction intermoléculaire) sont séparés et peuvent être ajuster indépendamment. Le principal avantage de cette stratégie est sa compatibilité avec les opérateurs de collision existant qui font souvent l'objet d'optimisations en temps de calcul. Adapter un code mono-espèce pour aboutir à un code multi-espèces est aisé et demande beaucoup moins d'effort comparé aux précédentes tentatives. La collision étant la pierre angulaire de la méthode de Boltzmann sur réseau, un changement de collision aboutit généralement à la réécriture complète du code. De plus, il n'y a pas d'approximation du mélange, chaque espèce a ses propres coefficients de transport pouvant être calculés à l'aide de la théorie cinétique des gaz. En général, la diffusion et la convection sont vus comme deux mécanismes séparés : l'un agissant sur la masse d'une espèce, l'autre sur la quantité de mouvement du mélange. En utilisant une force de friction intermoléculaire, la diffusion et la convection sont couplés par l'intermédiaire la quantité de mouvement de chaque espèce. Les mécanismes de diffusion et de convection sont intimement liés dans de nombreux phénomènes physique tel que la digitation visqueuse.

La digitation visqueuse est une instabilité très répandue qui se développe lorsque un fluide moins visqueux déplace un fluide plus visqueux dans un milieu poreux. L'interface entre les deux fluides commence par se déformer et des arrangements en forme de doigt émergent et grossissent. Ce phénomène peut soit améliorer le mélange dans le milieu poreux ce qui est très difficile à cause de l'absence de turbulence pour activement mélanger l'écoulement ou avoir des répercussions dramatiques pour certains procédés. L'exemple typique est la récupération secondaire du pétrole pour lequel la digitation de la solution aqueuse moins visqueuse poussant le pétrole plus visqueux dans les réservoirs

souterrains poreux réduit fortement l'efficacité de la récupération. De manière similaire, une solution possible pour réduire le dioxyde de carbone présent dans l'atmosphère est de le capturer directement sur les sites de productions d'énergie et de gaz, et de le stocker dans les réservoirs poreux disponibles. L'étude de l'interaction entre le dioxyde de carbone supercritique et les fluides interstitiels, généralement de la saumure, est important. Le mélange résultant de la dissolution du dioxyde de carbone peut être sujet à la digitation et changer radicalement la distribution de dioxyde de carbone dans le réservoir. La digitation visqueuse est aussi néfaste dans le cas de la chromatographie, une technique utilisée pour séparer et identifier les constituants d'un mélange en le faisant s'écouler dans un milieu poreux. Le fluide déplaçant (l'éluant) peut être moins visqueux que le mélange à tester. L'interface initialement plane se déforme à cause de la digitation aboutissant une séparation infructueuse ou inefficace. Finalement, la digitation visqueuse joue un rôle majeur dans la contamination des sols en augmentant considérablement la zone polluée. L'étude de la digitation visqueuse est donc essentielle dans de nombreux domaines.

La thèse est structurée en trois principales parties. La première partie contient le contexte nécessaire pour aborder la méthode de Boltzmann sur réseau et les mélanges miscibles. Les deux premiers chapitres détaille les fondamentaux de la méthode de Boltzmann sur réseau pour un fluide simple composé d'un seul composant. Le troisième chapitre présente indépendamment l'approche de Maxwell et Stefan pour le transferts de masse à partir de considérations simples. Cela est fait délibérément car une dérivation directe à partir de la cinétique des gaz serait longue, compliquée, et paraphrasait le livre séminal *molecular theory of gases and liquids* par Hirschfelder, Curtiss et Bird [1]. La seconde partie est la principale contribution de la thèse. Nous combinons l'approche du troisième chapitre et la méthode de Boltzmann sur réseau. Le modèle proposé est ensuite validé à partir de résultats analytiques, expérimentaux et numériques. Finalement, la troisième partie présente une application. L'instabilité de digitation visqueuse est simulée pour deux et trois composants miscibles.

Principaux résultats

Un mélange est composé de plusieurs espèces et chaque espèce est définie par sa propre fonction de distribution qui est gouvernée par sa propre équation cinétique. Pour des raisons de simplicité, on considère uniquement un opérateur de collision de type BGK. Les opérateurs de collision avancés tel que le modèle à temps de relaxation multiples, le modèle entropique, le modèle régularisé, le modèle basé sur les cumulants, principalement développé pour remédier à des problèmes de stabilité numérique peuvent aussi être implémenter [21, 27, 28, 31]. Soit les indices m et n correspondant aux différentes espèces ($m, n = 1, 2, \dots, N$; N étant le nombre total d'espèces). La fonction de

distribution de l'espèce m , f_α^m , obéit à l'équation cinétique discrète suivante :

$$f_\alpha^m(\mathbf{x} + \mathbf{e}_\alpha \delta_t, t + \delta_t) = f_\alpha^m(\mathbf{x}, t) - \frac{\delta_t}{\tau_m} \left[f_\alpha^m(\mathbf{x}, t) - f_\alpha^{m(eq)}(\mathbf{x}, t) \right] + \left(1 - \frac{\delta_t}{2\tau_m}\right) \delta_t S_\alpha^m(\mathbf{x}, t) \quad (\text{F.1})$$

où \mathbf{x} , t , α , et τ_m sont, respectivement, les coordonnées spatiale, le temps, le nombre de vitesses cinétiques \mathbf{e}_α , et le temps de relaxation de chaque espèce. La fonction de distribution à l'équilibre, $f_\alpha^{m(eq)}$, est donnée par la formulation polynomiale usuelle

$$f_\alpha^{m(eq)} = \rho_m \omega_\alpha \left[1 + \frac{\mathbf{u}_m \cdot \mathbf{e}_\alpha}{c_s^2} + \frac{(\mathbf{u}_m \cdot \mathbf{e}_\alpha)^2}{2c_s^4} - \frac{\mathbf{u}_m \cdot \mathbf{u}_m}{2c_s^2} \right]. \quad (\text{F.2})$$

S_α^m est le terme source pour chaque espèce similaire au terme de forçage de Guo [13], couramment utilisé pour inclure des forces dans l'algorithme de Boltzmann sur réseau,

$$S_\alpha^m = \omega_\alpha \left[\frac{\mathbf{e}_\alpha - \mathbf{u}_m}{c_s^2} + \frac{(\mathbf{e}_\alpha \cdot \mathbf{u}_m) \mathbf{e}_\alpha}{c_s^4} \right] \cdot \mathbf{F}_m, \quad (\text{F.3})$$

\mathbf{F}_m étant la force agissant sur la m -ième espèce qui est dérivée dans la suite pour prendre en compte les interactions entre les espèces.

Dans cette étude, nous utilisons la discrétisation isotherme D2Q9 (bi-dimensionnel et 9 vitesses). Une extension à une formulation tri-dimensionnel (D3Q19 ou D3Q27) est trivial. La pseudo-vitesse du son est $c_s^2 = \frac{1}{3}$, les vitesses cinétiques peuvent s'exprimer comme

$$\mathbf{e}_\alpha = \begin{bmatrix} 0 & 1 & 0 & -1 & 0 & 1 & -1 & -1 & 1 \\ 0 & 0 & 1 & 0 & -1 & 1 & 1 & -1 & -1 \end{bmatrix}^T \quad 1 \leq \alpha \leq 9, \quad (\text{F.4})$$

et les poids du réseau sont égaux à

$$\omega_\alpha = \left[\frac{4}{9} \quad \frac{1}{9} \quad \frac{1}{9} \quad \frac{1}{9} \quad \frac{1}{9} \quad \frac{1}{36} \quad \frac{1}{36} \quad \frac{1}{36} \quad \frac{1}{36} \right]^T \quad 1 \leq \alpha \leq 9. \quad (\text{F.5})$$

Les quantités macroscopique, notamment la densité et la quantité de chaque espèce, sont obtenues en calculant les différents moments des fonctions de distribution.

$$\rho_m = \sum_\alpha f_\alpha^m, \quad \rho_m \mathbf{u}_m = \sum_\alpha f_\alpha^m \mathbf{e}_\alpha + \frac{\delta_t}{2} \mathbf{F}_m. \quad (\text{F.6})$$

Les équations macroscopiques résultantes sont les équations de conservation pour des écoulements à faible nombre de Mach soumis à une force volumique (par exemple, la gravité). Afin de prendre en compte l'interaction entre les différentes espèces miscibles, nous introduisons les forces de diffusions ou forces de friction selon l'approche de Maxwell-Stefan au transfert de masse :

$$\mathbf{F}_{\mathcal{D},m} = -p \sum_{n=1}^N \frac{x_m x_n}{\mathcal{D}_{mn}} (\mathbf{u}_m - \mathbf{u}_n), \quad (\text{F.7})$$

et \mathbf{F}_m devient

$$\mathbf{F}_m = \mathbf{F}_{\mathcal{D},m} + \mathbf{F}_{\mathcal{B},m}, \quad (\text{F.8})$$

où $\mathbf{F}_{\mathcal{B},m}$ est une force volumique. Ainsi les équations cinétiques discrètes (F.1) pour les différentes espèces sont couplées par l'intermédiaire de \mathbf{F}_m . Puisque les force de diffusion $\mathbf{F}_{\mathcal{D},m}$ dépendent de la vitesse, de la pression totale p , des fraction molaires x_m , et des coefficients de diffusion (Maxwell-Stefan) \mathcal{D}_{mn} , un système linéaire doit être résolu à chaque pas de temps afin de calculer la quantité de mouvement de chaque espèce grâce à l'équation (F.6). Cette force également appelée force de friction intermoléculaire dépend de la vitesse relative de chaque espèce. Ainsi, lorsque toutes les espèces ont la même vitesse, il n'y a pas de diffusion. Notons que la force de friction intramoléculaire liée à la viscosité est déjà pris en compte par l'opérateur de collision BGK de manière similaire au cas des écoulements mono-espèce. L'idée d'inclure les effets de diffusion comme une force agissant sur les molécules date des premiers travaux de la théorie cinétique des gaz par Maxwell [38]. La même expression a été rigoureusement dérivée plus tard par Chapman et Cowling [2], une discussion détaillée est donnée par Hirschfelder, Curtiss, et Bird [1] et Kerkhof et Geboers présentent une dérivation plus récente dans la référence [59]. De longs et compliqués développements mathématiques sont nécessaires pour obtenir cette force de friction intermoléculaire à partir de la théorie cinétique des gaz, elle ne donc pas présenté. Les principales étapes de la dérivation font appel au développement de Chapman et Enskog, à la linéarisation, de l'intégrale de collision (1.10) et à sa solution approchée par l'intermédiaire d'un développement en série des vitesses à partir des polynômes de Sonine (ou Laguerre) et non d'Hermite. Une méthode équivalente utilisant les polynômes d'Hermite, les équations des treize moments de Grad, a été proposée par Zhdanov [60].

Conclusion

La première partie de cette thèse couvre les fondamentaux de la méthode de Boltzmann sur réseau. Partant de la théorie cinétique des gaz et de l'équation de Boltzmann, une formulation discrète est proposé. Un outil majeur pour obtenir les équations macroscopiques en jeu est le développement de Chapman et Enskog. Le temps de relaxation est ainsi lié à la dissipation visqueuse. Indépendamment, nous introduisons l'approche proposée par Maxwell et Stefan pour modéliser la diffusion pure entre les espèces. Cette approche est plus commode et possède une interprétation plus physique dans le cas de trois ou plus espèces comparée à la formulation de Fick traditionnelle. De plus, nous mettons en avant les effets non-triviaux de diffusion multi-espèces qui peuvent apparaître lors de la diffusion de trois ou plus composants tel que la diffusion osmotique, la diffusion inverse et la barrière de diffusion. La contribution fondamentale de cette thèse est de combiner ces idées et de proposer une méthode de Boltzmann sur réseau pour les gaz miscibles dans la seconde partie de la thèse.

Différentes méthodes de Boltzmann sur réseau pour les écoulements multi-espèces existent déjà. Il n'y a pas un unique ou communément admis opérateur de collision de

type BGK, chaque modèle dépend de la théorie cinétique sous-jacente choisie. Cependant, pour tout les modèles dans le cas d'un mélange binaire, la variation de la quantité de mouvement induite par la collision a une forme similaire à la force intermoléculaire de friction, c'est à dire un coefficient multiplié par la différence de vitesse des deux espèces. Les précédents modèles nécessitent de fortement modifier l'étape de collision par rapport à la formulation standard afin de prendre en compte l'interaction entre les composants. L'algorithme est alors plus complexe, coûteux en temps de calcul, et par dessus tout, ne peut être facilement implémenter dans des codes existant. Le point central de la méthode de Boltzmann sur réseau est la collision, la modifier signifie généralement réécrire entièrement le code. Dans l'approche proposée, l'équilibre usuel est utilisé combiné avec la force de friction intermoléculaire. Beaucoup moins d'effort est alors requis pour transformer un code mono-espèce pour qu'il prenne en compte la diffusion entre de multiple espèces. La dissipation visqueuse est liée à la relaxation vers l'état d'équilibre tandis que la diffusion moléculaire est associée avec la force de friction intermoléculaire. Le calcul des coefficients de transport est possible à l'aide de la cinétique des gaz. En plus du coefficient de diffusion (Maxwell-Stefan), une viscosité partielle est également définie pour chaque composant. Le problème de la vitesse du son fixé par le réseau est propre à la méthode de Boltzmann sur réseau. Ce problème est évité en utilisant une force artificielle pour modifier l'équation d'état de chaque espèce en fonction de sa masse moléculaire. Les résultats obtenus sont en excellent accord avec des solutions analytiques, expérimentales, et numériques. La dynamique complexe de diffusion de trois espèces ou plus est retrouvée, et le modèle proposé est capable de simuler les phénomènes de diffusion osmotique, de diffusion inverse, et de barrière de diffusion. Après avoir validé les caractéristiques de notre modèle, nous l'appliquons à l'instabilité de digitation visqueuse et discutons des résultats obtenus dans la dernière partie de la thèse.

L'instabilité de digitation visqueuse est simulée en considérant dans un milieu poreux deux espèces dans des proportions différentes soit un mélange moins visqueux déplaçant un mélange plus visqueux. Les principaux moteurs de l'instabilité sont la diffusion et le contraste de viscosité entre les espèces. Deux stratégies sont envisagées pour simuler les effets d'un milieu poreux. Les méthodes de rebond partiel et de force de Brinkman bien que basées sur des approches fondamentalement différentes donnent dans notre cas des résultats identiques. Les taux de croissance de l'instabilité calculés à partir de la simulation coïncident avec ceux obtenus à partir d'analyses de stabilité linéaire. L'évolution de la longueur de mélange peut être divisée en deux étapes dominées d'abord par la diffusion puis par la convection. La physique de la digitation visqueuse est ainsi correctement simulée. Toutefois, les effets de diffusion multi-espèces ne sont généralement pas pris en compte lors de la digitation visqueuse de trois espèces et plus. Ces derniers ne sont pas négligeable puisque nous mettons en avant une configuration initialement stable qui se déstabilise. La diffusion inverse entraîne la digitation dont l'impact dépend de la diffusion entre les espèces. Après avoir appliqué avec succès notre modèle au cas de la digitation visqueuse, il nous tarde de nous nous attaquer à d'autres problèmes impliquant des écoulements multi-espèces.

Perspectives

La dérivation du modèle proposé est rigoureusement exacte seulement pour les gaz dilués. Nous pouvons, dans une certaine mesure, l'appliquer aux liquides et gaz généraux. Les équation de Maxwell-Stefan sont aussi valides pour les gaz de faible et grande densité, les liquides et les polymères. On peut supposer que la force de friction intermoléculaire est toujours adéquate pour décrire la diffusion moléculaire dans ces cas. La pression partielle n'est bien définie dans le cas des gaz non-idéaux et ses gradients doivent être remplacés par les gradient du potentiel chimique. Les coefficients de transport doivent être calculés à partir de la théorie cinétique d'Eyring (liquides) ou d'Enskog (gaz denses) [1]. Des études plus fondamentales sont nécessaires pour approfondir notre modèle. Par exemple, la simulation d'une couche de mélange entre trois espèces pourrait mettre en avant des mécanismes intéressants. Une comparaison avec une expérience récente et bien documentée serait bénéfique. Un point de départ pour mesurer l'influence des viscosités partielles peut se baser sur les expériences d'écoulements de jets à viscosité variable effectuées dans la référence [105].

Concernant les simulations de digitation visqueuse, d'autres configurations du mélange à trois espèces pourraient être considérées. Une étude paramétrique peut être envisagée et prolongerait les premiers résultats obtenus ici. Une autre possibilité est de modéliser les pores à la place de simuler leur effets. Bien qu'étant plus coûteux, cette simulation soulignera les différentes échelles du milieu poreux en jeu. Finalement, on peut noter que la force de friction du milieu poreux a une forme similaire à l'approximation de Boussinesq fait dans le cas des problèmes de double diffusion convection rencontrés dans les océans et cela ouvre de nouvelles perspectives pour le modèle proposé.

Les publications suivantes sont liées à ce travail (voir aussi l'annexe E) :

- Lucien Vienne, et al. "Lattice Boltzmann method for miscible gases : A forcing-term approach". In : *Physical Review E*. [106]
- Lucien Vienne, et al. "Viscous fingering simulation by the lattice Boltzmann method". Under preparation.

Bibliography

-
- [1] J. O. HIRSCHFELDER, C. F. CURTISS et R. B. BIRD. *Molecular Theory of Gases and Liquids*. Second printing. John Wiley & Sons, 1964. ISBN : 9780471400653 (cf. p. 5, 11, 13, 16, 19, 45, 47, 62, 71, 72, 82, 116, 129, 130, 132, 145, 147, 149).
- [2] S. CHAPMAN et T. G. COWLING. *The Mathematical Theory of Non-uniform Gases*. 3^e éd. Cambridge University Press, 1970. ISBN : 052140844X (cf. p. 13, 29, 30, 62, 147).
- [3] P. L. BHATNAGAR, E. P. GROSS et M. KROOK. « A Model for Collision Processes in Gases. I. Small Amplitude Processes in Charged and Neutral One-Component Systems ». In : *Phys. Rev.* 94 (3 1954), p. 511–525. DOI : 10.1103/PhysRev.94.511 (cf. p. 15, 58).
- [4] Timm KRÜGER et al. *The Lattice Boltzmann Method*. Springer International Publishing, 2017. DOI : 10.1007/978-3-319-44649-3 (cf. p. 16, 21, 58).
- [5] X. SHAN, X. YUAN et H. CHEN. « Kinetic theory representation of hydrodynamics : a way beyond the Navier-Stokes equation ». In : *Journal of Fluid Mechanics* 550.-1 (fév. 2006), p. 413. DOI : 10.1017/s0022112005008153 (cf. p. 19, 21, 24, 123, 124).
- [6] Sauro SUCCI. *The Lattice Boltzmann Equation for Fluid Dynamics and Beyond*. Oxford University Press, 2001. ISBN : 978-0-19-850398-9 (cf. p. 20).
- [7] Z. CHAI et T. S. ZHAO. « Lattice Boltzmann model for the convection-diffusion equation ». In : *Physical Review E* 87.6 (juin 2013). DOI : 10.1103/physreve.87.063309 (cf. p. 20).
- [8] Baochang SHI et Zhaoli GUO. « Lattice Boltzmann model for nonlinear convection-diffusion equations ». In : *Physical Review E* 79.1 (jan. 2009). DOI : 10.1103/physreve.79.016701 (cf. p. 20).
- [9] Hiroshi OTOMO, Bruce M. BOGHOSIAN et François DUBOIS. « Two complementary lattice-Boltzmann-based analyses for nonlinear systems ». In : *Physica A : Statistical Mechanics and its Applications* 486 (nov. 2017), p. 1000–1011. DOI : 10.1016/j.physa.2017.06.010 (cf. p. 20).
- [10] Yan GUANGWU. « A Lattice Boltzmann Equation for Waves ». In : *Journal of Computational Physics* 161.1 (juin 2000), p. 61–69. DOI : 10.1006/jcph.2000.6486 (cf. p. 20).
- [11] Jian Guo ZHOU. *Lattice Boltzmann Methods for Shallow Water Flows*. Springer Berlin Heidelberg, 2004. DOI : 10.1007/978-3-662-08276-8 (cf. p. 20).
- [12] Harold GRAD. « On the kinetic theory of rarefied gases ». In : *Communications on Pure and Applied Mathematics* 2.4 (déc. 1949), p. 331–407. DOI : 10.1002/cpa.3160020403 (cf. p. 21, 122).
- [13] Zhaoli GUO, Chuguang ZHENG et Baochang SHI. « Discrete lattice effects on the forcing term in the lattice Boltzmann method ». In : *Phys. Rev. E* 65 (4 avr. 2002), p. 046308. DOI : 10.1103/PhysRevE.65.046308 (cf. p. 28, 61, 64, 65, 146).

- [14] Michael JUNK, Axel KLAR et Li-Shi LUO. « Asymptotic analysis of the lattice Boltzmann equation ». In : *Journal of Computational Physics* 210.2 (déc. 2005), p. 676–704. DOI : 10.1016/j.jcp.2005.05.003 (cf. p. 34).
- [15] François DUBOIS. « Equivalent partial differential equations of a lattice Boltzmann scheme ». In : *Computers & Mathematics with Applications* 55.7 (avr. 2008), p. 1441–1449. DOI : 10.1016/j.camwa.2007.08.003 (cf. p. 34).
- [16] Wen-An YONG, Weifeng ZHAO et Li-Shi LUO. « Theory of the Lattice Boltzmann method : Derivation of macroscopic equations via the Maxwell iteration ». In : *Physical Review E* 93.3 (mar. 2016). DOI : 10.1103/physreve.93.033310 (cf. p. 34).
- [17] Simon MARIÉ, Denis RICOT et Pierre SAGAUT. « Comparison between lattice Boltzmann method and Navier–Stokes high order schemes for computational aeroacoustics ». In : *Journal of Computational Physics* 228.4 (mar. 2009), p. 1056–1070. DOI : 10.1016/j.jcp.2008.10.021 (cf. p. 34).
- [18] Gauthier WISSOCQ, Pierre SAGAUT et Jean-François BOUSSUGE. « An extended spectral analysis of the lattice Boltzmann method : modal interactions and stability issues ». In : *Journal of Computational Physics* 380 (mar. 2019), p. 311–333. DOI : 10.1016/j.jcp.2018.12.015 (cf. p. 34).
- [19] Pierre LALLEMAND et Li-Shi LUO. « Theory of the lattice Boltzmann method : Dispersion, dissipation, isotropy, Galilean invariance, and stability ». In : *Physical Review E* 61.6 (juin 2000), p. 6546–6562. DOI : 10.1103/physreve.61.6546 (cf. p. 36).
- [20] Christophe COREIXAS, Bastien CHOPARD et Jonas LATT. « Comprehensive comparison of collision models in the lattice Boltzmann framework : Theoretical investigations ». In : *Physical Review E* 100.3 (sept. 2019). DOI : 10.1103/physreve.100.033305 (cf. p. 36, 39).
- [21] P. V. COVENEY et al. « Multiple relaxation time lattice Boltzmann models in three dimensions ». In : *Philosophical Transactions of the Royal Society of London. Series A : Mathematical, Physical and Engineering Sciences* 360.1792 (2002), p. 437–451. DOI : 10.1098/rsta.2001.0955 (cf. p. 37, 61, 145).
- [22] Dominique D’HUMIÈRES et Irina GINZBURG. « Viscosity independent numerical errors for Lattice Boltzmann models : From recurrence equations to “magic” collision numbers ». In : *Computers & Mathematics with Applications* 58.5 (sept. 2009), p. 823–840. DOI : 10.1016/j.camwa.2009.02.008 (cf. p. 37, 94).
- [23] L. TALON et al. « Assessment of the two relaxation time Lattice-Boltzmann scheme to simulate Stokes flow in porous media ». In : *Water Resources Research* 48.4 (avr. 2012). DOI : 10.1029/2011wr011385 (cf. p. 37, 94).
- [24] Siarhei KHIREVICH, Irina GINZBURG et Ulrich TALLAREK. « Coarse- and fine-grid numerical behavior of MRT/TRT lattice-Boltzmann schemes in regular and random sphere packings ». In : *Journal of Computational Physics* 281 (jan. 2015), p. 708–742. DOI : 10.1016/j.jcp.2014.10.038 (cf. p. 37, 94).

-
- [25] Maxime FÉVRIER. « Extension et analyse des schémas de Boltzmann sur réseau : les schémas à vitesse relative. » Thèse de doct. 2015 (cf. p. 37).
- [26] Alessandro De ROSIS et Kai H. LUO. « Role of higher-order Hermite polynomials in the central-moments-based lattice Boltzmann framework ». In : *Physical Review E* 99.1 (jan. 2019). DOI : 10.1103/physreve.99.013301 (cf. p. 37).
- [27] Martin GEIER et al. « The cumulant lattice Boltzmann equation in three dimensions : Theory and validation ». In : *Computers & Mathematics with Applications* 70.4 (août 2015), p. 507–547. DOI : 10.1016/j.camwa.2015.05.001 (cf. p. 37, 61, 145).
- [28] Jonas LATT et Bastien CHOPARD. « Lattice Boltzmann method with regularized pre-collision distribution functions ». In : *Mathematics and Computers in Simulation* 72.2-6 (sept. 2006), p. 165–168. DOI : 10.1016/j.matcom.2006.05.017 (cf. p. 38, 61, 145).
- [29] Orestis MALASPINAS. « Increasing stability and accuracy of the lattice Boltzmann scheme : recursivity and regularization ». In : *arXiv e-prints*, arXiv :1505.06900 (mai 2015), arXiv :1505.06900. arXiv : 1505 . 06900 [physics.flu-dyn] (cf. p. 38).
- [30] Christophe COREIXAS. « High-order extension of the recursive regularized lattice Boltzmann method ». Thèse de doct. 2018 (cf. p. 38).
- [31] S. S. CHIKATAMARLA, S. ANSUMALI et I. V. KARLIN. « Entropic Lattice Boltzmann Models for Hydrodynamics in Three Dimensions ». In : *Phys. Rev. Lett.* 97 (1 juil. 2006), p. 010201. DOI : 10.1103/PhysRevLett.97.010201 (cf. p. 39, 61, 145).
- [32] Qisu ZOU et Xiaoyi HE. « On pressure and velocity boundary conditions for the lattice Boltzmann BGK model ». In : *Physics of Fluids* 9.6 (juin 1997), p. 1591–1598. DOI : 10.1063/1.869307 (cf. p. 42).
- [33] C. F. CURTISS et R. Byron BIRD. « Multicomponent Diffusion ». In : *Industrial & Engineering Chemistry Research* 38.7 (juil. 1999), p. 2515–2522. DOI : 10.1021/ie9901123 (cf. p. 45).
- [34] Charles F. CURTISS et Joseph O. HIRSCHFELDER. « Transport Properties of Multicomponent Gas Mixtures ». In : *The Journal of Chemical Physics* 17.6 (juin 1949), p. 550–555. DOI : 10.1063/1.1747319 (cf. p. 45, 47, 62, 71).
- [35] Forman A. WILLIAMS. *Combustion Theory*. 2^e éd. Benjamin/Cummings Pub. Co, 1985. ISBN : 0805398015 (cf. p. 45).
- [36] Ingo MÜLLER. « A thermodynamic theory of mixtures of fluids ». In : *Archive for Rational Mechanics and Analysis* 28.1 (jan. 1968), p. 1–39. DOI : 10.1007/bf00281561 (cf. p. 45).
- [37] R. TAYLOR et R. KRISHNA. *Multicomponent Mass Transfer*. John Wiley & Sons, 1993. ISBN : 9780471574170 (cf. p. 45, 47, 51, 80).

- [38] James Clerk MAXWELL. « IV. On the dynamical theory of gases ». In : *Philosophical Transactions of the Royal Society of London* 157 (1867), p. 49–88. DOI : 10.1098/rstl.1867.0004 (cf. p. 47, 62, 147).
- [39] J. STEFAN. « Über die Theorie der Eisbildung ». In : *Monatshefte für Mathematik und Physik* 1.1 (déc. 1890), p. 1–6. DOI : 10.1007/bf01692459 (cf. p. 47).
- [40] R. KRISHNA et J.A. WESSELINGH. « The Maxwell-Stefan approach to mass transfer ». In : *Chemical Engineering Science* 52.6 (mar. 1997), p. 861–911. DOI : 10.1016/s0009-2509(96)00458-7 (cf. p. 47).
- [41] J. B. DUNCAN et H. L. TOOR. « An experimental study of three component gas diffusion ». In : *AIChE Journal* 8.1 (mar. 1962), p. 38–41. DOI : 10.1002/aic.690080112 (cf. p. 48, 78).
- [42] S. A. HOSSEINI, N. DARABIHA et D. THÉVENIN. « Mass-conserving advection–diffusion Lattice Boltzmann model for multi-species reacting flows ». In : *Physica A : Statistical Mechanics and its Applications* 499 (2018), p. 40–57. DOI : 10.1016/j.physa.2018.01.034 (cf. p. 57).
- [43] Li-Shi LUO et Sharath S. GIRIMAJI. « Theory of the lattice Boltzmann method : Two-fluid model for binary mixtures ». In : *Phys. Rev. E* 67 (3 mar. 2003), p. 036302. DOI : 10.1103/PhysRevE.67.036302 (cf. p. 58, 71).
- [44] Lawrence SIROVICH. « Kinetic Modeling of Gas Mixtures ». In : *Physics of Fluids* 5.8 (1962), p. 908. DOI : 10.1063/1.1706706 (cf. p. 58).
- [45] Abhijit S. JOSHI et al. « Lattice Boltzmann method for continuum, multi-component mass diffusion in complex 2D geometries ». In : *Journal of Physics D : Applied Physics* 40.9 (avr. 2007), p. 2961–2971. DOI : 10.1088/0022-3727/40/9/044 (cf. p. 58).
- [46] Zi-Xiang TONG et al. « A multi-component lattice Boltzmann method in consistent with Stefan–Maxwell equations : Derivation, validation and application in porous medium ». In : *Computers & Fluids* 105 (déc. 2014), p. 155–165. DOI : 10.1016/j.compfluid.2014.09.022 (cf. p. 58, 71).
- [47] Pietro ASINARI. « Semi-implicit-linearized multiple-relaxation-time formulation of lattice Boltzmann schemes for mixture modeling ». In : *Phys. Rev. E* 73 (5 mai 2006), p. 056705. DOI : 10.1103/PhysRevE.73.056705 (cf. p. 58, 71).
- [48] Pietro ASINARI et Li-Shi LUO. « A consistent lattice Boltzmann equation with baroclinic coupling for mixtures ». In : *Journal of Computational Physics* 227.8 (avr. 2008), p. 3878–3895. DOI : 10.1016/j.jcp.2007.12.001 (cf. p. 58, 71).
- [49] Bernard B. HAMEL. « Kinetic Model for Binary Gas Mixtures ». In : *Physics of Fluids* 8.3 (1965), p. 418. DOI : 10.1063/1.1761239 (cf. p. 58).
- [50] Victor SOFONEA et Robert F. SEKERKA. « BGK models for diffusion in isothermal binary fluid systems ». In : *Physica A : Statistical Mechanics and its Applications* 299.3-4 (oct. 2001), p. 494–520. DOI : 10.1016/s0378-4371(01)00246-1 (cf. p. 58).

-
- [51] S. ARCIDIACONO et al. « Lattice Boltzmann model for the simulation of multicomponent mixtures ». In : *Phys. Rev. E* 76 (4 oct. 2007), p. 046703. DOI : 10.1103/PhysRevE.76.046703 (cf. p. 58, 71, 80, 81, 82).
- [52] Jinfen KANG, Nikolaos I. PRASIANAKIS et John MANTZARAS. « Thermal multi-component lattice Boltzmann model for catalytic reactive flows ». In : *Phys. Rev. E* 89 (6 juin 2014), p. 063310. DOI : 10.1103/PhysRevE.89.063310 (cf. p. 58, 71, 75).
- [53] Pietro ASINARI. « Multiple-relaxation-time lattice Boltzmann scheme for homogeneous mixture flows with external force ». In : *Phys. Rev. E* 77 (5 mai 2008), p. 056706. DOI : 10.1103/PhysRevE.77.056706 (cf. p. 58, 71).
- [54] Pierre ANDRIES, Kazuo AOKI et Benoit PERTHAME. « A Consistent BGK-Type Model for Gas Mixtures ». In : *Journal of Statistical Physics* 106.5/6 (2002), p. 993–1018. DOI : 10.1023/a:1014033703134 (cf. p. 58).
- [55] P. ASINARI. « Lattice Boltzmann scheme for mixture modeling : Analysis of the continuum diffusion regimes recovering Maxwell-Stefan model and incompressible Navier-Stokes equations ». In : *Physical Review E* 80 (5 2009), p. 056701. DOI : 10.1103/PhysRevE.80.056701 (cf. p. 58, 71).
- [56] Sam BENNETT, Pietro ASINARI et Paul J. DELLAR. « A lattice Boltzmann model for diffusion of binary gas mixtures that includes diffusion slip ». In : *International Journal for Numerical Methods in Fluids* 69.1 (mar. 2011), p. 171–189. DOI : 10.1002/flid.2549 (cf. p. 58).
- [57] Jens ZUDROP et al. « A robust lattice Boltzmann method for parallel simulations of multicomponent flows in complex geometries ». In : *Computers & Fluids* 153 (août 2017), p. 20–33. DOI : 10.1016/j.compfluid.2017.04.021 (cf. p. 58, 71).
- [58] Jens ZUDROP, Sabine ROLLER et Pietro ASINARI. « Lattice Boltzmann scheme for electrolytes by an extended Maxwell-Stefan approach ». In : *Phys. Rev. E* 89 (5 mai 2014), p. 053310. DOI : 10.1103/PhysRevE.89.053310 (cf. p. 58).
- [59] Piet J. A. M. KERKHOFF et Marcel A. M. GEBOERS. « Toward a unified theory of isotropic molecular transport phenomena ». In : *AIChE Journal* 51.1 (2004), p. 79–121. DOI : 10.1002/aic.10309 (cf. p. 62, 71, 129, 132, 147).
- [60] V ZHDANOV, Yu KAGAN et A SAZYKIN. « Effect of viscous transfer of momentum on diffusion in a gas mixture ». In : *Sov. Phys. JETP* 15 (1962), p. 596–602 (cf. p. 63, 147).
- [61] Michael E. MCCRACKEN et John ABRAHAM. « Lattice Boltzmann methods for binary mixtures with different molecular weights ». In : *Phys. Rev. E* 71 (4 avr. 2005), p. 046704. DOI : 10.1103/PhysRevE.71.046704 (cf. p. 63).
- [62] N. LOOLJE et al. « Introducing a variable speed of sound in single-component lattice Boltzmann simulations of isothermal fluid flows ». In : *Computers & Fluids* 167 (mai 2018), p. 129–145. DOI : 10.1016/j.compfluid.2018.02.037 (cf. p. 63, 73, 75).

- [63] J M BUICK et J A COSGROVE. « Investigation of a lattice Boltzmann model with a variable speed of sound ». In : *Journal of Physics A : Mathematical and General* 39.44 (oct. 2006), p. 13807–13815. DOI : 10.1088/0305-4470/39/44/013 (cf. p. 64).
- [64] Daniel D. JOSEPH et Yuriko Y. RENARDY. *Fluid Dynamics of Two Miscible Liquids with Diffusion and Gradient Stresses*. Springer New York, 1993, p. 324–395. DOI : 10.1007/978-1-4615-7061-5_6 (cf. p. 67).
- [65] Daniel D. JOSEPH, Adam HUANG et Howard HU. « Non-solenoidal velocity effects and Korteweg stresses in simple mixtures of incompressible liquids ». In : *Physica D : Nonlinear Phenomena* 97.1-3 (oct. 1996), p. 104–125. DOI : 10.1016/0167-2789(96)00097-8 (cf. p. 67).
- [66] C. R. WILKE. « A Viscosity Equation for Gas Mixtures ». In : *The Journal of Chemical Physics* 18.4 (avr. 1950), p. 517–519. DOI : 10.1063/1.1747673 (cf. p. 72, 130, 131, 132).
- [67] K. R. ARNOLD et H. L. TOOR. « Unsteady diffusion in ternary gas mixtures ». In : *AIChE Journal* 13.5 (sept. 1967), p. 909–914. DOI : 10.1002/aic.690130518 (cf. p. 78).
- [68] Rajamani KRISHNA. « Uphill diffusion in multicomponent mixtures ». In : *Chemical Society Reviews* 44.10 (2015), p. 2812–2836. DOI : 10.1039/c4cs00440j (cf. p. 80).
- [69] G M HOMSY. « Viscous Fingering in Porous Media ». In : *Annual Review of Fluid Mechanics* 19.1 (jan. 1987), p. 271–311. DOI : 10.1146/annurev.fl.19.010187.001415 (cf. p. 89, 90, 100, 104, 106).
- [70] Japinder S. NIJER, Duncan R. HEWITT et Jerome A. NEUFELD. « The dynamics of miscible viscous fingering from onset to shutdown ». In : *Journal of Fluid Mechanics* 837 (jan. 2018), p. 520–545. DOI : 10.1017/jfm.2017.829 (cf. p. 89, 91, 100, 104).
- [71] S. HILL et F. Inst. P. « Channeling in packed columns ». In : *Chemical Engineering Science* 1.6 (1952), p. 247–253. DOI : 10.1016/0009-2509(52)87017-4 (cf. p. 90).
- [72] Philip Geoffrey SAFFMAN et Geoffrey Ingram TAYLOR. « The penetration of a fluid into a porous medium or Hele-Shaw cell containing a more viscous liquid ». In : *Proceedings of the Royal Society of London. Series A. Mathematical and Physical Sciences* 245.1242 (juin 1958), p. 312–329. DOI : 10.1098/rspa.1958.0085 (cf. p. 90).
- [73] C. T. TAN et G. M. HOMSY. « Stability of miscible displacements in porous media : Rectilinear flow ». In : *Physics of Fluids* 29.11 (1986), p. 3549. DOI : 10.1063/1.865832 (cf. p. 91, 100, 101, 106).

-
- [74] Satyajit PRAMANIK et Manoranjan MISHRA. « Effect of Péclet number on miscible rectilinear displacement in a Hele-Shaw cell ». In : *Physical Review E* 91.3 (mar. 2015). DOI : 10.1103/physreve.91.033006 (cf. p. 91, 95, 98, 100, 101, 102, 106).
- [75] Tapan Kumar HOTA, Satyajit PRAMANIK et Manoranjan MISHRA. « Nonmodal linear stability analysis of miscible viscous fingering in porous media ». In : *Physical Review E* 92.5 (nov. 2015). DOI : 10.1103/physreve.92.053007 (cf. p. 91, 100, 101).
- [76] W. B. ZIMMERMAN et G. M. HOMS. « Three-dimensional viscous fingering : A numerical study ». In : *Physics of Fluids A : Fluid Dynamics* 4.9 (sept. 1992), p. 1901–1914. DOI : 10.1063/1.858361 (cf. p. 91, 97).
- [77] A. RIAZ et E. MEIBURG. « Three-dimensional miscible displacement simulations in homogeneous porous media with gravity override ». In : *Journal of Fluid Mechanics* 494 (nov. 2003), p. 95–117. DOI : 10.1017/s0022112003005974 (cf. p. 91, 97).
- [78] Birendra JHA, Luis CUETO-FELGUEROSO et Ruben JUANES. « Quantifying mixing in viscously unstable porous media flows ». In : *Physical Review E* 84.6 (déc. 2011). DOI : 10.1103/physreve.84.066312 (cf. p. 91).
- [79] Richard HOLME et Daniel H. ROTHMAN. « Lattice-gas and lattice-Boltzmann models of miscible fluids ». In : *Journal of Statistical Physics* 68.3-4 (août 1992), p. 409–429. DOI : 10.1007/bf01341756 (cf. p. 91).
- [80] N. RAKOTOMALALA, D. SALIN et P. WATZKY. « Miscible displacement between two parallel plates : BGK lattice gas simulations ». In : *Journal of Fluid Mechanics* 338 (mai 1997), p. 277–297. DOI : 10.1017/s0022112097004928 (cf. p. 91, 94).
- [81] Stuart D.C. WALSH, Holly BURWINKLE et Martin O. SAAR. « A new partial-bounceback lattice Boltzmann method for fluid flow through heterogeneous media ». In : *Computers & Geosciences* 35.6 (juin 2009), p. 1186–1193. DOI : 10.1016/j.cageo.2008.05.004 (cf. p. 93).
- [82] Jiujiang ZHU et Jingsheng MA. « An improved gray lattice Boltzmann model for simulating fluid flow in multi-scale porous media ». In : *Advances in Water Resources* 56 (juin 2013), p. 61–76. DOI : 10.1016/j.advwatres.2013.03.001 (cf. p. 93).
- [83] Hiroaki YOSHIDA et Hidemitsu HAYASHI. « Transmission–Reflection Coefficient in the Lattice Boltzmann Method ». In : *Journal of Statistical Physics* 155.2 (fév. 2014), p. 277–299. DOI : 10.1007/s10955-014-0953-7 (cf. p. 93, 94).
- [84] D.T. THORNE et M.C. SUKOP. « Lattice Boltzmann model for the elder problem ». In : *Computational Methods in Water Resources : Volume 2, Proceedings of the XVth International Conference on Computational Methods in Water Resources*. Elsevier, 2004, p. 1549–1557. DOI : 10.1016/s0167-5648(04)80165-5 (cf. p. 93).

- [85] Chen CHEN et al. « Chapman–Enskog Analyses on the Gray Lattice Boltzmann Equation Method for Fluid Flow in Porous Media ». In : *Journal of Statistical Physics* 171.3 (mar. 2018), p. 493–520. DOI : 10.1007/s10955-018-2005-1 (cf. p. 93, 94).
- [86] Irina GINZBURG. « Consistent lattice Boltzmann schemes for the Brinkman model of porous flow and infinite Chapman-Enskog expansion ». In : *Physical Review E* 77.6 (juin 2008). DOI : 10.1103/physreve.77.066704 (cf. p. 94).
- [87] Zhaoli GUO et T. S. ZHAO. « Lattice Boltzmann model for incompressible flows through porous media ». In : *Physical Review E* 66.3 (sept. 2002). DOI : 10.1103/physreve.66.036304 (cf. p. 94).
- [88] Nicos S. MARTYS. « Improved approximation of the Brinkman equation using a lattice Boltzmann method ». In : *Physics of Fluids* 13.6 (juin 2001), p. 1807–1810. DOI : 10.1063/1.1368846 (cf. p. 94).
- [89] Michael A. A. SPAID et Frederick R. PHELAN. « Lattice Boltzmann methods for modeling microscale flow in fibrous porous media ». In : *Physics of Fluids* 9.9 (sept. 1997), p. 2468–2474. DOI : 10.1063/1.869392 (cf. p. 94).
- [90] Patrick GROSFILS et al. « Structural and dynamical characterization of Hele–Shaw viscous fingering ». In : *Philosophical Transactions of the Royal Society of London. Series A : Mathematical, Physical and Engineering Sciences* 362.1821 (août 2004). Sous la dir. de M. AL–GHOUL, J. P. BOON et P. V. COVENEY, p. 1723–1734. DOI : 10.1098/rsta.2004.1398 (cf. p. 94).
- [91] Irina GINZBURG. « Comment on An improved gray Lattice Boltzmann model for simulating fluid flow in multi-scale porous media : Intrinsic links between LBE Brinkman schemes ». In : *Advances in Water Resources* 88 (fév. 2016), p. 241–249. DOI : 10.1016/j.advwatres.2014.05.007 (cf. p. 94).
- [92] M. NOROUZI et M. R. SHOGHI. « A numerical study on miscible viscous fingering instability in anisotropic porous media ». In : *Physics of Fluids* 26.8 (août 2014), p. 084102. DOI : 10.1063/1.4891228 (cf. p. 97, 100).
- [93] M’hamed BOUZIDI et al. « Lattice Boltzmann Equation on a Two-Dimensional Rectangular Grid ». In : *Journal of Computational Physics* 172.2 (sept. 2001), p. 704–717. DOI : 10.1006/jcph.2001.6850 (cf. p. 99).
- [94] L. A. Hegele JR, K. MATTILA et P. C. PHILIPPI. « Rectangular Lattice-Boltzmann Schemes with BGK-Collision Operator ». In : *Journal of Scientific Computing* 56.2 (déc. 2012), p. 230–242. DOI : 10.1007/s10915-012-9672-x (cf. p. 99).
- [95] Cheng PENG et al. « A hydrodynamically-consistent MRT lattice Boltzmann model on a 2D rectangular grid ». In : *Journal of Computational Physics* 326 (déc. 2016), p. 893–912. DOI : 10.1016/j.jcp.2016.09.031 (cf. p. 99).

-
- [96] E. VERGNAULT, O. MALASPINAS et P. SAGAUT. « A lattice Boltzmann method for nonlinear disturbances around an arbitrary base flow ». In : *Journal of Computational Physics* 231.24 (oct. 2012), p. 8070–8082. DOI : 10.1016/j.jcp.2012.07.021 (cf. p. 100).
- [97] José Miguel PÉREZ, Alfonso AGUILAR et Vassilis THEOFILIS. « Lattice Boltzmann methods for global linear instability analysis ». In : *Theoretical and Computational Fluid Dynamics* 31.5-6 (nov. 2016), p. 643–664. DOI : 10.1007/s00162-016-0416-7 (cf. p. 100).
- [98] O. MANICKAM et G. M. HOMSY. « Stability of miscible displacements in porous media with nonmonotonic viscosity profiles ». In : *Physics of Fluids A : Fluid Dynamics* 5.6 (juin 1993), p. 1356–1367. DOI : 10.1063/1.858571 (cf. p. 106).
- [99] O. MANICKAM et G. M. HOMSY. « Simulation of viscous fingering in miscible displacements with nonmonotonic viscosity profiles ». In : *Physics of Fluids* 6.1 (jan. 1994), p. 95–107. DOI : 10.1063/1.868049 (cf. p. 106).
- [100] M. MISHRA, M. MARTIN et A. De WIT. « Differences in miscible viscous fingering of finite width slices with positive or negative log-mobility ratio ». In : *Physical Review E* 78.6 (déc. 2008). DOI : 10.1103/physreve.78.066306 (cf. p. 106).
- [101] S. H. HEJAZI et al. « Viscous fingering of a miscible reactive $A + B \rightarrow C$ interface : a linear stability analysis ». In : *Journal of Fluid Mechanics* 652 (avr. 2010), p. 501–528. DOI : 10.1017/s0022112010000327 (cf. p. 106).
- [102] Y. NAGATSU et A. De WIT. « Viscous fingering of a miscible reactive $A+B \rightarrow C$ interface for an infinitely fast chemical reaction : Nonlinear simulations ». In : *Physics of Fluids* 23.4 (avr. 2011), p. 043103. DOI : 10.1063/1.3567176 (cf. p. 106).
- [103] L. A. RIOLFO et al. « Experimental evidence of reaction-driven miscible viscous fingering ». In : *Physical Review E* 85.1 (jan. 2012). DOI : 10.1103/physreve.85.015304 (cf. p. 106).
- [104] V. LOODTS et al. « Density profiles around $A+B \rightarrow C$ reaction-diffusion fronts in partially miscible systems : A general classification ». In : *Physical Review E* 94.4 (oct. 2016). DOI : 10.1103/physreve.94.043115 (cf. p. 106).
- [105] Benoît TALBOT. « Mélange et dynamique de la turbulence en écoulements libres à viscosité variable. » Thèse de doct. 2009 (cf. p. 116, 149).
- [106] Lucien VIENNE, Simon MARIÉ et Francesco GRASSO. « Lattice Boltzmann method for miscible gases : A forcing-term approach ». In : *Physical Review E* 100.2 (août 2019). DOI : 10.1103/physreve.100.023309 (cf. p. 116, 149).
- [107] Harold GRAD. « Note on N-dimensional Hermite polynomials ». In : *Communications on Pure and Applied Mathematics* 2.4 (déc. 1949), p. 325–330. DOI : 10.1002/cpa.3160020402 (cf. p. 122).
- [108] Bruce E POLING, John P O’CONNELL et J M PRAUSNITZ. *The properties of gases and liquids*. 5^e éd. McGraw-Hill, 2000. ISBN : 9780070116825 (cf. p. 129, 132).

- [109] J. W. BUDDENBERG et C. R. WILKE. « Calculation of Gas Mixture Viscosities. » In : *Industrial & Engineering Chemistry* 41.7 (juil. 1949), p. 1345–1347. DOI : 10.1021/ie50475a011 (cf. p. 131).
- [110] Lucien VIENNE, Simon MARIÉ et Francesco GRASSO. « Simulation of Viscous Fingering Instability by the Lattice Boltzmann Method ». In : *AIAA Aviation 2019 Forum*. American Institute of Aeronautics et Astronautics, juin 2019. DOI : 10.2514/6.2019-3432 (cf. p. 137).
- [111] B. DORSCHNER et al. « Grad’s approximation for moving and stationary walls in entropic lattice Boltzmann simulations ». In : *Journal of Computational Physics* 295 (août 2015), p. 340–354. DOI : 10.1016/j.jcp.2015.04.017 (cf. p. 139).

Résumé : La méthode de Boltzmann sur réseau est une formulation discrète particulière de l'équation de Boltzmann. Depuis ses débuts, il y a trente ans, cette méthode a gagné une certaine popularité et elle est maintenant utilisée dans presque tous les problèmes habituellement rencontrés en mécanique des fluides notamment pour les écoulements multi-espèces. Dans le cadre de ce travail, une force de friction intermoléculaire est introduite pour modéliser les interactions entre les molécules de différent types causant principalement la diffusion entre les espèces. Les phénomènes de dissipation visqueuse (collision usuelle) et de diffusion moléculaire (force de friction intermoléculaire) sont séparés et peuvent être ajustés indépendamment. Le principal avantage de cette stratégie est sa compatibilité avec des optimisations de la collision usuelle et les opérateurs de collision avancés. Adapter un code mono-espèce pour aboutir à un code multi-espèces est aisé et demande beaucoup moins d'effort comparé aux précédentes tentatives. De plus, il n'y a pas d'approximation du mélange, chaque espèce a ses propres coefficients de transport pouvant être calculés à l'aide de la théorie cinétique des gaz. En général, la diffusion et la convection sont vus comme deux mécanismes séparés : l'un agissant sur la masse d'une espèce, l'autre sur la quantité de mouvement du mélange. En utilisant une force de friction intermoléculaire, la diffusion et la convection sont couplés par l'intermédiaire la quantité de mouvement de chaque espèce. Les mécanismes de diffusion et de convection sont intimement liés dans de nombreux phénomènes physique tel que la digitation visqueuse.

L'instabilité de digitation visqueuse est simulée en considérant dans un milieu poreux deux espèces dans des proportions différentes soit un mélange moins visqueux déplaçant un mélange plus visqueux. Les principaux moteurs de l'instabilité sont la diffusion et le contraste de viscosité entre les espèces. Deux stratégies sont envisagées pour simuler les effets d'un milieu poreux. Les méthodes de rebond partiel et de force de Brinkman bien que basées sur des approches fondamentalement différentes donnent dans notre cas des résultats identiques. Les taux de croissance de l'instabilité calculés à partir de la simulation coïncident avec ceux obtenus à partir d'analyses de stabilité linéaire. L'évolution de la longueur de mélange peut être divisée en deux étapes dominées d'abord par la diffusion puis par la convection. La physique de la digitation visqueuse est ainsi correctement simulée. Toutefois, les effets de diffusion multi-espèces ne sont généralement pas pris en compte lors de la digitation visqueuse de trois espèces et plus. Ces derniers ne sont pas négligeable puisque nous mettons en avant une configuration initialement stable qui se déstabilise. La diffusion inverse entraîne la digitation dont l'impact dépend de la diffusion entre les espèces.

Mots clés : méthode de Boltzmann sur réseau, mécanique des fluides, écoulements multi-espèces, dynamique du mélange, instabilité de digitation visqueuse

Abstract: The lattice Boltzmann method (LBM) is a specific discrete formulation of the Boltzmann equation. Since its first premises, thirty years ago, this method has gained some popularity and is now applied to almost all standard problems encountered in fluid mechanics including multi-component flows. In this work, we introduce the inter-molecular friction forces to take into account the interaction between molecules of different kinds resulting primarily in diffusion between components. Viscous dissipation (standard collision) and molecular diffusion (inter-molecular friction forces) phenomena are split, and both can be tuned distinctively. The main advantage of this strategy is optimizations of the collision and advanced collision operators are readily compatible. Adapting an existing code from single component to multiple miscible components is straightforward and required much less effort than the large modifications needed from previously available lattice Boltzmann models. Besides, there is no mixture approximation: each species has its own transport coefficients, which can be calculated from the kinetic theory of gases. In general, diffusion and convection are dealt with two separate mechanisms: one acting respectively on the species mass and the other acting on the mixture momentum. By employing an inter-molecular friction force, the diffusion and convection are coupled through the species momentum. Diffusion and convection mechanisms are closely related in several physical phenomena such as in the viscous fingering instability.

A simulation of the viscous fingering instability is achieved by considering two species in different proportions in a porous medium: a less viscous mixture displacing a more viscous mixture. The core ingredients of the instability are the diffusion and the viscosity contrast between the components. Two strategies are investigated to mimic the effects of the porous medium. The gray lattice Boltzmann and Brinkman force models, although based on fundamentally different approaches, give in our case equivalent results. For early times, comparisons with linear stability analyses agree well with the growth rate calculated from the simulations. For intermediate times, the evolution of the mixing length can be divided into two stages dominated first by diffusion then by convection, as found in the literature. The whole physics of the viscous fingering is thus accurately simulated. Nevertheless, multi-component diffusion effects are usually not taken into account in the case of viscous fingering with three and more species. These effects are non-negligible as we showcase an initial stable configuration that becomes unstable. The reverse diffusion induces fingering whose impact depends on the diffusion between species.

Keywords: lattice Boltzmann method, fluid mechanics, multi-component flows, mixture dynamics, viscous fingering instability